

NORTHWESTERN UNIVERSITY

Investigation of Polymer Conjugated Helix Bundle Peptides to Design
Micellar Nanocarriers with Tunable Size and Stability using Molecular
Dynamics

A DISSERTATION

SUBMITTED TO THE GRADUATE SCHOOL

IN PARTIAL FULFILLMENT OF THE REQUIREMENTS

for the degree

DOCTOR OF PHILOSOPHY

Field of Mechanical Engineering

By

Dan Ma

EVANSTON, ILLINOIS

June 2018

ABSTRACT

Investigation of Polymer Conjugated Helix Bundle Peptides to Design Micellar Nanocarriers with Tunable Size and Stability using Molecular Dynamics

Dan Ma

Hybrid polymer-peptide conjugates are receiving increasing attention as a promising class of biomaterials. Polymer conjugated coiled-coil peptides are a new addition to these designer macromolecules. Even though a variety of experiments and computational simulations have shown stabilization of helices upon polymer conjugation, there are still many questions regarding the conformations of the attached polymer chains and their effects on the thermomechanical and aggregation behavior of peptides. Here, we first investigate the self-assembly of coiled-coils with single polymer chains covalently conjugated to either the end or side, and compare with no polymer conjugation. Our results ascertain polymer stabilization effects on both structural and thermodynamical properties of the peptides. Next, based on scaling theory for tethered polymers, we study multiple polymer chain conjugation to investigate the effect of conjugation density on the stability of coiled-coils and to explore the mushroom conformation of polymer chains on the helix surface. Our findings reveal the molecular mechanisms underpinning recent experimental observations on the stability of protein-PEG conjugates and lay the groundwork for development of stable protein bundles that can serve as drug delivery vehicles, nanocarriers and other biomechanical building blocks.

Building on these findings, we focus on a recent design that has utilized end-conjugation of alkyl chains to 3-helix coiled-coils to achieve amphiphilicity, combined with the side-chain conjugation of polyethylene glycol (PEG) to tune micelle size through entropic confinement forces. Next, we investigate this phenomenon in depth, using micelle theory and coarse-grained dissipative particle dynamics (DPD) simulations in an explicit solvent. We analyze the conformations of the PEG chains conjugated to three different positions on 3-helix bundle peptides to observe the degree of confinement upon assembly, as well as the ordering of the subunits making up the micelle. We discover that the micelle size and stability is dictated by competition between the entropy of the PEG chain conformations in the assembled state and intermolecular cross-interactions among PEG chains that promote cohesion between neighboring conjugates. Our analyses build on the role of PEG molecular weight and conjugation site in micelle shape and lead to computational phase diagrams that can be used to design 3-helix micelles. This work opens pathways for the design of multifunctional micelles with tunable size, shape and stability.

Homomeric micelles with tunable size, shape and stability have been extensively studied for biomedical applications such as drug carriers. However, designing the local valency and self-assembled morphology of nanophase-separated multicomponent micelles with varied ligand binding sites remains challenging. Finally, we present micelles self-assembled from amphiphilic peptide-PEG-lipid hybrid conjugates, where the peptides can be either 3-helix or 4-helix coiled-coils. We demonstrate that the micelle size and sphericity can be controlled based on the coiled-coil oligomeric state. Using theory and coarse-grained dissipative particle dynamics (DPD) simulations in an explicit solvent simulation, we studied the distribution of 3-helix and 4-helix

conjugates within the mixed micelles and observed self-organization into nanodomains within the mixed micelle. We discover that the phase separation behavior is dictated by the geometry mismatch in alkyl chain length from different coiled-coil oligomeric states. Our analyses on the self-assembly tendency and drug delivery potency of mixed micelles with controlled multivalency provide further important insights into the assembly and formation of nanophase-separated micelles.

Acknowledgements

I am indebted to many people for helping me during my PhD studies and development of this thesis.

I have the greatest gratitude for my advisor, Prof. Sinan Keten, whose patience, wisdom, and knowledge have always helped me throughout my research studies. From our discussions, I have always learned how to identify valuable implications from the simulation results and find the best direction to pursue.

I would like to thank my committee members Prof. Catherine Brinson, Prof. Randall Snurr for their guidance and support.

I would like to thank Dr. Elham Hamed, whose enthusiasm encouraged my passion for research. More importantly, I have benefited greatly from her guidance and support. I would also like to thank the friendly and thoughtful people (especially Elizabeth) in Keten group for their helpful discussions, collaborations and providing me with a wonderful environment in my studies.

I would like to thank Prof. Ting and Dr. JooChuan Ang from UC Berkeley, Prof. Reidar Lund from University of Oslo for insightful discussions and collaborations on experiments.

And last but not least, my warmest feelings and deepest thanks go to my parents who have always wholeheartedly supported me during my graduate studies.

I would like to acknowledge support from the Department of Mechanical Engineering for the 2016-2017 Martin Outstanding Doctoral Fellowship and from Northwestern TGS for the 2017-2018 Honorary Terminal Year Fellow.

I would like to acknowledge support from the Office of Naval Research (Grant # N00014-13-1-0760).

I would like to acknowledge the support of the computational resources and staff contributions provided for the Quest high performance computing facility at Northwestern University which is jointly supported by the Office of the Provost, the Office for Research, and Northwestern University Information Technology. I would also like to acknowledge the support of Ares high performance computing facility at Northwestern University and dynano cluster.

Table of Contents

ABSTRACT.....	2
Acknowledgements	5
List of Tables, illustrations, Figures, Graphs.....	10
Chapter 1 Introduction and Background.....	21
1.1 Introduction to Polymer Conjugation.....	21
1.1.1 What Are Proteins?	21
1.1.2 What Are Coiled-Coils?	22
1.1.3 Why Polymer Conjugation?.....	23
1.1.4 Application	24
1.2 Introduction to Amphiphilic Micelle as a Nanocarrier.....	25
1.3 Thesis Outline	26
Chapter 2 Atomistic and Molecular Modeling Methods	28
2.1 Why Molecular Dynamics?	28
2.2 Introduction to MD	28
2.2.1 Basic Principles of Molecular Dynamics.....	28
2.2.2 Force Fields	30
2.2.3 Enhanced Sampling Techniques: Metadynamics.....	32
2.2.4 Periodic Boundary Conditions and Ensembles	34
2.3 Coarse-grained Modeling	35
2.3.1 GO-like Models	36

2.3.2 MARTINI Models	38
2.3.3 Dissipative Particle Dynamics Model	40
2.4 Phase Separation Theoretical Studies	42
Chapter 3 Conjugation Effects on Self-assembling Helix Bundles	43
3.1 Generating Coiled-coil-polymer Conjugates	45
3.2 Melting Behavior Investigation with Coarse-grained Model.....	47
3.3 Self-assembly Pattern Dependence on Conjugation.....	50
3.4 Thermodynamic Properties of Unzipping.....	56
Chapter 4 Multi-PEG conjugation effects.....	59
4.1 Building Multi-PEG-helix Conjugates	61
4.2 Helicity Investigation upon Multiple Chains Conjugation	62
4.3 Multi-PEG Chains Conformational Probabilities Study.....	64
4.4 Prediction with Brush Theory	70
Chapter 5 Design of 3-helix Micelles with Tunable Shapes	74
5.1 Modeling Approach and Force Field Terms	76
5.2 Simulation Details for Self-Assembly Studies	79
5.3 CG Model Validation with Experiments	81
5.4 PEG Chains Conformational Analyses.....	84
5.5 Micelle Shapes with PEG Conjugation Sites and Molecular Weight	91
Chapter 6 Micelles based on a mixture of coiled-coils.....	96
6.1 Model Generation with Different Coiled-coils Oligomeric States....	98

6.1 Micelle Self-assembly Process	100
6.2 Alkyl Chain Conformations Studies	102
6.3 Phase Separation in Mixed Micelles	105
6.4 Micelle Shape and Stability Investigations	108
Chapter 7 Conclusions	113
References	118

List of Tables, illustrations, Figures, Graphs

Figure 1.1 (a) Amino acid structure, (b) Schematic figures of hierarchical protein structures.	21
Figure 1.2 Schematic figure of a coiled coil consisting of a number of helices; each color represents one helical strand.	23
Figure 2.1 Schematic representation of the idea of metadynamics.	33
Figure 2.2 Schematic representation of the idea of periodic boundary conditions.....	35
Figure 2.3 Schematic figure of non-bonded potentials: comparison of standard Lennard-Jones potential and potential in GO-like models.	37
Figure 2.4 Schematic figure of one helix strand and polymer conjugates structure: comparison of all-atom model and MARTINI coarse-grained model. Smaller bonded opaque beads represent the all-atom model, while large transparent beads represent the coarse-grained model.	39
Table 2.1 Interaction parameter between beads i and j , a_{ij} . The magnitude of a_{ij} denotes the maximum repulsion that the particles will experience. H, P, A, W represent helix, PEG, alkyl chains and water beads, respectively. Parameters are adopted from Groot [2], and calibrated to match experimental studies [3, 4].....	41
Figure 3.1 Schematic figure of CG model utilized. (a) Schematic of the coarse-grained model of the trimeric coiled coil where each residue is mapped into a single bead located at the position of $C\alpha$ atom of the atomistic structure; and (b, c) schematics of the coiled coil with side and end polymer conjugation.....	45

- Figure 3.2 The relationship between the predicted apparent melting temperature (T_m) and simulation heating rate (r) for a single trimeric coiled coil with no polymer attached, with a side-conjugated polymer, and with an end-conjugated polymer..... 49
- Figure 3.3 Example snapshots of self-assembly simulations showing (a, b) the more dominant side-by-side aggregation pattern and (c, d) the less occurring end-to-end aggregation pattern, for coiled coils with side-conjugated polymer and end-conjugated polymer chains..... 51
- Figure 3.4 Results of self-assembly simulations of coiled coils without polymer as well as with side and end polymer conjugation showing (a) the number of assembled clusters and (b) aggregation number as a function of concentration, where different concentrations correspond to different number of trimers in a simulation box of fixed dimensions..... 54
- Figure 3.5 Results of self-assembly simulations of coiled coils without polymer as well as with side and end polymer conjugation showing (a) the number of assembled clusters and (b) aggregation number as a function of concentration, where different concentrations correspond to a fixed number of trimers in simulation boxes of different volume..... 55
- Figure 3.6 Results of MetaD simulations showing the energy required for unzipping of one helical unit (shown in blue) from the three-helix bundle without polymer, with side-conjugated polymers, and with end-conjugated polymers. The collective variable d is defined as the distance between the center of mass of one helical unit and the center of mass of the two others. 56

- Figure 4.1 Schematic figures of polymer brush and mushroom region. For a grafting distance S much larger than polymer size R , the chains form a mushroom, while with S grafting distance much smaller than the polymer size H , the chains adopt a brush conformation. 60
- Figure 4.2 Schematic figure of the coiled coil-PEG conjugate structure, where three PEG chains are attached to residue 7 (blue chains), 14 (red chains), and 21 (green chains) of each helical strand. The trimeric coiled coil is consisting of three α -helices with a sequence of Ac-EVEALESKVAALESKVQALESKVEALEHG-CONH₂. For (a) all-atom model figure; (b) MARTINI coarse-grained model figure. 61
- Figure 4.3 Fractional helicity of the peptide as a function of PEG molecular weight (M_n ; black solid circle markers), based on predictions of all-atom molecular dynamics simulations. The secondary axis (red solid square markers) illustrates the root mean square deviation (rmsd) of the peptide structure with respect to the crystalline structure of the coiled coil for different PEG molecular weights. Both the helical content and coiled coil configuration of the peptide are retained upon the conjugation of multiple PEG chains. 64
- Figure 4.4 The average radius of gyration (R_g) of all conjugated PEG chains for the case where three chains are attached to each helix of coiled coil and its comparison with the case of single side-conjugated PEG chain, both all-atom and coarse-grained simulation are included. 64
- Figure 4.5 Conformational density distribution of the three PEG chains attached to each helical strand of the coiled coil for chains with (a) 10, (b) 20, (c) 30, and (d) 40

monomers. The x and y axes denote the cross-section of the coiled coil (see Figure 4.2). The boundaries of the helices are shown in solid white lines while the boundaries of PEG influence regions are depicted by dashed and dotted white lines. The red and blue colors denote, respectively, the highest and lowest values of density over the time of simulation and the color bar ranges are different for different panels. 67

Figure 4.6 Conformational density distribution of all PEG chains attached to the coiled coil for chains with (a) 10, (b) 20, (c) 30, and (d) 40 monomers. The r axis denotes the radial distance from the z axis, which lies along the coiled coil length (see Figure 4.2). The boundaries of the coiled coil are shown in solid white lines while the boundaries of PEG influence regions are depicted by dashed and dotted white lines. The red and blue colors denote, respectively, the highest and lowest values of density over the time of simulation and the color bar ranges are different for different panels. 68

Figure 4.7 Probability density distribution profile of all PEG chains attached to the coiled coil for chains with 10, 20, 30, 40, 60, 80 and 120 monomers. The x axis denotes the radial distance of each monomer from the z center of mass of the helix bundle scaled by the radius of gyration, and the y axis denotes the distribution probability at certain distance normalized with the volume. 69

Figure 4.8 PEG chain radius of gyration trend with increasing chain length. All results are from CG model simulations; red squares indicate calculated data points, while solid blue line shows the fitting line for all simulation data, and the black dash point line depicts the predicted values of R_g if the chains were in the brush regime. 72

Figure 5.1 (a) Schematic figure of a 3-helix bundle with the PEG chain and the alkyl chain

conjugated on one strand, the cylindrical coordinate here originates in the center of the whole triple helix bundle, with z axis along the average center of the 3-helix bundle and r axis vertical to the length of triple helix bundle and (b) a sample micelle (aggregation number is 15) from simulation results, with PEG conjugated on position 14, R here indicates the distance to the micelle center of mass. The helical strands (cyan) together with their conjugated PEG chains (pink) form the shell of this spherical structure, while the alkyl chains (yellow) and their connection points (purple) to the helical strands form the core of the sphere. Figure (a) shows the coarse graining method of one single helix strand together with polymer chains conjugated on it..... 78

Figure 5.2 Size of the micelle (aggregation number) as a function of different PEG chains conjugated sites. Figure (a) shows the average micelle size in system for different cases, while (b) shows the largest micelle size for different cases. For all the three different conjugation sites (7, 14, 28), average values and standard deviations are indicated, while dual mixture case includes a mean value of the mixture P7&P14, mixture P7&P28 and mixture P14&P28. 80

Figure 5.3 Distribution of PEG chains as a function of distance to the center of a micelle, and comparison with experiment. Three conjugation sites are included: (a) PEG chains conjugated on P7; (b) PEG chains conjugated on P14; (c) PEG chains conjugated on P28. A comparison between experimental (dashed lines) and CGMD (solid lines) is shown above. For the CGMD results, all the data are collected from the sample micelles. For both experimental and simulation data, the micelle core (red lines) comprises the alkyl chains, and the micelle shell (black lines) comprises the peptides

with conjugated PEG chains.	83
Figure 5.4 Distribution weight fraction of all micelle component beads and water beads as a function of distance to the micelle center of mass, including cases for all the three different PEG conjugation sites. (a) PEG chains conjugated on P7 of the isolated triple helix bundle; (b) PEG chains conjugated at P7 in the sample micelle; (c) PEG chains conjugated at P14 in the sample micelle; (d) PEG chains conjugated at P28 in the sample micelle. Green lines indicate the peptide distribution, black lines indicate the alkyl chain distribution, red lines indicate the PEG chain distribution and blue lines indicate the water distribution. The dash dot magenta lines indicate the estimated position of each conjugation site.....	85
Figure 5.5 PEG chain distribution plots for four different cases, including (a) PEG chains conjugated on the isolated triple helix bundle; (b) PEG chains conjugated at P7 in the sample micelle; (c) PEG chains conjugated at P14 in the sample micelle; (d) PEG chains conjugated at P28 in the sample micelle. The color bar shows the distribution probability decrease from red to blue, the white dashed line in each plot indicates the distribution area with a probability larger than 2×10^{-3}	87
Table 5.1 Average conformational size of PEG polymer chains, including radius of gyration R_g , R_g in the radial direction (along the helix bundle), R_g on the tangential direction (vertical to the helix bundle) and end-to-end distance R_{ee} in DPD simulations. The results are given by the present simulations for all conjugation sites, on the isolated triple helix bundle and free polymer chains in water with the standard deviation included. All the data presented here studied the same PEG chain molecular weight	

2000 Da.....	89
Figure 5.6 Three schematic figures in (a) on the left indicate different PEG conjugation sites with their possible distributions. Vector R here indicates the distance to the micelle center of mass, and a phase diagram (b) of the PEG conjugation sites and the PEG degree of polymerization, illustrating the predicted micelle shape, based on geometric parameters calculated from simulation. The color bar shows the packing parameter decrease from yellow to blue. Two contour lines distinguish three different micelle shapes according to theory. The points represent the visualized shape from simulations, with blue crosses indicating a bilayer shape, red squares indicating a cylinder shape and black circles indicating a spherical shape. The formed micelle shape changes from bilayer to cylinder to sphere with an increasing PEG molecular weight.....	
	91
Table 5.2 Geometric quantities that determine micelle packing parameter for different degrees of polymerization (DP) and PEG conjugation positions, including V_0 , the occupied volume per subunit and a_0 , the outer surface area per subunit. The packing parameters (PP) are given by the results of $PP = V_0 a_0 \cdot lc$, from which $lc = 6.00nm$	
	95
Figure 6.1 Schematic figures of MD models used in simulations: (a) 3-helix bundle (cyan) in CG DPD model with the PEG chain (pink) and the alkyl chain (purple and green) conjugated to each strand. (b) 3-helix bundle in AA model. For simplicity, only the PEG (CPK drawing method) and alkyl (Licorice drawing method) chains conjugated to the blue helix bundle are shown here. (c) 4-helix bundle (cyan) in the CG DPD model with the PEG chain (pink) and the alkyl chain (purple and green) conjugated to each	

strand. (d) 4-helix bundle in AA model. For simplicity, only the PEG (CPK drawing method) and alkyl (Licorice drawing method) chains conjugated to the blue helix bundle are shown here. 98

Figure 6.2 The number of free subunits in system and the largest, average aggregation number defined as the number of helices in the (a) 3HM, (b) 3&4 mixture micelle, and (c) 4HM as a function of time. The sharp increases indicating micelle fusion process are highlighted in dashed blue ovals. The results are obtained from DPD CG simulations with 100 subunits for each case. 101

Figure 6.3 The largest aggregation number defined as the number of helices in the largest micelle in systems (a) 3HM, (b) 3&4 mixture micelle, and (c) 4HM as a function of time. The results are obtained from DPD CG simulations, including 3 different trials for each case and with 100 subunits for each system. 102

Table 6.1 Average conformational size of alkyl chains, including radius of gyration R_g and end-to-end distance R_{ee} in DPD simulations. The results in the table are given by the present DPD CG simulations for alkyl chains in 3HM, 4HM and 3&4 mixture micelles, alkyl chains on the isolated 3-helix or 4-helix micelles, and compares the CG DPD and AA simulation results for alkyl chains on isolated 3-helix and 4-helix micelles. 103

Figure 6.4 Distribution behavior of alkyl chains on the helix bundle cross sectional plane in micelles, including alkyl chains conjugated on (b) a 3-helix peptide and (c) a 4-helix peptide. A schematic figure (a) on the left shows the axis setting method in both figures: with the alkyl bead distribution projected onto the xy plane that is orthogonal to the helix bundle (radial) direction. In the figure (b)(c), the color bars in show the

probability distribution decrease from red to blue, the black dashed line indicates the estimated conjugation location on the helix terminus, and the orange point dash lines indicate the alkyl chain distribution area that has a probability density value larger than 1×10^{-4} . The results are given by the present DPD CG simulations for 3HM and 4HM sample micelles with the same number of subunits over the last 150 ns after convergence. 104

Figure 6.5 Phase separation and fragmentation measurements (red) compared to well mixed theoretical micelles (black) for three sample micelles (a-c). Panels (a-c) show θ , the number fraction of 8-bead fragmentation as a function of the number of 3-helix component in the 8 beads. The aggregation number of the sample micelles are 50, 56 and 57, with 3helix:4helix ratio 6:8, 8:8 and 7:8 respectively. The calculated sum of squared error (SSR) are high as 0.504, 0.438 and 0.492, which are anticipated for phase separated mixed micelles. 105

Table 6.2 Average conformational size of PEG polymer chains, including radius of gyration R_g , R_g in the radial direction (along the helix bundle), R_g in the tangential direction (vertical to the helix bundle), R_g in total and end-to-end distance R_{ee} in CG DPD simulations. The results are given by the present DPD CG simulations for PEG in 3HM, 4HM and 3&4 mixture micelles, and PEG on the isolated triple helix bundle and free polymer chains in water with standard deviations included. All the data presented here studied the same PEG chains with molecular weight 2000 Da in DPD simulations. 106

Figure 6.6 Schematic figure of the micelle fusion process, with the initial configuration of

the small micelles at 860 ns, and the merged micelle at 3000 ns and 3700 ns. This figure shows the migration of coiled-coils into nanodomains within the mixed micelle. Only alkyl chains are shown in this figure for simplicity, with 4-helix components in red and 3-helix components in blue.	107
Table 6.3 Aggregation number, alkyl core radius, vacant volume in micelle core, water beads permeability and micelle SASA in comparison of 3HM, 4HM and 3&4 mixture micelles. The results are given by sample micelles in the present DPD CG simulations including all the three helix components. The water content in micelle is defined as the number of water beads inside the sample micelle (the micelle boundary here is defined as a PEG weight fraction at 10%).	108
Figure 6.7 Average interaction energy between alkyl beads and (a) alkyl beads, (b) other beads, including the peptide, PEG and water, (c) all beads as a function of simulation time. This energy function compares pure 3-helix micelle (black), pure 4-helix micelle (red) and 3&4 mixture micelles (blue). The blue triangles indicate the convergence time for the two systems, at 300 ns for 3HM, 1000 ns for 4HM, and 330 ns for 3&4 mixture micelles. The results are given by DPD CG simulations including 3HM, 4HM and mixture micelles.	110
Table 6.4 Average interaction energy of alkyl beads to alkyl beads, between other repulsive beads, and among all beads. These average interaction energies are computed for sample 3HM, 4HM and mixture micelles; and for alkyl bead interaction energy in 3-helix and 4-helix conjugates isolated in water solution. The free energy of 3HM, 4HM, and mixture micelle formation is also calculated as the energy in the micelle	

minus the energy in an isolated single helix bundle. The 3HM and 4HM results are given by the average and standard deviation values of 3 micelle samples with different sizes, and mixture micelles results include 3 different sample micelles with an increasing 3-helix component:4-helix component ratio. Given that DPD naturally has a repulsive interaction potential, larger interaction energy values here indicate less favorable interaction.111

Chapter 1 Introduction and Background

1.1 Introduction to Polymer Conjugation

1.1.1 What Are Proteins?

Proteins constitute critical building blocks of life. They are large molecules or macromolecules, consisting of amino acid residues, and can fold into specific three-dimensional structures. The covalent peptide bonding sequence of amino acids is the primary structure of a protein (see Figure 1.1 b), which determines the three-dimensional configurations and specific functionalities. Amino acids are important organic compounds composed of amine ($-\text{NH}_2$) and carboxylic acid ($-\text{COOH}$) groups, together with a specific side chain group ($-\text{R}$) (see Figure 1.1 a), which can be

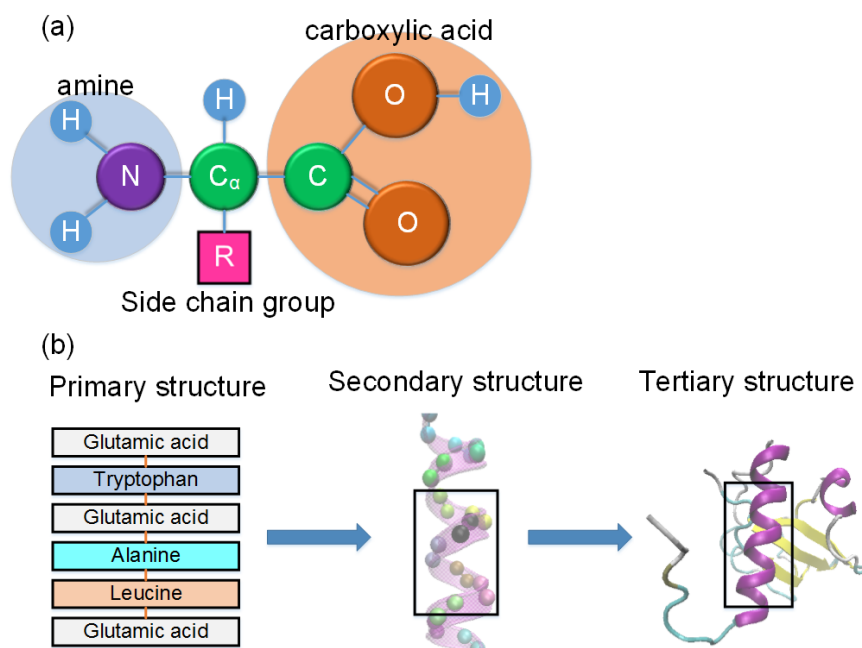


Figure 1.1 (a) Amino acid structure, (b) Schematic figures of hierarchical protein structures.

charged, polar, or hydrophobic, connected to the center carbon atom. Twenty different amino acids exist in nature, which serve as the major building blocks of proteins. Peptides are short chains of amino acids linked by amide bonds; they are distinguished from proteins mainly based on their smaller size.

Moreover, some specific amino acids sequences can result in the formation of a specific secondary structure (see Figure 1.1 b), among them α -helix and β -sheet are the most common structures. These structures are formed by hydrogen bonds between some of the backbone atoms. β -sheets are composed of β -strands packed in a parallel or anti-parallel configuration. Natural α -helices usually have a right-handed spiral conformation; each helix turn has 3.6 residues and each residue has a rise of 1.5 Å. This structure makes α -helices universal and versatile protein motifs.

1.1.2 What Are Coiled-Coils?

The coiled-coil is one kind of protein tertiary structure, which has one or more protein secondary structures in their protein domains. Tertiary structure refers to the three-dimensional geometry of the protein (see Figure 1.1 b), which is determined by interactions and bonds of side chains within a particular protein. Coiled-coils consist of two or more α -helix strands packed either in the same (parallel) or opposite (anti-parallel) direction. The helices wind into superhelical structures with either right-handed or left-handed configurations [5], as shown in Figure 1.2. In biological systems, coiled-coils assemble into a wide variety of structures, including hair, filaments, cells, and etc. [6, 7]. They have a common repeating sequential pattern involving seven amino acids, which is known as a heptad [6]. The heptad repeat can be represented as *abcdefg*, where the first and fourth residues, *a* and *d*, are hydrophobic amino acids,

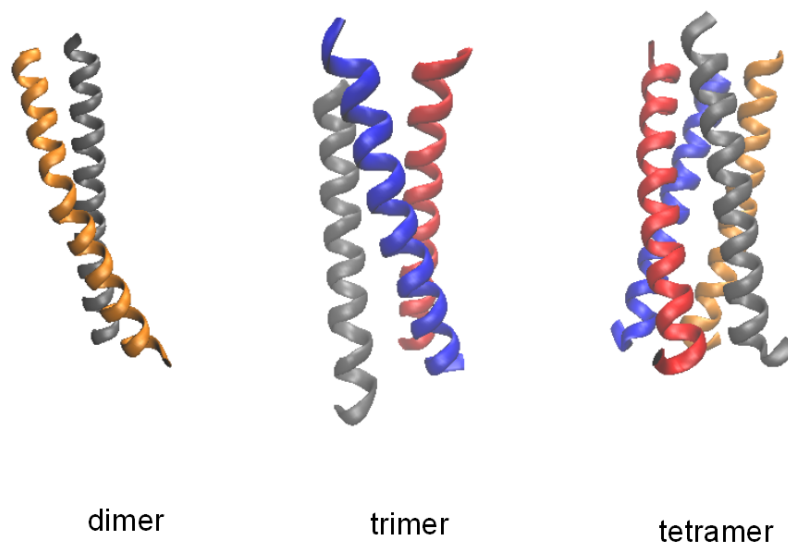


Figure 1.2 Schematic figure of a coiled coil consisting of a number of helices; each color represents one helical strand.

oppositely charged residues are located at positions *e* and *g*, while residues *b*, *c* and *f* are exposed to the solvent [8]. Such a sequence distribution makes coiled-coil amphipathic, with residues *a* and *d* forming an internal hydrophobic core and residues *e* and *g* forming interhelical ionic interactions.

1.1.3 Why Polymer Conjugation?

The α -helix is among the most common and stable protein secondary structures in nature. However, a significant challenge of its development in the biomedical fields lies in its high structural dependence on environmental factors, such as temperature, PH, ionic strength or pressure [9], especially for short chains [10]. While protein properties, as well as functionalities, are controlled by their structural stability, many studies have observed an improvement in helix

stability by cross covalently linking side-chain residues or introducing conformational constraints to reduce the entropy for helix unfolded states [10, 11]. Helix capping [12, 13], increasing the hydrophobicity of the peptide hydrophobic core [14-16], using hydrocarbon staples [17-19], introducing specific interstrand interactions [11, 20-22] , and conjugation with poly(ethylene glycol) (PEG) [8, 11, 23-27] are examples of effective strategies that have been used to enhance helix stability. Experiments have shown no destabilization effect on the helix conformation upon PEG conjugation and reported an increase in thermal stability of the peptide [26, 28]. Molecular dynamics simulations have also ascertained that PEG chains can preserve helical secondary structure [8] by forming a shell around the helix and reducing both peptide solvent accessible area and interfacial energy for hydrophobic domain exposed to the polar solvent [25].

1.1.4 Application

Coiled-coils, especially with a recently *de novo* new design [29, 30] have a variety of applications. *De novo* peptide designs are developed with simplified protein folds with which a structure-function relationship can be more readily ascertained [31]. The coiled-coils conjugated with PEG chains have also become a common choice for building amphiphilic blocks [27], which can form micelle structures and thus serve as drug delivery vehicles [28] or nanocarrier platform [26, 27] in medical applications. However, the detailed mechanical and thermal properties of peptide-PEG hybrid conjugates is still not fully revealed and the effect of multiple chain conjugation on their stability and aggregation is uncovered.

1.2 Introduction to Amphiphilic Micelle as a Nanocarrier

Amphiphilic molecules can spontaneously self-assemble into micelles and have been routinely used to synthesize nanocarriers. A new design of peptide-polymer conjugates with PEG chains covalently joined to each coiled-coil helix strand was reported by Shu et al. [32] Polyethylene glycol (PEG), which has good hydrophilic properties and biocompatibility, has become a popular building block with which to synthesize hybrid amphiphilic molecules. When the PEG-helix conjugates are further conjugated with hydrophobic alkyl chains as reported in Ref. [3, 27, 33], the amphiphilic molecules can form spherical micelles ~15 nm in size.

10–30 nm nanocarriers are highly desirable as drug delivery and imaging probe vehicles due to their ability to penetrate deep tissue or other biological barriers [34-37]. The unique sub-20 nm size regime of 3-helix micelles (3HM) assures deep tumor penetration via an enhanced permeation and retention (EPR) effect [38-42] and the individual alkyl, peptide, and PEG components allow for tunable micelle kinetic stability. [43, 44] 3HM in mice displayed a long blood circulation half-life of 29 hours, selective accumulation in tumors, and minimal accumulation in the liver and spleen. [45] Systemic delivery of doxorubicin-loaded 3HM to tumor-bearing mice showed selective tumor accumulation over other organs. [27] Experimental results suggest that 3HM is more effective than liposomes in accumulating and distributing within tumor tissue as well as penetrating the blood brain barrier (BBB). [46]

In summary, stable, long circulating 3-helix micelles (3HM) based on amphiphilic peptide-polymer conjugates are attractive candidates as drug carriers. However, the molecular origins of their behavior and performance are yet to be determined. There is a great need to understand the micelle performance from a structural standpoint to develop tunable, stable, and

small nanocarriers. Previous experimental studies have reported the effect of alkyl chain length and PEG conjugation location along the helix backbone on the stability of 3HM. [43, 44] The PEG chains were shown to stabilize the 3-helix micelle by means of entropic repulsion and micelles formed with different alkyl chain length showed different size and stability. However, the distribution of water molecules and degree of hydration within micelles is unknown. As structural deconvolution of the micelle into its individual components is essential, we thus utilized molecular dynamics simulation tools to better understand the role of PEG and coiled-coil oligomeric states in the structural stability of 3HM.

1.3 Thesis Outline

In order to understand the self-assembly behavior of peptide-PEG conjugates to further design micellar nanocarriers with tunable sizes and shapes, we performed a variety of computational studies using molecular dynamics. Chapter 2 will have a detailed introduction to all the technical methodologies we used in our study. This includes basic computational methods: molecular dynamics, three kinds of coarse-grained models we used, and other technologies. Next are four specific study results on polymer conjugation. First, with a single polymer chain conjugated to different locations of a coiled-coil, and with different conjugate concentrations in the system, we explored the melting behavior, unzipping energy, as well as aggregation behavior of helix-polymer conjugates. All the details including materials, simulation methods, and results will be explained in Chapter 3. Then, coiled-coil trimers with multiple PEG chains conjugated onto the surface will be investigated in Chapter 4. With three PEG chains attached to each helix strand, we explored the effect of conjugation density on the conformations of attached PEG chains, with radius of gyration, density profile, and conformational distribution figures included.

Based on the verified coiled-coil stable structure after PEGylation, we developed a CG DPD model with explicit water solvent. We look into PEG conformational distributions on different conjugation sites and with different molecular weights to design peptides-PEG-lipid hybrid conjugates based micelles with tunable sizes and shapes in Chapter 5. We further utilized the CG DPD model to study the micelle size and shape with different coiled-coil oligomeric states and will provide important insights into the formation of nanophase-separated micelles in Chapter 6. At last, in chapter 7, we summarize all the related studies, provide the key conclusions of my work and indicate possible research directions to go for in the future.

Chapter 2 Atomistic and Molecular Modeling Methods

2.1 Why Molecular Dynamics?

There are three approaches to scientific research: analytical, experimental, and computational methods. The most promising feature of computational modeling is that it can provide insights into problems that cannot be tackled analytically or experimentally. Molecular dynamics is a powerful computational tool that enables us to explore the physical and thermomechanical behavior of systems at small time and length scales that are challenging to reach using experiments. Additionally, some loading scenarios and environmental conditions, such as very high/low temperatures or pressures, can be readily applied in MD simulations while they might be expensive or even unattainable in experiments. Also, computational models allow us to build and simulate systems with high levels of structural and chemical complexity that are difficult to design and fabricate experimentally. These remarkable potentials of molecular dynamics motivate us to choose this technique to study the behavior of helix bundles conjugated with polymer chains and multicomponent micelle structures.

2.2 Introduction to MD

2.2.1 Basic Principles of Molecular Dynamics

Molecular dynamics (often referred to as MD) is a computational method that can solve simultaneous equations of motion for a system of particles at nanoscale, where the particles may represent atoms and molecules [47]. In this technique, we assume that each atom or molecule acts like a particle with a certain mass, and different particles interact with each other through

certain kinds of potentials. The basic idea of molecular dynamics is based on Newton's Laws, where the motion of every particle should at first follow the Newton's Law of Motion:

$$\vec{F} = \frac{d}{dt}(m\vec{v}) = m\vec{a} \quad (2.1)$$

Solving equations of motion then leads to particles positions $r_i(t)$, velocities $v_i(t)$, and accelerations $a_i(t)$ for each step, and dynamical trajectories of each particle in the system can be revealed, indicating overall dynamics of the system and mechanical properties as well. The total energy of the system can be written as a sum over kinetic energy (K) and potential energy

$$E = K + U \quad (2.2)$$

(U).

$$K = \frac{1}{2}m \sum_{j=1}^N v_j^2 \quad (2.3)$$

$$U = U(r_j) \quad (2.4)$$

From which, the kinetic energy and potential energy are:

The potential energy is a function of the atomic coordinates $r_j(t)$ (where $j=1, 2 \dots N$ refers to a collection over all particles in system) with a properly defined potential energy surface $U(r_j)$,

$$F = m \frac{d^2 r_j}{dt^2} = -\nabla_{r_j} U(r_j), j = 1, 2 \dots N \quad (2.5)$$

the force field terms are obtained as

The numerical problem can only be solved for a system with more than two particles, $N > 2$. Typically, MD is based on updating schemes that yield new positions from particles previous positions, velocities and current accelerations. For example, in the basic Verlet algorithm, this can be formulated as:

$$r_i(t_0 + \Delta t) = -r_i(t_0 - \Delta t) + 2r_i(t_0) + a_i(t_0)(\Delta t)^2 + O(\Delta t^4) \quad (2.6)$$

Various numerical integration methods, including the common Velocity Verlet method are employed to solve the equation of motion, where the material volume is represented by dynamics of a large ensemble of particles. This technique can be used for not only atomistic systems but also mesoscale coarse-grained systems. However, in particular for all-atom simulations, due to high frequency vibration of light atoms, the system requires a time step on the order of femtoseconds ($1 \text{ fs} = 10^{-15} \text{ s}$). Thus, due to computational limitations, MD simulations are restricted to time-scales of tens to hundreds of nanoseconds.

In this thesis, MD is used to explore a number of complex biophysical phenomena, including helix bundle self-assembly, multiple polymer conjugation onto helix bundle, as well as micelle formation under varies peptide and polymer components.

2.2.2 Force Fields

For each system, it is crucial to define a proper interaction potential between particles, and then come up with accurate configurations. There are many variations of different kinds of potentials [48] including external fields, pair-wise potential and multibody interactions. The use of pair-wise potentials is quite common; chemical bonds like ionic, covalent, and metallic bonds or physical bonds like Van der Waals interactions and hydrogen bonds can all be represented by

pair-wise potential terms. The non-bonded potentials describe attractive and repulsive forces among groups of atoms, which are typically based on empirical data and first-principles based information [49]. One model that is quite common to characterize a combination of repulsion and attraction between atoms is known as Lennard-Jones (LJ) potential, which is given as

$$U_{LJ} = 4\varepsilon\left(\frac{\sigma^{12}}{r^{12}} - \frac{\sigma^6}{r^6}\right) \quad (2.7)$$

where σ is the finite distance at which the inter-particle potential is zero, while ε is the interaction strength at the minimum energy.

In addition, a well-defined multibody interaction, such as the bond angle or torsion angle terms in CHARMM force field [50] or embedded atom potential [51], may be important to model complex molecular structures. With a combination of all the proper interaction potentials, the force field is then defined.

Among all the force fields, all-atom force fields are considered to be both reliable and computationally efficient ways of studying the dynamics of materials. As for biomolecules, OPLS [52], AMBER [53], CHARMM [50], and GROMOS/GROMACS [54] are commonly used as force fields and the last three additionally as MD programs or other packages. Also, NAMD [55] is another popular molecular dynamics program that can use CHARMM force fields among other force fields. For the sake of brevity, only details of the CHARMM force fields will be discussed here. Other force fields have similar basic concepts and formulations.

The CHARMM potential includes bonded and non-bonded terms to describe short and long ranged forces between particles, while contributions to bond stretching, bending, and rotation are individually defined in function (2.8), which makes it possible to formulate the dynamics of each

particle [50].

$$\begin{aligned}
 U(\vec{R}) = & \sum_{bonds} K_b(b - b_0)^2 + \sum_{angles} K_\theta(\theta - \theta_0)^2 + \sum_{dihedrals} K_\chi(1 \\
 & + \cos(n\chi - \delta)) \\
 & + \sum_{improper} K_{imp}(\phi - \phi_0)^2 + \sum_{nonbond} K_{UB}(S - S_0)^2 \\
 & + \sum_{nonbonded} \epsilon \left[\left(\frac{R_{\min(i,j)}}{r_{ij}} \right)^{12} - \left(\frac{R_{\min(i,j)}}{r_{ij}} \right)^6 \right] + \frac{q_i q_j}{\epsilon_1 r_{ij}}
 \end{aligned} \tag{2.8}$$

In the equation above, the constants after summation symbols are bond, Urey-Bradley, angle, dihedral angle and improper dihedral angle force constants, respectively, and the terms in parentheses are the bond length, Urey-Bradley 1,3-distance, bond angle, dihedral angle and improper torsion angle force, respectively, with the subscript zero representing the equilibrium distance or angle for each term. Moreover, the Coulomb and 6-12 Lennard-Jones terms constitute the external or non-bonded potentials. ϵ is the Lennard-Jones energy well depth and $R_{\min(i,j)}$ denotes the distance at which particles i and j have zero Lennard-Jones potential. q_i and q_j are the partial atomic charges of particles i and j , respectively, ϵ_1 denotes the effective dielectric constant, and r_{ij} is the distance between particles i and j .

2.2.3 Enhanced Sampling Techniques: Metadynamics

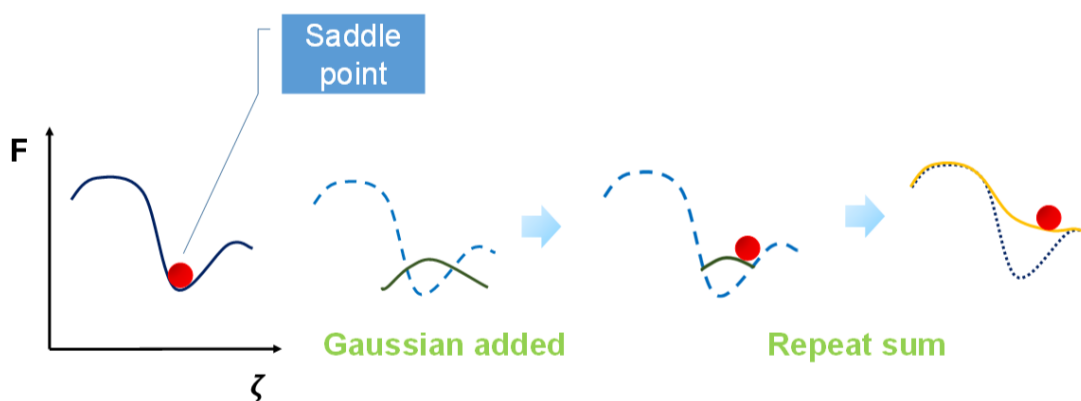


Figure 2.1 Schematic representation of the idea of metadynamics.

Due to the short time scale of MD simulations, many problems may evolve in the simulation process, such as the relevant configurations might be separated by high free-energy barriers, or systems diffuse extremely slowly in the configuration space [56, 57]. Many different methods have been developed to speed up the sampling rate of MD simulations, which are often referred to as enhanced sampling techniques. Metadynamics (MetaD) is one of the enhanced sampling techniques that facilitate sampling by reconstructing the free energy surface as a function of a few selected degrees of freedom, often referred to as collective variables (CVs) [56]. In detail, the system is biased by a history-dependent potential, which is constructed as a summation of Gaussians centered along the trajectory followed by the reaction coordinates, to improve the sampling of the phase space (see Figure 2.1).

Keeping track of the bias potential V (the position where the Gaussian potential functions were added), a reconstruction of a negative image of the history energy F is possible under the assumption that the time-history potential provides an unbiased estimate of F :

$$\lim_{t \rightarrow \infty} V(\zeta, t) \approx -F(\zeta) \quad (2.9)$$

The biased potential at time t can be written as:

$$V(S(r(t)), t) = w \sum_{i=\tau, 2\tau, \dots, t} e^{-\frac{(S(r(i)) - \zeta(i))^2}{2\delta\zeta^2}} \quad (2.10)$$

where, $S(r)$ is the function of the state of the system, $\zeta(t)$ is the value of the reaction coordinate at time t , τ is the frequency at which Gaussians are added, w is the Gaussian height and $\delta\zeta$ is the Gaussian width.

Using this method, we can provide qualitative information on the free energy of a system in a very short time. Given this advantage, we will use this method to analyze energy landscapes in Chapter 3.

2.2.4 Periodic Boundary Conditions and Ensembles

For most cases, the number of particles as well as the box size is limited in the MD simulations, which may result in different types of surface and size effects and lead to an unphysical topology of the system. For example, using a small number of water molecules in the simulation box may form a sphere and interrupt the normal simulation process due to the surface tension. Thus, periodic boundary conditions are required for certain dimensions. A simple analogy of this method is that once a particle leaves the simulation box, an image of this particle will enter the box on the opposite side [58], see Figure 2.2. Using this method, we can study material bulk properties using a small system.

Each system may also need a collection of possible microstates, which are under certain kinds

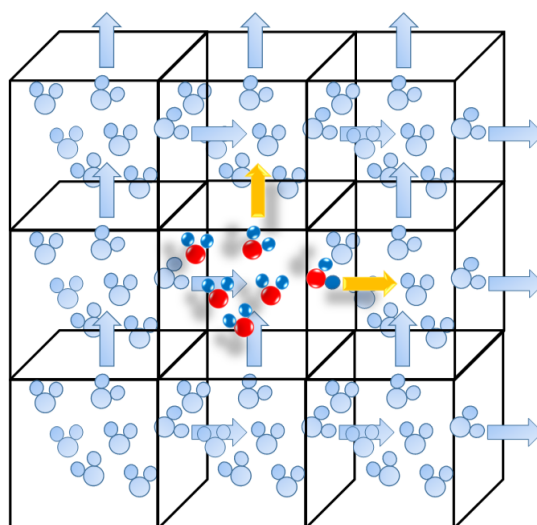


Figure 2.2 Schematic representation of the idea of periodic boundary conditions.

of thermodynamical constraints such as temperature (T), pressure (p), volume (V), total energy of the system (E) or total number of particles (N). This idealized collection of a specific system's copies, each representing a type of possible state, is called ensemble, proposed by Gibbs in 1878 [59]. In detail, different types of ensembles are obtained by keeping the values of three sets of parameters constant throughout the simulations, such as isobaric-isothermal ensemble (NPT), microcanonical ensemble (NVE), or canonical ensemble (NVT). For each specific system, we need a specific kind of ensemble according to our needs, specifically the experimental conditions that need to be reproduced.

2.3 Coarse-grained Modeling

Even though all-atom models have an accurate description of macromolecular systems, they are historically restricted when systems are large or long simulation times are needed, especially for self-assembly processes, which have a large number of molecules, including water molecules. Thus, a simplified representation of macromolecules with fewer particles, fewer degrees of

freedom, and more simplified bonded and non-bonded interactions that can be easily and correctly calculated for longer time scales is required, which is known as a coarse-grained (CG) model.

Coarse-grained models have so far been successfully applied to a wide range of molecules including proteins, nucleic acids, lipid membranes, carbohydrates etc., with several distinct approaches for developing CG models, including residue-based and shape-based modeling strategies in the context of proteins. For the sake of brevity, here, only three coarse-grained methods used in the current studies are discussed: GO-like [60, 61] models, MARTINI models [62-64] and DPD models, which are all residue based coarse-grained models.

2.3.1 GO-like Models

GO-like models [60, 61] are primarily built for peptides or proteins. In these models, each amino acid is represented by a single bead located at the C_α position, with a mass equal to the mass of the amino acid. The primary feature of the GO-like model is that the protein structure is biased toward its native configuration [61]. The beads are connected with each other through harmonic or non-linear springs representing the covalently bonded protein backbone. In detail, harmonic potentials are applied to each of bonds and angles while a dihedral term reflecting the preferences of the backbone dihedral angles of the residues is included [60]. All the bonded potentials follow the formulations in CHARMM force field [65]. For the non-bonded interactions, it has the following form [60]:

$$V_{ij} = \varepsilon_{ij} \left[13 \left(\frac{\sigma_{ij}}{r_{ij}} \right)^{12} - 18 \left(\frac{\sigma_{ij}}{r_{ij}} \right)^{10} + 4 \left(\frac{\sigma_{ij}}{r_{ij}} \right)^6 \right] \quad (2.11)$$

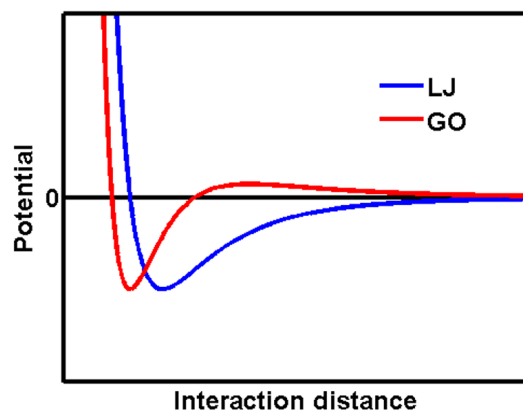


Figure 2.3 Schematic figure of non-bonded potentials: comparison of standard Lennard-Jones potential and potential in GO-like models.

where r_{ij} is the distance between residues i and j , while ε_{ij} is the interaction strength at the minimum energy. It is worth noting that this potential has two distinguishing differences from the standard Lennard-Jones potential as shown in Figure 2.3 [60]. First, it has a steeper curvature near the minimum than that of a Lennard-Jones function. Second, an additional small energy barrier, which is called the “desolvation penalty”, is included which any pair of residues must pay before forming a favorable contact. A successful GO-like model makes the residues that are in contact in the native state have a favorable attractive energy, while those not in contact in the native state have a less favorable interaction, either repulsive, neutral, or less attractive [60].

For the conjugates self-assembly studies in Chapter 3, we focus on the interactions between helix bundles and its influence on peptides conformations, thus explicit treatment of the water solvent is not essential here. GO-like models with peptides native configurations captured are employed for computational efficiency to assess whether significant changes from the native state are possible during the self-assembly process.

2.3.2 MARTINI Models

MARTINI force field [63] was originally proposed for coarse-grained representation of lipid systems, but was later extended to proteins as well. This model is residue based and uses a four-to-one mapping, where an average of four heavy atoms are represented by a single interaction bead [62-64]. Usually the center of mass of these four atoms defines the interaction site, and most beads have a mass of 72 amu (corresponding to four water molecules) [62]. Each protein amino acid in this model is represented by one bead for the backbone together with one or more beads for the side chain, depending on its dimensional degrees of freedom [64]. To simplify this model, basically four types of interactions are introduced: polar (P), nonpolar (N), apolar (A), and charged (C). Within these main types, subtypes are defined to precisely capture the interactions: they are either modified by hydrogen-bonding capacities (*d* refers to donor, *a* refers to acceptor, *da* refers to both, and *0* refers to none); or by a number, from 1 to 5, indicating its degree of polarity (*1* refers to the lowest and *5* refers to the highest polarity) [63].

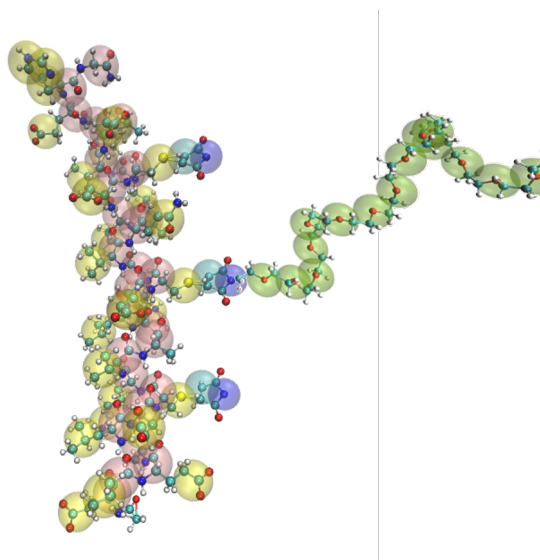


Figure 2.4 Schematic figure of one helix strand and polymer conjugates structure: comparison of all-atom model and MARTINI coarse-grained model. Smaller bonded opaque beads represent the all-atom model, while large transparent beads represent the coarse-grained model.

In the MARTINI model, the interaction potentials have similar functional forms as the CHARMM force field and only differ in some detailed constant definitions. For bonded interactions, harmonic potentials are applied to each of bonds and angles and dihedral and improper terms are used for more complicated geometries. As for non-bonded interactions, a shifted 12-6 Lennard-Jones (LJ) potential energy function together with a Coulombic potential function for charged particles are used.

There is a specific well-known issue associated with the MARTINI CG model: since water is modeled as P_4 particles, it has a relatively high freezing temperature [66]. Specifically, it may freeze from 280 to 300K, depending on the simulation conditions. This rapid and irreversible freezing process could present a real problem, especially for systems where a nucleation site already exists. The use of periodic boundaries enhances the freezing process. To prevent this

unwanted freezing of water in the model, a special antifreeze particle denoted by BP₄, with a mole fraction $n_{AF} = 0.1$, is introduced. For each BP₄-P₄ interaction, the LJ interaction strength ϵ is raised to level "O", while the length at the minimum energy σ is increased from 0.47 nm to 0.57 nm, in order to avoid phase separation and disturbance to lattice packing uniformity.

For the multiple polymer chain conjugation studies in Chapter 4, the water solvent and its related hydrophobic effects play a crucial role in the polymer conformations and structures. Hence, we employed a combination of all-atomistic simulations with MARTINI models, while CG MARTINI simulation results are carefully examined and evaluated with all-atomistic simulation results. A representation of one helix strand and polymer conjugates structure in MARTINI model is shown in Figure 2.4.

2.3.3 Dissipative Particle Dynamics Model

Dissipative Particle Dynamics (DPD) is a Lagrangian thermostat coarse-grained simulation technique that can be used to describe pairwise hydrodynamic interactions in mesoscale materials. This method has been widely used in studying the phase separation of biomaterials such as lipid bilayers [67-69], self-assembly behavior of copolymers [70], and interaction of polymer conjugated nanoparticles with lipid membranes [71-73]. In DPD simulations, three pairwise forces act additively on each particle: a conservative force F_{ij}^C , a dissipative force F_{ij}^D , which serves as heat sink, and a random force F_{ij}^R , which serves as a heat source:

$$F_i = \sum_{j \neq i} F_{ij}^C + F_{ij}^D + F_{ij}^R, \quad r_{ij} < r_c \quad (2.12)$$

The conservative force is a soft repulsion term of the form $F_{ij}^C = a_{ij}\omega(r_{ij})\hat{\mathbf{r}}_{ij}$, where $\omega(r_{ij})$

a_{ij}	W	P	A	H
W	25	26.3	100	26.3
P	26.3	25	100	20
A	100	100	25	100
H	26.3	20	100	25

Table 2.1 Interaction parameter between beads i and j , a_{ij} . The magnitude of a_{ij} denotes the maximum repulsion that the particles will experience. H, P, A, W represent helix, PEG, alkyl chains and water beads, respectively. Parameters are adopted from Groot [2], and calibrated to match experimental studies [3, 4].

is a normalized distribution function:

$$\omega(r_{ij}) = \begin{cases} 1 - \frac{r_{ij}}{r_c} & (r_{ij} < r_c) \\ 0 & (r_{ij} \geq r_c) \end{cases} \quad (2.13)$$

and a_{ij} is the maximum repulsion that the particles will experience, which can be derived from the Flory-Huggins theory of polymers. The interactions between different particles used in these simulations can be found as in Table 2.1.

The other two forces have the forms $F_{ij}^D = -\gamma\omega^2(r_{ij})(\hat{\mathbf{r}}_{ij}\dot{\mathbf{v}}_{ij})\hat{\mathbf{r}}_{ij}$ and $F_{ij}^R = \sigma\omega(r_{ij})\alpha\delta t^{-1/2}\hat{\mathbf{r}}_{ij}$. Here, the time unit $\tau = 24.32 \text{ ps}$ is used, and the basic length unit used is $r_c = 0.8 \text{ nm}$. Other relevant parameters are the dissipation parameter, the random noise parameter, and the timestep, for which we use values of 4.5, 3, and 0.006τ , respectively.

The driving force for micelle formation is essentially the hydrophobic effects in the amphiphilic conjugates, which emerges from the relatively lower repulsive interactions between

“like” particles (e.g. lipid-lipid repulsion is lower than lipid-water repulsion). Considering the fact that DPD model has been effectively used to model hydrodynamic interactions especially phase separation in amphiphilic molecules, we use DPD model for the micelle related studies in Chapter 6 and Chapter 7.

2.4 Phase Separation Theoretical Studies

For the theoretical investigation on phase separation in Chapter 6, sample micelles with 3 different 3helix:4helix ratios were chosen for fragmentation frequency distribution analysis (similar to MALDI spectra [74, 75]). Here, all the possible 8-bead-fragmentations in the sample micelles were classified according to the number of 3-helix component beads (from 0 to 8). The size of the fragmentation was chosen because the total number of beads in the double alkyl chain, except for connection beads, was 8. To quantify micro-phase separation, we compared the fragmentation density distribution of sample micelles with a random model and calculated the sum-of-squares error to provide a metric for phase separation.

Chapter 3 Conjugation Effects on Self-assembling Helix Bundles

It has been found out that the conjugation of helix bundles with polymers, particularly poly(ethylene glycol), does not result in unfolding of helices or a decrease in helicity, but may preserve peptide thermodynamical stability and induce controlled assembly [3, 8, 10, 24, 26, 27]. Previous studies have shown that this stabilization effect may be due to the fact that attached polymer chains can act as springs to exert forces on helix bundles, decrease peptide accessibility to solvent, and thus preserve their stability [25]. Two kinds of polymer-peptide conjugates have been designed recently by covalently attaching a single polymer chain either to the termini [76-81] or to the side of coiled coils [24]. These two families of peptide-polymer conjugates showed different behaviors; while end conjugation was found to destabilize short helices especially at high pH conditions [78, 79], side conjugation was found to enhance the stability and preserve the secondary and tertiary structure of the coiled coil through decreasing the steric hindrance between polymer chains [10, 24, 82].

The self-assembly of a coiled coil structure is generally driven by the propensity of peptide amino acids to form hydrophobic interhelical interfaces. The amino acid sequence, as well as the chain length of the peptides serve as a structure-directing motif and guides aggregation number, aggregation stability and aggregate structure [77]. The self-assembly patterns of coiled coils conjugated with polymer observed in experiments support this by showing that the coiled coil primary oligomeric state is generally retained during the aggregation process [24, 78, 79], with no large aggregates observed. For example, Shu et al. [24] showed that for all the investigated

concentrations of three-helix coiled-coil-polymer side-conjugates, no distribution of monomers, dimers, or aggregates larger than trimers was observed.

Despite advances in our understanding of coiled-coil-polymer conjugates, the influence of polymer conjugation location on the assembly of helix bundles remains to be fully characterized. In order to address this question, here we perform coarse-grained (CG) molecular dynamics simulations of trimeric coiled coils conjugated with polymer chains. The use of CG models allows for extending the length and time scales of observation while saving computational time. This method is critically important for simulating a system with a large number of peptides and polymer chains. The effect of conjugation location is studied by covalently attaching the polymer chain either to the termini or to the middle residue of each helix of the three-helix assembly. First, annealing simulations are used to investigate the thermal denaturation and melting behavior of the coiled coil with and without the polymer conjugation, and also to validate our coarse-graining approach by comparing the obtained melting data with those of experiments. Next, the self-assembly patterns of coiled coils both in the absence and presence of polymer chains on different sites are studied and the number of assembled clusters as well as the average aggregation number are compared for different cases. Finally, we investigate the side and end polymer conjugation effects on the energy of unzipping one helical unit from the three-helix assembly using metadynamics (MetaD) enhanced sampling simulations. Characterization of the free-energy landscape governing the disassembly of coiled coil for different peptide-polymer configurations enables us to explain the mechanisms of helix aggregation observed in self-assembly simulations.

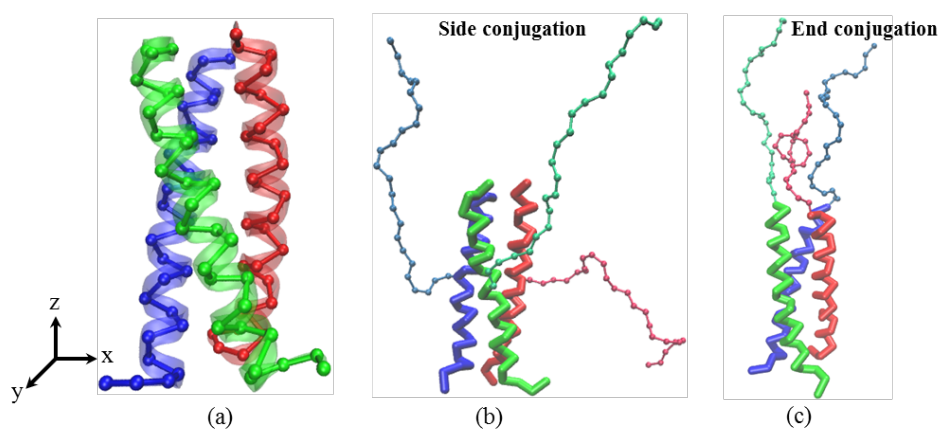


Figure 3.1 Schematic figure of CG model utilized. (a) Schematic of the coarse-grained model of the trimeric coiled coil where each residue is mapped into a single bead located at the position of $C\alpha$ atom of the atomistic structure; and (b, c) schematics of the coiled coil with side and end polymer conjugation.

3.1 Generating Coiled-coil-polymer Conjugates

In our simulation system, the selected peptide was a trimeric coiled coil, with 29 residues in each homo helical strand (pdb id “1coi” in the protein data bank [83]). In building a compatible protein coarse-grained model, we used the GO Model Builder by MMTSB Web Service [60]. For the GO model, every residue is represented by a single bead located at the $C\alpha$ position of the corresponding amino acid, hence each helix strand was represented by 29 beads, as shown in Figure 3.1 (a). All force field parameters for the protein were defined based on the GO model. More details about this model were given in Chapter 2.

GO-like models of a protein are biased toward their native configuration, and thus have been successfully used to capture the thermodynamics and kinetics of protein folding. However, one should note that the simplified CG model can give rise to some differences in the stability of higher order assembly [84]. Specifically, for GO-like models, although they can capture the folding/unfolding mechanisms of single helical units, they have some limitations in modeling the

hydrophobic interactions and salt bridges between the helical units that stabilize the coiled coil tertiary structure. The absence of explicit solvent and ions in the model makes this effect more pronounced, since the molecular organization of coiled coils forms based on burial of hydrophobic residues in the interior while exposing the polar residues on the exterior of the molecule in a water-filled environment. Despite these limitations, the employed model of the coiled coil can still provide us with simple means to capture basic aggregation features and thermodynamical mechanisms of coiled coils conjugated with polymers.

The polymer employed in our model was composed of 30 monomers (molecular weight of ~ 1300 Da) for one chain. Modified MARTINI CG force field of polymer was used to build the model [85], where each polymer monomer was represented by a single bead. The bonded interactions of the polymer chain, including energy terms for bonds, angles, and dihedrals, were taken from ref. [85], while for the non-bonded interactions only the entropic repulsion effects due to excluded volume were considered. As discussed above, there are experimental results on the differences between side and end conjugation of polymer chains on helix bundles. Thus, in our study, we employed two kinds of conjugations. First, we built a model with polymer attached to the residue No.15, which is the middle residue on each strand of the trimer (Figure 3.1b). Secondly, the polymer chains were attached to the terminal residue of each strand of trimer (Figure 3.1c). Since there is no solvent in our system, NVT ensemble was chosen and periodic boundary conditions were employed in the three dimensions. For all simulations, except annealing simulations, temperature was kept constant at 300 K.

It is worth mentioning that besides conjugation location, several other factors, including the polymer type and chain length, the protein sequence and size, and the environment, may influence

the behavior of protein-polymer conjugates. In a previous study [82], Hamed et al. addressed the effects of polymer chain length and solvent type (polar versus non-polar) on the stability of a peptide similar to the one employed in the current study. It was shown that PEG chains of different lengths, from 10 to 40 monomers, stabilize the secondary structure of a side-conjugated helix through forming a shielding shell around the peptide and reducing its solvent accessible surface area [82]. However, for case of end-conjugated proteins, a long polymer may lead to dissociation of the helix bundle [26, 78]. Lund et al. [26] showed experimentally that for a peptide similar to that of current study, the protein secondary structure and the coiled coil structure are preserved upon end conjugation of a polymer chain with molecular weight of 2000 Da. Based on these observations for both side and end conjugation cases, here, we selected a polymer chain with 30 monomers (molecular weight of ~ 1300 Da) as an example case study to investigate the aggregation behavior of coiled coils conjugated with polymers, with the a priori assumption that the selected length does not result in coiled coil disassembly.

3.2 Melting Behavior Investigation with Coarse-grained Model

Firstly, in order to investigate the thermodynamical behavior of our CG model, we carried out melting simulations of a single trimeric coiled coil, with the temperature starting at 300 K and being increased to 400 K in increments of 1 K. Different equilibration times, including 0.75, 1.5, 3, 6, 12, and 24 ns, were employed at each temperature, to study the effect of heating rate on the melting behavior of the protein. In order to quantify the structural stability of the coiled coil, two parameters were utilized as indicators of peptide helicity: the end-to-end length of each helical unit as well as the RMSD (root mean square deviation) of helical units with respect to the coiled coil crystalline structure, which were calculated from the simulation trajectories at different

temperatures. The annealing simulations considered three different cases: coiled coils with (i) no polymer attached, (ii) with side-conjugated polymer, and (iii) with end-conjugated polymer, to investigate the effect of the location of conjugation on the coiled coil thermal stability.

As a result, Figure 3.2 shows a linear relationship between the apparent melting temperature T_m (the temperature at which the protein is half-denatured) and the logarithm of heating rate (r), in the form of:

$$T_m = a \ln(r) + b \quad (3.1)$$

Where the fitting parameters a and b , given in Figure 3.2, are slightly different for the three cases employed in simulations. This phenomenon is comparable to a linear dependence of T_m on the logarithm of heating rate which was also observed experimentally for the collagen protein [86]. In detail, for the smallest heating rate tested in our simulations, the estimated melting temperature was ~ 360 K for protein only case and ~ 364 - 365 K for the protein conjugated with polymer. These results are in a reasonable agreement with experimental observations on the melting transition of the specific coiled coil structure studied here, which occurs around 343 - 353 K [24], even though relatively short simulation relaxation times and less degrees of freedom in the CG model may result in a slightly overestimation of apparent T_m .

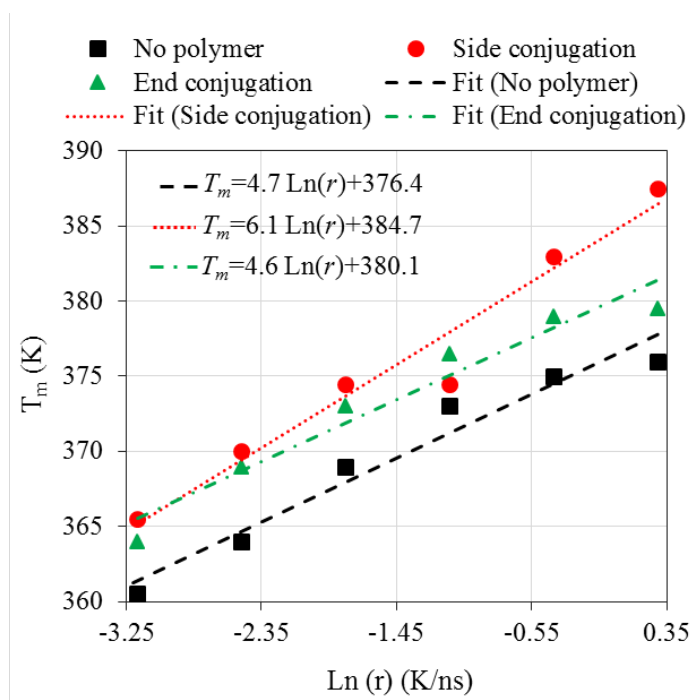


Figure 3.2 The relationship between the predicted apparent melting temperature (T_m) and simulation heating rate (r) for a single trimeric coiled coil with no polymer attached, with a side-conjugated polymer, and with an end-conjugated polymer.

In comparison among the three cases, no significant changes were observed in the thermal behavior of the protein upon polymer conjugation (Figure 3.2), which is in agreement with experimental observations of helices conjugated with polymer either at the end [87] or at the side [24]. The minor increase in thermal stability of coiled coil with polymer attachment can be attributed to the reduced structural flexibility of peptide conjugated with polymer chain [87, 88]. In addition, the simulations confirm the results of previous studies showing that the conjugation of polymer does not result in the unfolding of helical units and thus does not destabilize the helix secondary structure.

3.3 Self-assembly Pattern Dependence on Conjugation

In order to investigate the effect of peptide concentrations on its aggregation behavior, two methods were employed to control the coiled coil concentration in the simulation box. For the first method, we fixed the box volume, while the number of trimers in box varied from 5 to 30, more specifically 5, 10, 15, 20, 25 and 30 trimers. For the second one, the number of peptides in the simulation box was fixed at 27 trimers, while the box sizes varied by decreasing the dimensional distances between trimers. The first method is closer to the experimental setup, however, increasing the concentration by increasing the number of trimers existing in the box will lead to larger numbers of aggregated clusters. Thus, using this method, it would be challenging to discern the effect of peptide concentration from that of peptide aggregation propensity in the simulations. On the other hand, using the second method, we could resolve this coupling effect by fixing the number of coiled coils in the simulation box.

Similar to the melting behavior simulations, for all the simulations, three cases of coiled coils without polymer, with side-conjugated polymer, and with end-conjugated polymer were employed. All the simulation jobs ran for longer than 300 ns. To check the convergence for all the simulations, we did an analysis of assembled clusters numbers over all trajectory frames in VMD, and assume the system equilibrium within a decrease of 10%. Thus, the final 100 ns is chosen to quantify the number of assembled clusters and their average aggregation number. The reported values in this study represent the time-associated mean values and standard deviations.

In the process of self-assembly, no free helical units were observed but some helical units shuffled between different trimers, thus we calculated the aggregation number in terms of the number of helical units. In defining an assembled cluster, we considered a side-by-side distance

of 16 Å between centers of mass of helical units and an end-to-end distance of 7 Å between terminals. The selected values were tested by distribution analysis of all the distances between all the helical units in a simulation box. It has been found that side-by-side assembly (Figure 3.3a

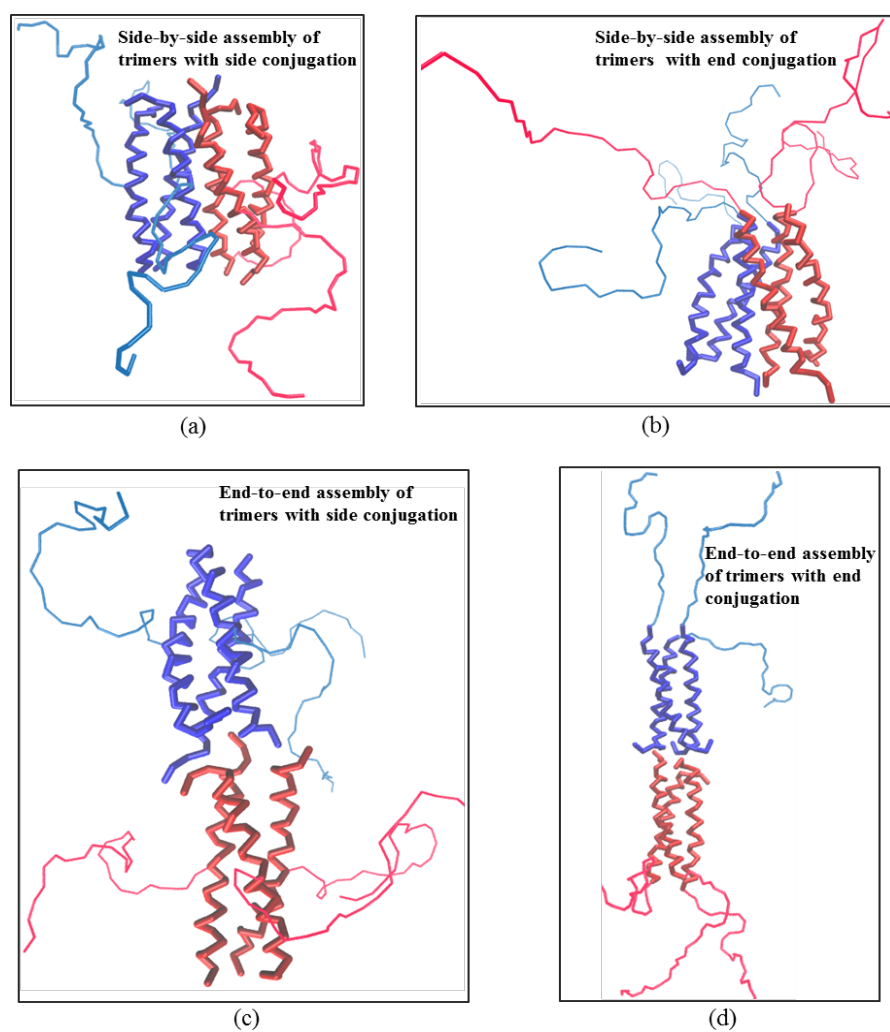


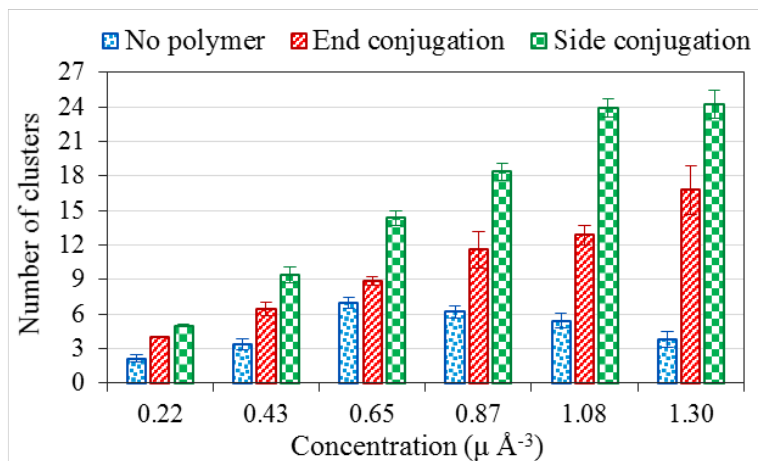
Figure 3.3 Example snapshots of self-assembly simulations showing (a, b) the more dominant side-by-side aggregation pattern and (c, d) the less occurring end-to-end aggregation pattern, for coiled coils with side-conjugated polymer and end-conjugated polymer chains.

and b) was the dominant assembly pattern for our model, probably due to stability of the initial structure of the coiled coil and the favorable hydrophobic interactions between helices, while end-to-end assembly (Figure 3.3c and d) still cannot be ignored. Hence, we used the definition above to define a cluster, considering both side and end conjugation. Aggregation number is defined as a mean value of number of helix strands in each cluster among the box, and number of clusters is the number of clusters as defined above; it is a value inverse proportional to the aggregation number for a fixed number of trimers in the system.

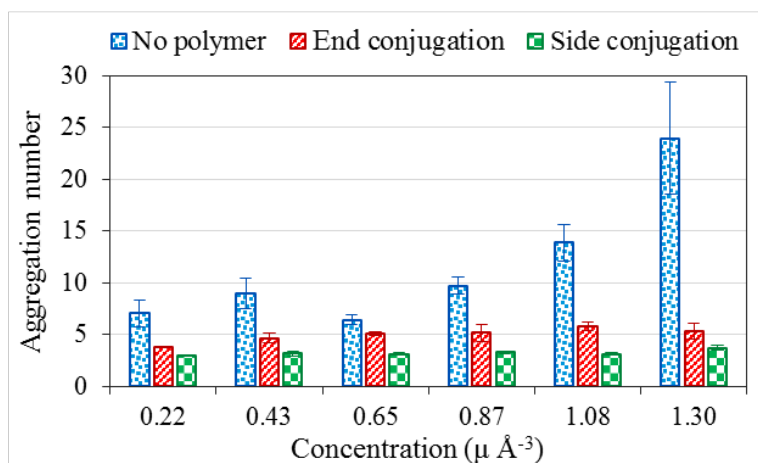
The self-assembly results for the number of assembled clusters as well as aggregation number are illustrated in Figures 3.4 and 3.5 for the two methods of changing the concentration. For the method where the box volume was fixed, the aggregation number increases with an increase in concentration (Figure 3.4b), more rapidly for the case of no polymer attached while more slowly in the presence of polymer chains. The results for aggregation number correspond well with experimental observations of micelle assembly in aqueous solutions [86]. However, the predicted results for the number of clusters are different in this method; it increases with an increase in concentration for the cases of side and end polymer conjugation, while it first increases and then decreases for coiled coils without polymer (Figure 3.4a). This observed trend for the number of clusters can be attributed to increasing the number of building blocks existing in the simulation box. For the other method where the number of peptides in the box was fixed, increasing the concentration gives rise to larger aggregation numbers but smaller number of clusters (Figure 3.5). Additionally, the results show that peptides without polymer have smaller number of clusters and larger aggregation number than both end and side conjugation cases. This finding suggests that the steric hindrance by the presence of polymer chain slows the rate of aggregation

of conjugated coiled coils compared to the case of pure coiled coils, in agreement with experimental observations of other peptide-polymer conjugate systems [79, 88]. Furthermore, helices with end-conjugated polymer have larger aggregation number and smaller number of clusters compared to side conjugation case. Thus, among the three conformations studied, with regard to propensity for aggregation, the case without polymer is the highest and the case with side-conjugated polymer is the lowest propensity one. However, it should be noted that the formation of clusters with large aggregation numbers observed for the case of pure peptides is less likely to occur in experiments where concentrations employed are much lower and the sequence specific side-chain interactions generally make dimers and trimers more favorable. As such, the CG modeling results here are meant to be qualitative assessments of the role of polymer conjugation, rather than quantitative predictions of the most likely aggregation states.

The dominated side-by-side assembly pattern can also explain why helices with end conjugation assemble more easily compared to those with side conjugation; the bulky polymer chain at the helix side makes a mushroom-like structure around the coiled coil that decreases the possibility of side-by-side assembly with other coiled coils. However, the presence of polymer chain at the terminal end of peptide interferes to a lesser degree with the side-by-side assembly pattern.

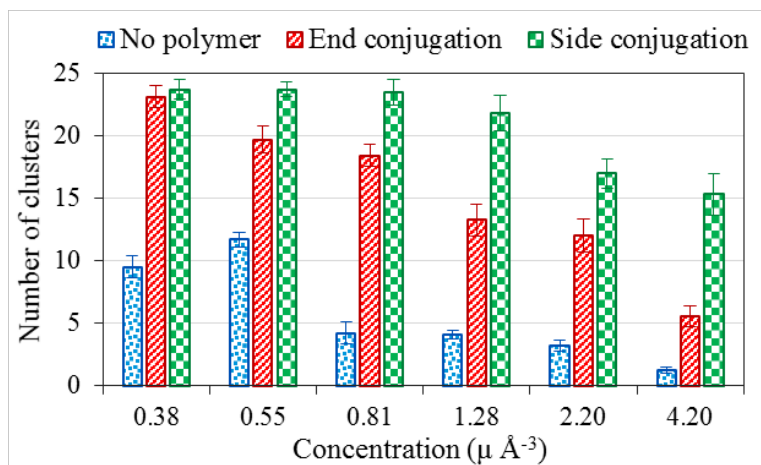


(a)

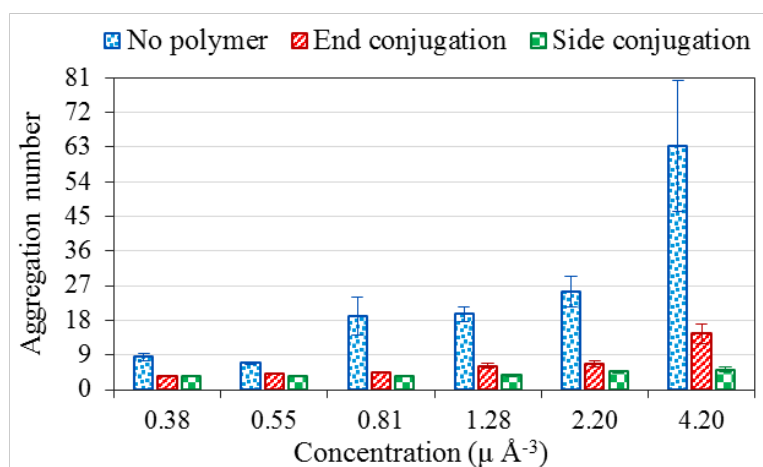


(b)

Figure 3.4 Results of self-assembly simulations of coiled coils without polymer as well as with side and end polymer conjugation showing (a) the number of assembled clusters and (b) aggregation number as a function of concentration, where different concentrations correspond to different number of trimers in a simulation box of fixed dimensions.



(a)



(b)

Figure 3.5 Results of self-assembly simulations of coiled coils without polymer as well as with side and end polymer conjugation showing (a) the number of assembled clusters and (b) aggregation number as a function of concentration, where different concentrations correspond to a fixed number of trimers in simulation boxes of different volume.

3.4 Thermodynamic Properties of Unzipping

Furthermore, in making a supplement of results of assembly simulations, a metadynamics (MetaD) enhanced sampling technique [56, 57] is employed to investigate the energy required for unzipping of a single helical unit from a three-helix assembly with or without polymer attached. MetaD simulations were performed using the PLUMED [89] plugin implemented in NAMD. In order to obtain the free energy landscape of coil unzipping, we defined the collective variable (CV), d , as the distance between the center of mass of one helical unit and the center of mass of the two others. The lower boundary, upper boundary, and width of the CV were selected as 6 Å, 30 Å, and 0.1 Å, respectively. The bias Gaussian functions with a hill height of 0.005 kcal/mol were added to the system every 1000 time steps.

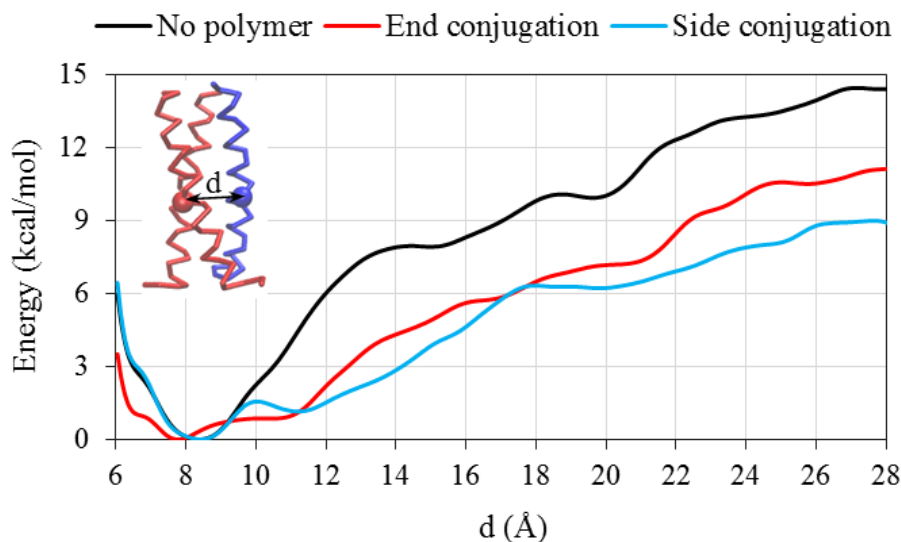


Figure 3.6 Results of MetaD simulations showing the energy required for unzipping of one helical unit (shown in blue) from the three-helix bundle without polymer, with side-conjugated polymers, and with end-conjugated polymers. The collective variable d is defined as the distance between the center of mass of one helical unit and the center of mass of the two others.

The results given in Figure 3.6 show the unzipping energy along the reaction coordinate d , for the cases of coiled coil with no polymer, with side conjugation, and with end conjugation. The unzipping energy is the highest for the case of no polymer and the lowest for the side conjugation, with the end conjugation case in-between. These results support the observations of self-assembly simulations that helices without polymer attachment have the largest tendency to aggregation, and thus more energy is required to disassemble them. However, the energy of disassembly decreases upon polymer conjugation, possibly due to the entropic effects of the polymer chain. It should be noted that the energy landscapes of helix unfolding and coil unzipping are distinctly different, and while the polymer conjugation may stabilize the helical units against unfolding (as depicted by a slight increase in the melting temperature of peptide in the presence of polymer chains), it probably has the adverse effect for unzipping. In a previous study, the unzipping energy landscape is characterized using an all-atomistic structure of a coiled coil similar to that of current study in an explicit water solvent and found that coil unzipping occurs in a sequential manner where heptad repeats of the unzipped coil first unfold and then detach from the hydrophobic core one after another in a row [90], giving rise to a number of local minima in the energy landscape pertaining to unzipping of each heptad repeat. Here, while we still observe the coupled unfolding/unzipping effects, the simple nature of the CG model and absence of explicit solvent do not allow us to resolve the individual events of detachment of heptad repeats from the hydrophobic core from the energy landscape. Thus, only two states of complete attachment and complete detachment can be identified.

Our results indicate that while simple CG models are useful in capturing the general structural features of polymer-peptide conjugates and the effects of steric interactions on assembly

processes, their accuracy in predicting the energetics of assembly/disassembly is somewhat limited. Alternative systematic coarse-graining approaches similar to recent techniques established for polymers [91] may need to be utilized in the near future to improve the accuracy of coarse-graining methods for proteins.

Chapter 4 Multi-PEG conjugation effects

In the previous studies, single polyethylene glycol (PEG) conjugation onto coiled coil structure has been observed to preserve the peptide helical structure, both in experiments [24, 92] and computational simulations [10, 25]. Also, longer PEG chains with larger molecular weights have been shown to provide a better stabilization effect due to a larger reduction in the peptide solvent accessible area [25]. In addition, PEG conjugated onto the end termini and at the middle side of the helix bundle appear to have different conformations and thus stability effects. However, there have been no studies so far about conjugation of multiple PEG chains on helix bundle surface. We know that prior studies on polymer conjugation onto surfaces and particles have revealed that mushroom and brush regimes, defined chiefly by the density of the conjugation and chain length, have been found to have quite different properties, including different polymer conformations on a substrate or surface [23, 93-97]. One standing question about helix-PEG conjugates is if multiple PEG chains are conjugated onto the helix surface, will they form a mushroom-like region, with conformations similar to the case of a single chain?

In theory, polymer chains end-grafted onto a surface or interface, with the density of attachment or molecular weight high enough, can have quite different behavior compared with flexible chains in a solution. Those chains, which are called “polymer brushes”, can often stretch away from their substrate and have much larger size [23, 98]. While the tethering distance is much larger than chain size or the chain molecular weight is small, polymer chains may be isolated from each other, and those are in the “mushroom” region instead [23].

In testing this assumption, we performed molecular dynamics simulations on NAMD, using a

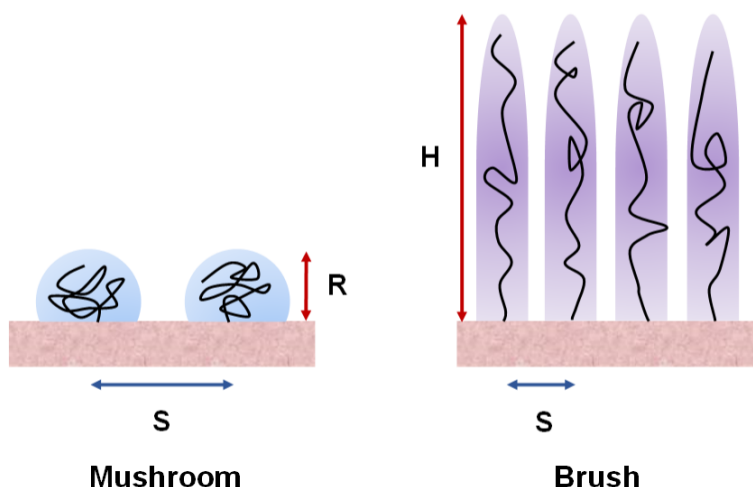


Figure 4.1 Schematic figures of polymer brush and mushroom region. For a grafting distance S much larger than polymer size R , the chains form a mushroom, while with S grafting distance much smaller than the polymer size H , the chains adopt a brush conformation.

MARTINI coarse-grained model [63] to save computational time. Additionally, all-atom simulations were carried out for shorter chains and smaller systems to check the structural stability of the peptide and also test the accuracy of CG models. Using the all-atom simulation results, helix bundle helicity is determined to investigate the helical structure and coiled coil configuration of the peptide upon the conjugation of multiple PEG chains. To quantify the size of PEG chains on helix bundle, PEG radius of gyration is calculated with varied molecular weights for both all-atom and coarse-grained simulations, which may also validate the CG model in this field of study. Afterwards, PEG chains density profiles as well as conformational distribution heatmaps will be quantified, in order to investigate the PEG chains conformational behavior on the helix bundle. At last, we will wrap up all the results by relating them to the brush theory, and make a prediction about the size requirements of polymer chains to form a brush regime on helix

bundle surface, for the sake of future research.

4.1 Building Multi-PEG-helix Conjugates

The trimeric coiled coil structure we used in this study is composed of 29 residues with pdb id “1coi” in the protein data bank [83]. On the basis of this structure, the residues at position 7, 14, and 21 of each strand of the coiled coil were replaced by cysteine in our study to make easier the attachment of three maleimide-capped PEG chains, which have been used in experiments[24, 92], to each helix. In our all-atom model, the employed PEG chains had 10, 20, 30, and 40 monomers with molecular weights of 442, 882, 1323, and 1763 Da, respectively. A schematic figure of the all-atomistic structure is shown in Figure 4.2 (a).

For the coarse-grained simulations, longer chain lengths with up to 120 PEG monomers were

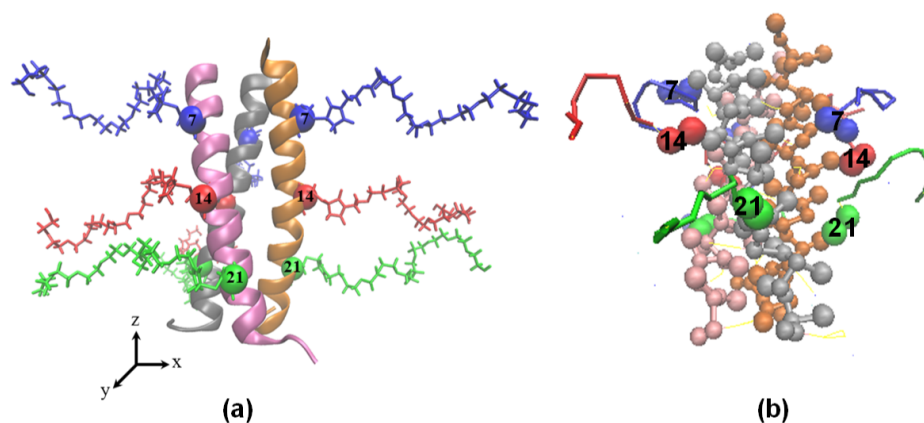


Figure 4.2 Schematic figure of the coiled coil-PEG conjugate structure, where three PEG chains are attached to residue 7 (blue chains), 14 (red chains), and 21 (green chains) of each helical strand. The trimeric coiled coil is consisting of three α -helices with a sequence of Ac-EVEALESKVAALESKVQALESKVEALEHG-CONH₂. For (a) all-atom model figure; (b) MARTINI coarse-grained model figure.

also considered. The coarse-grained coiled coil structure was constructed using the CG Builder plugin implemented in VMD [99], which uses the MARTINI model [63, 66] for coarse-graining. The coarse-grained PEG model was also built using a similar procedure, where each monomer was mapped into a single bead [85]. All those models use a CHARMM force field [100], which makes NAMD an applicable software for the simulations. A schematic figure of the coarse-grained structure is shown in Figure 4.2 (b).

In both all-atom simulations and coarse-grained simulations, the peptide-PEG conjugate structures were solvated in a water box, with 15 Å padding (TIP3P water model is used for all-atom simulations, as for the coarse-grained model, a water MARTINI model [63] is used). Periodic boundary conditions were employed in all three dimensions to avoid surface effects and obtain bulk properties. In order to preserve the water pressure constant to prevent unphysical topologies in the system, NPT ensemble was used for all the simulations. For all-atom models, simulations ran in equilibrium for 50 ns followed a 30000 steps minimization. As for coarse-grained simulations, longer simulations up to hundreds of ns were required to reach equilibrium since longer PEG chains were employed. The equilibration of simulation jobs was assured by checking the convergence of the PEG radius of gyration.

4.2 Helicity Investigation upon Multiple Chains Conjugation

First of all, all-atom simulations results are used to check the coiled coil helicity and assure that multiple PEG conjugation does not perturb the structural stability of helices. In this study, the secondary structure was quantified using the STRIDE algorithm implemented in VMD [99]. Figure 4.3 shows the average fractional helicity of the coiled coil for different PEG molecular weights. Our simulations indicate that, for all of the PEG molecular weights studied (442, 882,

1323, and 1763 Da), conjugation of nine PEG chains does not induce helix unfolding but, on the contrary, slightly enhances the helical content of the conjugated peptide compared to the non-conjugated coiled coil. This trend is in line with previous experimental [24, 76, 92] and simulation [10, 82, 101] observations of a single PEG chain conjugation. Additionally, the small values of root mean square deviation (RMSD) of the peptide structure with respect to the coiled coil crystalline structure (secondary axis of Figure 4.3) ascertain that the trimeric structure of coiled coil is preserved for all PEG molecular weights studied.

With this conclusion, we can investigate the PEG chains conformations onto helix bundle as the next step, while helix bundle can be treated as a relatively stable cylindrical surface or substrate in future discussions.

4.3 Multi-PEG Chains Conformational Probabilities Study

To quantify the size of PEG on helix surface, we calculated its radius of gyration (R_g) as in Figure 4.4. The scaling of average R_g with molecular weight generally follows the relationship

$R_g \propto M_n^N$, where $N = 0.5$ for an ideal chain [25]. Here, we present the R_g of multi-PEG chains

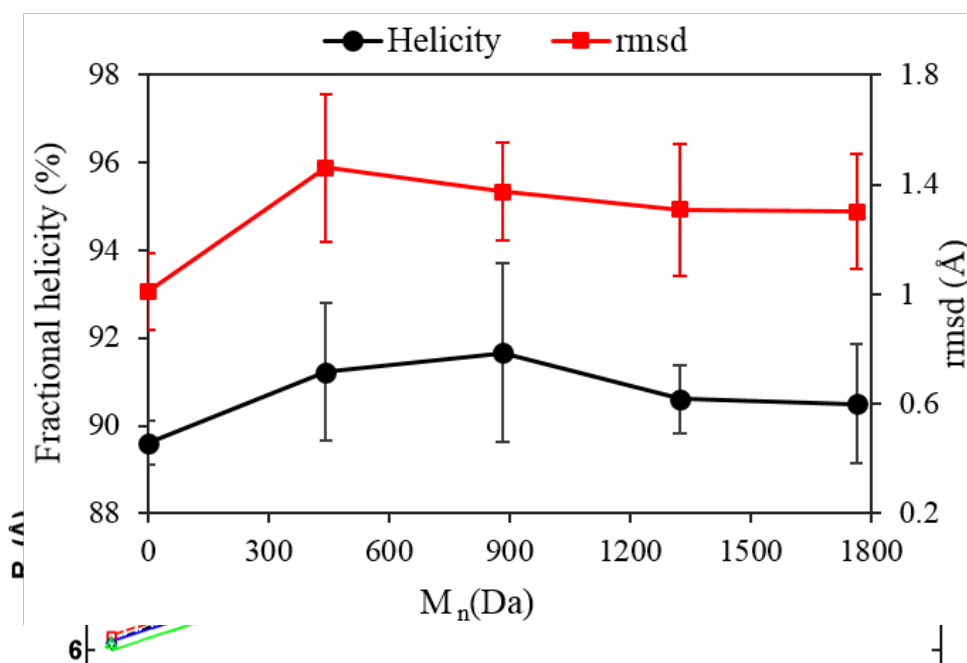


Figure 4.3 Fractional helicity of the peptide as a function of PEG molecular weight (M_n ; black solid circle markers), based on predictions of all-atom molecular dynamics simulations. The secondary axis (red solid square markers) illustrates the root mean square deviation (rmsd) of the peptide structure with respect to the crystalline structure of the coiled coil for different ^{ase} of PEG molecular weights. Both the helical content and coiled coil configuration of the peptide. are retained upon the conjugation of multiple PEG chains.

for both all-atom and coarse-grained model simulations. For the molecular weights studied, the values of R_g for the cases of single chain and multiple chains are close; they are indiscernible at low molecular weights. However, slight deviations are observed at high molecular weights, due to the confinement effects induced from other chains. One may also note that the R_g results for coarse-grained model are slightly smaller than all-atom results, due to less degrees of freedom in the process of coarse-graining. Regardless, for the molecular weights studied, R_g values for a single isolated chain versus three chains conjugated to a helix are very similar, implying that the polymer chains still adopt a mushroom-like conformation on the coiled coil surface. Meanwhile, the coarse-grained simulation results agree well with all-atom simulation results, which validates the accuracy of the coarse-grained model and makes it applicable to perform larger molecular weight simulations and to save computational time.

We also obtained conformational distribution plots of PEG chains in the xy plane of a Cartesian coordinate system and in the rz plane of the cylindrical coordinate system, based on all-atom simulation results for all the four molecular weights during the equilibrium states. In the Figures 4.5 and 4.6 below, we used red color to represent the highest probability of PEG presence and blue as the lowest presence probability. Three different types of lines highlight three PEG chains influence regions around the three helices of the coiled coil, and solid lines show the boundaries of each helix strand. As for the rz plane (Figure 4.6), z is along the coiled coil length, and r is the radial distance from the z axis as shown in Figure 4.2. We can make a conclusion based on the figure that for all studied PEG M_n , the three attached polymer chains sweep a mushroom-like region around the exterior of each helix of the coiled coil, which contributes to the enhanced structural stability of conjugated coiled coil. As the PEG molecular

weight increases, the size of these influence regions gets larger, in agreement with an increase in R_g with M_n . In addition, at lower molecular weights (10 and 20 monomers), the three mushroom-like regions around the three helices of coiled coil have more or less distinct boundaries and do not overlap significantly. However, at higher densities (30 and 40 monomers), the three regions overlap more and extend further away from the coiled coil, due to steric hindrance of bulky PEG chains and the limited space available to them on the helix surface. These findings confirm that indeed the higher conjugation density has some effect on the conformations of the polymer chains. However, the interactions between the polymer chains do not destabilize the coiled coil structure at these low molecular weights.

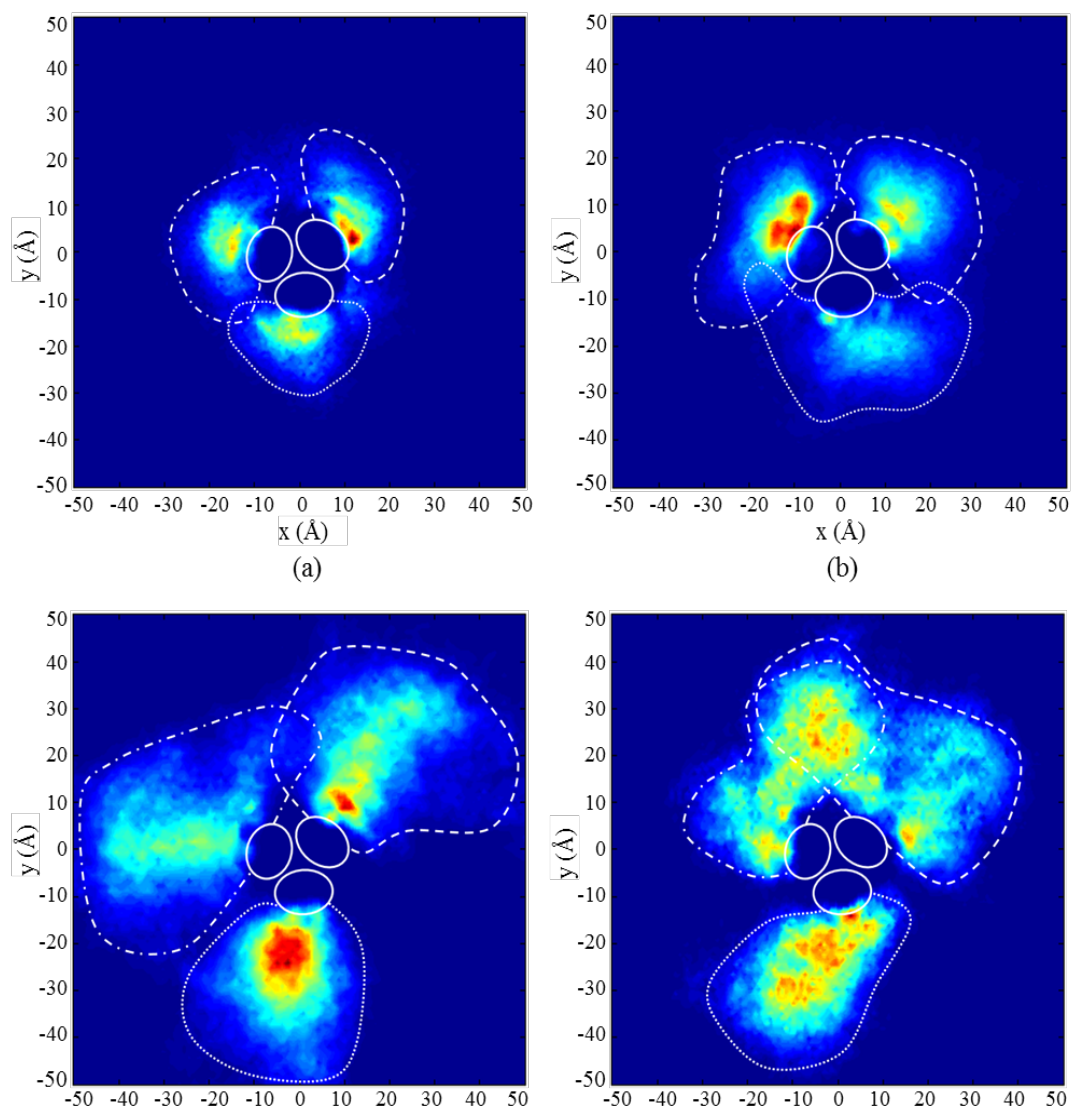


Figure 4.5 Conformational density distribution of the three PEG chains attached to each helical strand of the coiled coil for chains with (a) 10, (b) 20, (c) 30, and (d) 40 monomers. The x and y axes denote the cross-section of the coiled coil (see Figure 4.2). The boundaries of the helices are shown in solid white lines while the boundaries of PEG influence regions are depicted by dashed and dotted white lines. The red and blue colors denote, respectively, the highest and lowest values of density over the time of simulation and the color bar ranges are different for different panels.

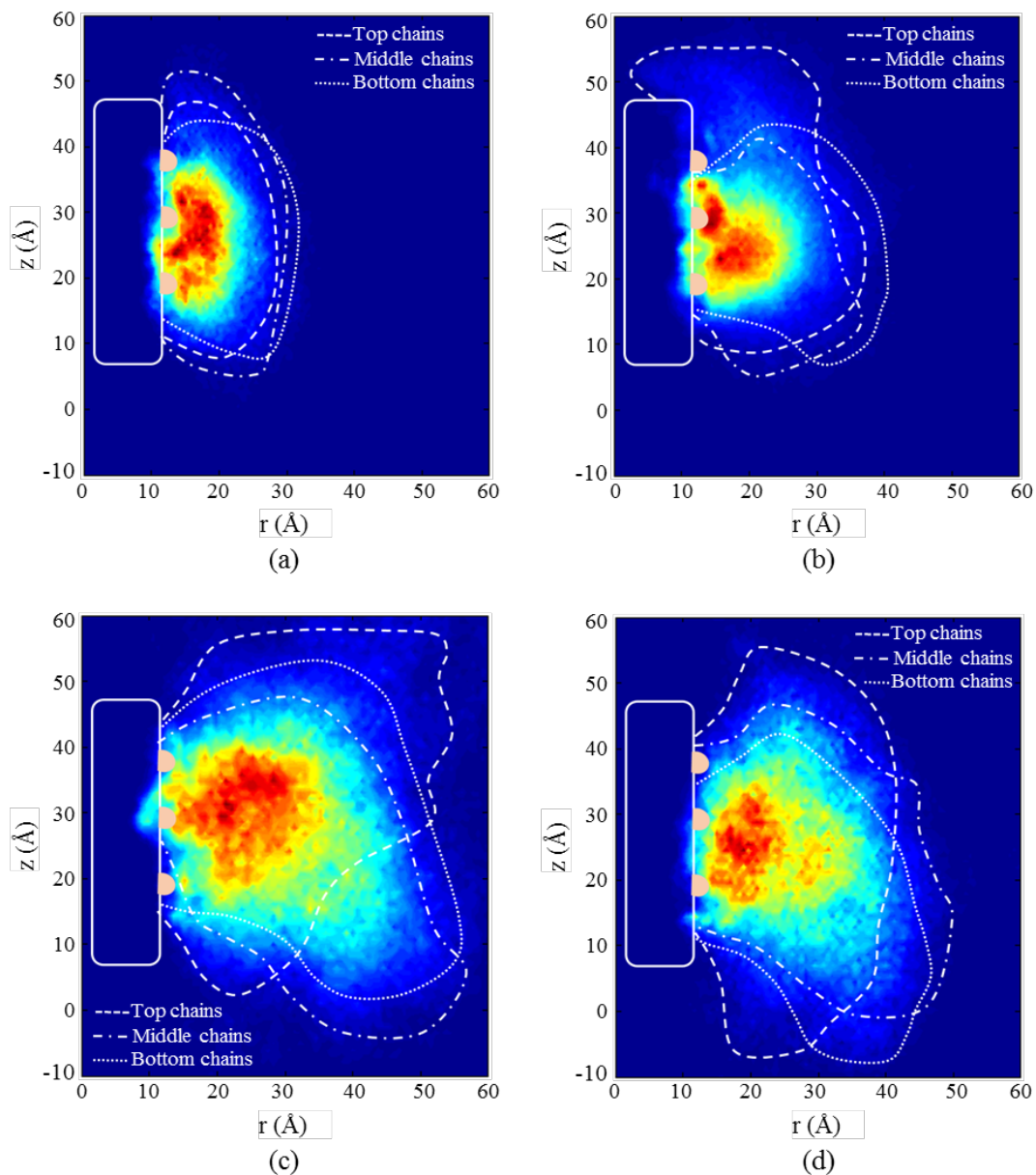


Figure 4.6 Conformational density distribution of all PEG chains attached to the coiled coil for chains with (a) 10, (b) 20, (c) 30, and (d) 40 monomers. The r axis denotes the radial distance from the z axis, which lies along the coiled coil length (see Figure 4.2). The boundaries of the coiled coil are shown in solid white lines while the boundaries of PEG influence regions are depicted by dashed and dotted white lines. The red and blue colors denote, respectively, the highest and lowest values of density over the time of simulation and the color bar ranges are different for different panels.

The r-z density maps (Figure 4.6) also show that higher molecular weight PEG chains have larger influence regions, which is in agreement with x-y plots and R_g . Additionally, they denote that in the vertical direction (along the z axis), the PEG chains have large influence regions. Thus, PEG chains prefer to extend to the helix exterior region, rather than helix bundle edges.

Furthermore, a probability density distribution profile is included for all the chain lengths studied in coarse-grained model, in order to extend the observations of all-atom simulations to larger molecular weights. Here density is calculated as the number of PEG molecules (carbon or oxygen) per volume of the region bounded between cylinders with inner and outer radii R and $R+r$, respectively. As shown in Figure 4.7, with increasing chain length and thus increasing molecular weight, the density profile has a flatter curvature, which is in agreement with both experimental and simulation results [102, 103]. Previous studies have shown steep decreasing

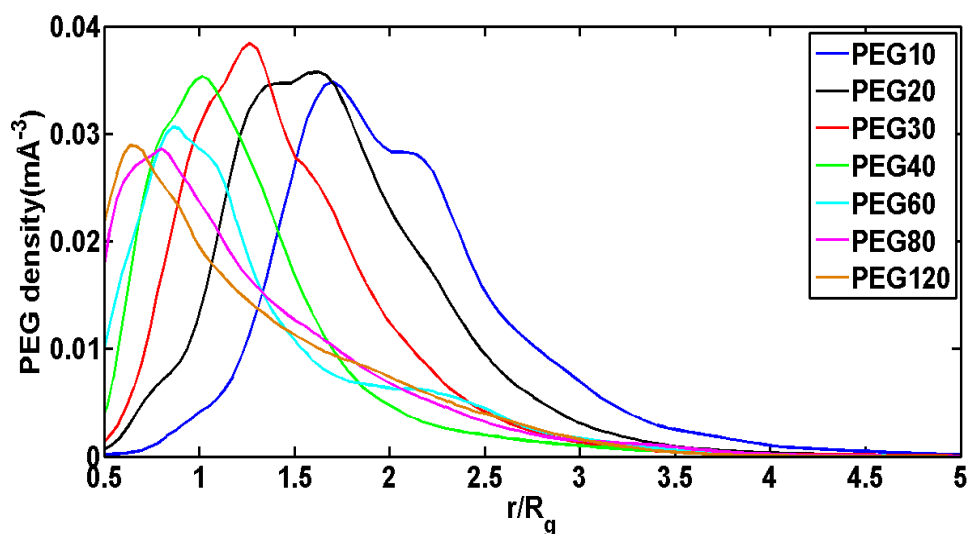


Figure 4.7 Probability density distribution profile of all PEG chains attached to the coiled coil for chains with 10, 20, 30, 40, 60, 80 and 120 monomers. The x axis denotes the radial distance of each monomer from the z center of mass of the helix bundle scaled by the radius of gyration, and the y axis denotes the distribution probability at certain distance normalized with the volume.

curvature after peak for brush-like distribution while parabolic-like density profile for mushroom region [102, 103]. For all the molecular weights, the density profile has a distinct rounded peak and a monotonic decay to zero, which are the characteristics of a mushroom conformation.

4.4 Prediction with Brush Theory

With the conclusion above, a question may rise on what chain lengths are required to transition to from a polymer mushroom to a polymer brush regime. There are a wide range of polymer tethering variations considering interface, polymer and solvent. For example, polymer can be tethered on flat planar substrates [23, 96, 97, 104], surface of cylindrical [95, 103, 105-107] or spherical [108-110]. For our case, however, we studied helix bundle, which forms a cylindrical surface with limited interaction surface, and PEG chains were end-grafted to it. In order to probe the interaction between helix and PEG and thus the conformation of PEG onto helix surface, we need to first find a criterion to distinguish brush and mushroom region.

Several theoretical works have been done to describe the behavior of polymer chains grafted on a surface. First, Alexander [111] and de Gennes [112] used a scaling theory (SF) to model each polymer chain as a sequence of “blobs” instead of Gaussian chains used in previous models. Based on this model, Self-Consistent-Field (SCF) approach, single chain mean field theory [113] and analytical solutions of SCF (ASCF) [98] were proposed to solve the problem. However, the analytical approaches, such as ASCF and SF, are not valid for shorter chains, $n < 200$, according to experimental observations [23]. Thus, in our study, we employed the Single Chain Mean Field theory (SCMF) to predict the brush region, since this theory has been found to be valid not only for smaller molecular weights similar to our case [23] but also for both planar and curved surfaces.

A reduced surface coverage is first defined as $\sigma^* = \frac{M}{S} R_g^2$, with $\sigma = \frac{M}{S}$, where M is the number of chains tethered to surface, S is the total surface area, while R_g is the bulk radius of gyration of the chain attached (mean value over all the 9 PEG chains in our study). Furthermore, we model the surface area of the helix bundle as a perfect cylinder, which has a surface area of $S = 2 \pi R l$, with $R = 16 \text{ \AA}$ and $l = 36 \text{ \AA}$ according to the model we built. Three regions are defined based on this surface coverage: the mushroom region for $\sigma^* < 1$, a mushroom to brush transition region for $1 < \sigma^* < 6$, and a brush region for $\sigma^* > 6$ [23]. Thus, in order to build a brush region, we need at least a $R_g > 27 \text{ \AA}$. Using this R_g value in our $M_n \sim R_g$ relationship [25] leads to a minimum PEG chain length of 150. However, one should also notice that this calculation is rather simple since we take the helix surface as a perfect cylinder, while PEG tends to patch onto helix surface rather than the area in-between three helices, and also the surface curvature is not considered in our formulation. Additionally, most theories have a 2D surface, while for our case, it is a three-dimensional surface with much larger stretching area. This, therefore, makes our prediction underestimated.

Moreover, for a polymer brush grafted to a cylindrical surface, the scaling of the brush thickness, H, with molecular weight is given as [94, 114]:

$$H \propto M_n^{0.75} \sigma^{0.25} R^{0.25} \quad (4.1)$$

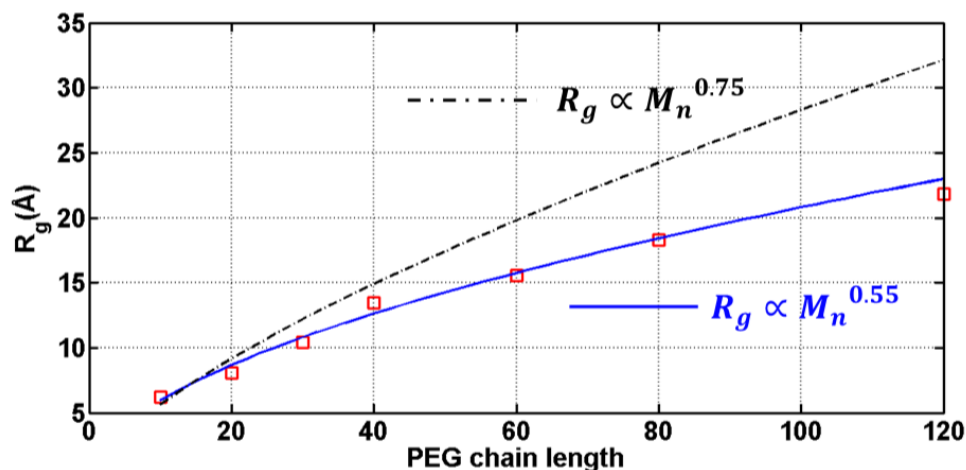


Figure 4.8 PEG chain radius of gyration trend with increasing chain length. All results are from CG model simulations; red squares indicate calculated data points, while solid blue line shows the fitting line for all simulation data, and the black dash point line depicts the predicted values of R_g if the chains were in the brush regime.

where σ is the grafting density and R is the cylinder radius. Assuming that H and R_g are related [94], it follows that $R_g \propto M_n^{0.75} \sigma^{0.25} R^{0.25}$ in the brush regime. For a given coiled coil conjugated with a fixed number of chains, the theoretical prediction of $R_g \propto M_n^{0.75}$ for a brush conformation is clearly different from our CG results of $R_g \propto M_n^{0.55}$, confirming that the system is far from a brush regime (see Figure 4.8), which is expected to occur at much larger molecular weights on high curvature surfaces such as a coiled coil. However, we continue to investigate the conjugation of much longer PEG chains or increasing the conjugation density which, according to the aforementioned theories, may make it possible to observe the formation of a brush regime in the future studies.

Our study elucidates pathways to design of new bimolecular materials with desirable

functionalities. The presence of polymer chains directs the higher order organization of peptides, such as formation of micelles [3, 33, 115] and nanotubes [116], and makes the peptides compatible with a polymeric matrix. Conjugation with multiple chains, rather than single high molecular weight polymers, may be one strategy for improving stability and compatibility in biomaterials and drug delivery applications. Our study also opens possibilities for future investigations of peptide-polymer conjugates with a broad range of polymer grafting densities. The methodology established here might eventually be useful to explore the possibility of using the conformational variability of polymer chains to generate stimuli-responsive switches that activate helix folding/unfolding upon changes in temperature, pressure, or solvent quality.

Chapter 5 Design of 3-helix Micelles with Tunable Shapes

Drug carrying micelles with tunable stability and size are needed to address challenges in delivering therapeutic compounds into cells in a targeted fashion [1, 46, 117-120]. Polyethylene glycol (PEG), which has good hydrophilic properties and biocompatibility, has become a popular building block with which to synthesize hybrid amphiphilic molecules that can assemble into micelles with appropriate nanoscale dimensions and adjustable stability [121, 122]. A new design of peptide-polymer conjugate of the 3-helix bundle peptide covalently conjugated with PEG chains on each helix strand was reported by Shu et al. [32] When these PEG-helix conjugates are further conjugated with alkyl chains, they form spherical micelles ~15 nm in size [3, 32]. For penetrating deep tissue or other biological barriers, micelles used as nanocarriers usually need to have a diameter of in the range of 10-30 nm. [44, 46]

The small diameter of 3-helix micelles makes them favorable for these applications, however, the self-assembly mechanisms and molecular design parameters controlling the size and shape of these assemblies remain to be fully established. For this specific newly designed micelle, the aggregation number, which is the number of amphiphile molecules assembled in a single micelle, is one of the most common criteria to quantify the micelle size. Dong et al. found that with PEG chains conjugated farther from the alkyl core, larger micelles are formed due to better geometric packing [44]. They also found that intermolecular interactions and molecular packing dictate micelle stability [3, 44]. Systematic efforts aimed specifically at creating very stable helix micelles have previously focused on chemically crosslinking the polymers of the outer shell layer [123-126]. Covalent networks formed in this fashion would stabilize the micelle at the

expense of limiting degradation, which compromises the drug release process [127]. In the case of PEGylation without crosslinking, it is possible that intermolecular cross-interactions between the polymer chains give rise to some cohesion forces between subunits, which may help provide some stability without hindering micelle degradation. This necessitates understanding PEG conformational dynamics in assembled micelles.

In the work by Dong et al. [44], density profiles of the micelle core and shell distribution were obtained through fitting the small angle x-ray scattering (SAXS) data, where they examined how PEG chains covalently conjugated onto different sites of the peptides exhibit differences in the SAXS measurements. It was found that a combined effect of the PEG confinement under micelle morphology and the geometric packing of trimeric subunits dictated both the stability and size of formed micelles. However, the PEG chain conformational behavior cannot easily be characterized from SAXS measurements due to limited scattering contrast between peptide/PEG and consequent challenges in separating scattering contributions.

Building on the insights gained from these experimental studies, here we aim establish a simulation-driven design framework for controlling the size, shape and stability of 3-helix micelles. In order to shed light on the behavior of conjugated PEG chains and their effect on the formation of micelles, we use a coarse-grained molecular dynamics (CGMD) model based on the dissipative particle dynamics (DPD) technique to extend the length and time scales of simulation. Atomistic molecular dynamics (MD) simulations of the self-assembly of a large number of large conjugated subunits is still prohibitively expensive computationally, which necessitates the development of coarse-grained formulations for these novel systems. We first conduct a comprehensive investigation of micelle formation from subunits with different PEG conjugation

positions. The impact of PEG conjugation site on resulting micelle size is examined, and we also compare the conformation of PEG chains in micelles, on an isolated subunit (PEG and alkyl chains conjugated 3-helix bundle), and freely distributed in aqueous solution. Our analyses reveal the complex effects of the PEG chain length and conjugation location on chain conformation, packing, emergent micelle structure and internal mobility. Through quantitative studies and analysis on the conjugated position's effect on micelle morphology and dynamics, we provide a computational phase diagram that summarizes the range of molecular weights and possible conjugation locations for stable spherical micelle.

5.1 Modeling Approach and Force Field Terms

Our system consists of a coiled coil consisting of three alpha helical peptides, with each helical strand conjugated with an alkyl chain on N terminus and a PEG chain on the residue position 7, 14, 21 or 28. As a representative 3-helix bundle, here we study a peptide that consists of 29 residues on each strand. The atomistic structure of this triple helix coiled coil is available in the Protein Data Bank (PDB ID '1coi' [83]). Given the length and time-scale limitations of all-atomistic simulations, here we choose to establish a coarse-grained molecular dynamics simulation methodology for this system. The model parameters include those for the peptide, for the conjugated polymer chain, the alkyl tail group, and the solvent environment, which in this case represents water. Our goal here is to evaluate the effects of PEG conjugation position on micelle formation and stability. We investigate systems with three different conjugation positions that have recently been synthesized by Xu group: the PEG chain is attached to each helical strand on (i) residue 7 (near N-terminus, denoted as "P7"), (ii) residue 14 (in the middle of strand, denoted as "P14"), or (iii) residue 28 (near C-terminus, denoted as "P28").

For these amphiphilic conjugates, previous experiments and simulations have reported that the triple helix coiled coils maintain their secondary (helix) and tertiary (coiled-coil) structure regardless of PEG conjugation site or density [32, 76, 101, 128, 129]. In fact, a slight increase in helix stability can be seen due to the shielding effect of the conjugated PEG chains and enthalpic interactions between PEG and peptide surface [25]. Based on both experimental and computational analyses, here we assume that conformational changes within the coiled coil are negligible during self-assembly. Therefore, for computational efficiency, we model the 3-helix peptide domain as three homogenous rigid rods, with every residue represented by one single hydrophilic bead for computational efficiency. This approach has been frequently used and proven to be efficient in protein modeling [130, 131]. To mimic the peptide's coiled coil tertiary structure, each rigid rod was rotated 16.71° to fit the helix end-to-end vectors. A schematic of the coarse-graining procedure is shown in Figure 5.1 (a).

Our polymer conjugate model is modeled after polyethylene glycol (PEG), which is the most commonly employed polymer in polymer-peptide conjugates including α -helices [3, 76-81]. We investigate the conformational behavior of PEG chains and their effect on micelle formation by adopting coarse-grained (CG) MARTINI parameters for PEG that were recently developed by Lee et al. [132]. A previous study conducted by Li et al. [71, 133] on PEGylated nanoparticles has validated this model when used with the DPD technique. In this model, each PEG monomer is mapped onto one single hydrophilic bead. The bond and angle term parameters of the PEG chain are taken from ref. [132], but are expressed in terms of DPD reduced units; while the non-bonded interactions are mapped to the conservative force F_{ij}^C in DPD. For studying the effect of the conjugation site on self-assembly, we keep the length of the PEG chain constant at degree of

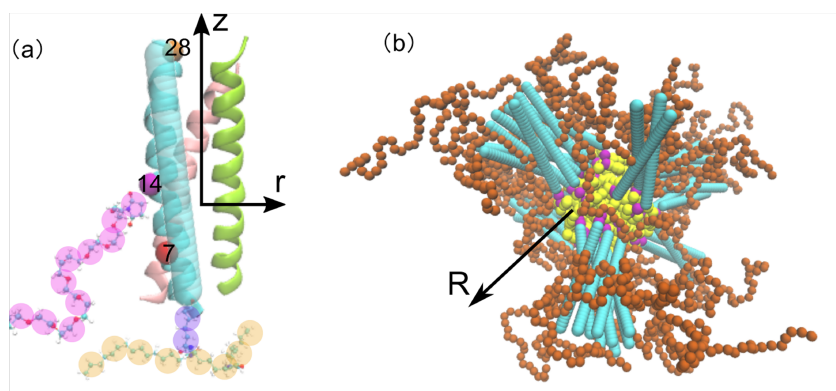


Figure 5.1 (a) Schematic figure of a 3-helix bundle with the PEG chain and the alkyl chain conjugated on one strand, the cylindrical coordinate here originates in the center of the whole triple helix bundle, with z axis along the average center of the 3-helix bundle and r axis vertical to the length of triple helix bundle and (b) a sample micelle (aggregation number is 15) from simulation results, with PEG conjugated on position 14, R here indicates the distance to the micelle center of mass. The helical strands (cyan) together with their conjugated PEG chains (pink) form the shell of this spherical structure, while the alkyl chains (yellow) and their connection points (purple) to the helical strands form the core of the sphere. Figure (a) shows the coarse graining method of one single helix strand together with polymer chains conjugated on it.

polymerization $DP = 44$ (molecular weight ~ 2000 Da). This is comparable to designs that have been recently characterized experimentally [4, 26]. We also investigate molecular weight effects on self-assembly separately, by studying four different cases, specifically $DP = 10, 20, 30,$ and 60 .

The lipid hydrophobic tails linked to the N-terminus of the peptides were also modeled using the DPD method [67, 68]. In our simulations, the hydrophobic tail contains two linker beads, directly connected to the end of each helix strand. Two alkyl chains are connected to the linker group (see schematic Figure 5.1 a). Each alkyl bead represents a three to one mapping of atoms to beads, and has roughly the same liquid volume as the PEG bead. All the alkyl beads including linkers are hydrophobic in water. Bond and angle terms as well as non-bonded conservative force

interaction parameters of the alkyl beads were adopted from ref. [67, 68, 71].

5.2 Simulation Details for Self-Assembly Studies

Each system simulated consists of 100 amphiphilic subunits. These subunits are randomly distributed in the box using Packmol [134]. We also study mixed systems of P7, P14, and P28 at equal ratio, where the total number of molecules is 99. All systems are solvated in water to satisfy a particle density of 3 beads per unit cubic volume. All simulations are carried out for approximately $0.9 \mu\text{s} \sim 1.5 \mu\text{s}$, and tend to reach equilibrium before 800 ns. The equilibration of each simulation is assured by checking that the average micelle aggregation number is a stable value that does not decrease or increase by more than 3 in 200 ns. The last 150 ns of the whole simulation are chosen for data analysis. As suggested by the error bars on Figure 5.2, and discussed below, the assembled micelles show a distribution of sizes. We consider subunits as members of a micelle when their alkyl chains are within a distance of $3 r_c$ from each other. The aggregation number here indicates the number of peptide-polymer conjugates (including one peptide strand together with the conjugated PEG and alkyl chain) in an assembled micelle. In the studies of PEG conformational behavior, we focus on assembled micelles that agree with the experimentally known sizes in order to make direct comparisons between simulation and experiment. For micelles with PEG conjugated to P7, P14, and P28, we chose micelles with aggregation numbers of 27, 45, and 54 monomers respectively [44]. To validate the PEG model in our DPD simulations, Table 2 compares the R_g and R_{ee} predicted from our DPD PEG model with experimental results [26, 132].

We report values for a free PEG chain in solution, and PEG on an isolated subunit for all PEG

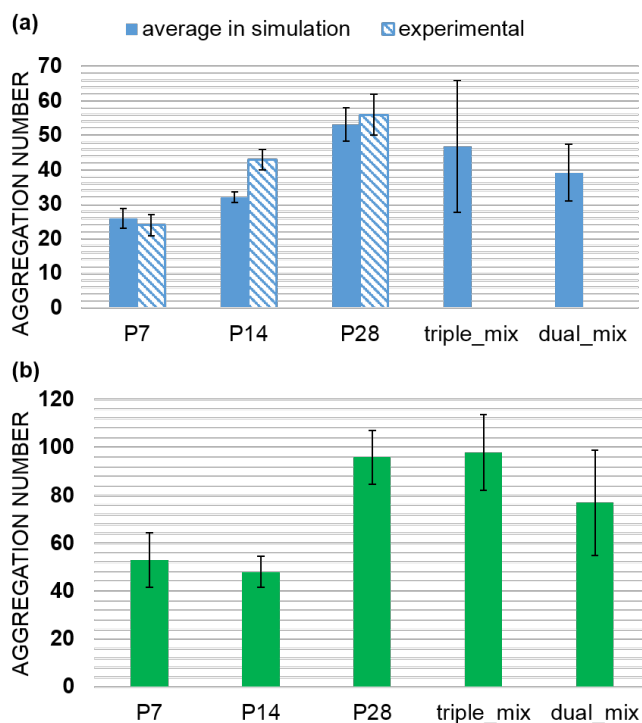


Figure 5.2 Size of the micelle (aggregation number) as a function of different PEG chains conjugated sites. Figure (a) shows the average micelle size in system for different cases, while (b) shows the largest micelle size for different cases. For all the three different conjugation sites (7, 14, 28), average values and standard deviations are indicated, while dual mixture case includes a mean value of the mixture P7&P14, mixture P7&P28 and mixture P14&P28.

conjugation positions and molecular weight 2000 Da. In our DPD model, PEG in solution has R_g 14.8 ± 2.9 Å, which is in good agreement with the experimental value (16 ± 3 Å) and MARTINI CGMD value (14.5 ± 0.2 Å) [132]. PEG on an isolated triple helix bundle also has a R_g value 15.2 ± 1.7 Å, which is comparable to experimental SAXS data 11 ± 4 Å (error due to the resolution of SAXS) [4, 26]. The slight difference compared with experiments might be due to the fact that in the simplified DPD model, the interaction surface area between the PEG chain and peptide is smaller. Overall, these results confirm that this model is a good representation of the PEG

conformational behavior in a conjugated state.

In the “cohesive interaction density” analysis, a cutoff distance the same as the DPD conservative force cutoff distance ($1 R_C$) is used to find the beads from other triple helix bundles in proximity to each PEG bead.

5.3 CG Model Validation with Experiments

First, we present simulations that investigate the self-assembly behavior of the PEGylated peptides. The driving force of self-assembly is the hydrophobic effect induced by the explicit water solvent molecules, which interact unfavorably with the alkyl chains. This effect causes the subunits to aggregate into larger clusters with the hydrophobic alkyl chains forming the micelle core and hydrophilic PEGylated peptides forming the shell in a reproducible core-shell structure. An example of a formed micelle can be seen in Figure 5.1 (b), which corresponds to an aggregation number of 45 monomers. The most common simulation outcome is the formation of spherical micelles comprising these self-assembled subunits. This observation can be explained by Minton’s excluded volume theory on the effects of isovolumic change on macromolecular conformations [135]. In this theory, for a constant fraction of occupied volume, rounded particles have a smaller excluded volume than anisometric ones. Even though other morphologies, such as bowl-like and cylindrical aggregates, are also observed both in experiments [136] and simulations of copolymer self-assembly, a spherical micelle is more common for amphiphiles with large hydrophilic:hydrophobic ratios and consequent relatively low aggregation numbers, such as those observed herein. Indeed, larger micelles were more frequently non-spherical in our simulations than were smaller ones. As we believe spherical micelles are most relevant for drug delivery applications, sample micelles are chosen for analysis, taking care to match the average

experimental aggregation number.

To study the effect of PEG conjugation site on micelle formation and size, we calculated several micelle characteristic parameters from the simulation results. First, we calculated the aggregation number of the largest micelle in each simulation box, as shown in Figure 5.2, to quantify the micelle size for different conjugation sites. We also calculated the average aggregation number of all micelles over three trials in order to reduce statistical variations. The average aggregation number $N_{average}$ indicates the typical micelle size for each case. The largest aggregation number, N_{max} in either scenario is indicative of the micelle stability. One should note that, in terms of N_{max} , P14 has the lowest degree of size dispersity. We also find that conjugate positions closer to the hydrophobic core result in a smaller micelle size, with $N_{average}(P7) = 26, N_{average}(P14) = 32, N_{average}(P28) = 53$, and these findings agree relatively well with experimental observations [44]. The lowest N_{max} for P14 conjugation indicates that micelles formed in this case have high sphericity, suggesting that this intermediate conjugation site may be the best option for stable micelles with controlled shape. Additionally, we present analyses on the self-assembly of dual mixture combinations and triple mixtures of P7, P14, and P28 in equal stoichiometric ratios. As shown in Figure 5.2, all mixture cases result in assembly of micelles with polydisperse sizes. We also observed large micelles forming and disassembling frequently in the simulations, especially for the P14 and P28 dual mixture case. For drug delivery purposes, an ideal drug carrier should have a uniform size and stable structure. Therefore, subunits with the same conjugation position should lead to assemblies with more reproducible size distributions.

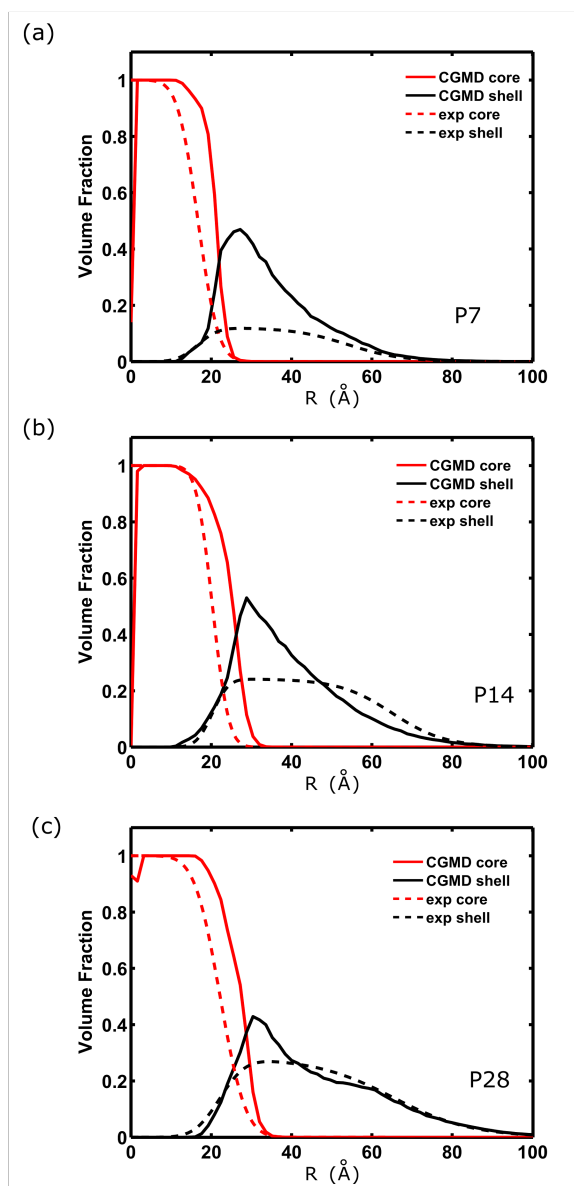


Figure 5.3 Distribution of PEG chains as a function of distance to the center of a micelle, and comparison with experiment. Three conjugation sites are included: (a) PEG chains conjugated on P7; (b) PEG chains conjugated on P14; (c) PEG chains conjugated on P28. A comparison between experimental (dashed lines) and CGMD (solid lines) is shown above. For the CGMD results, all the data are collected from the sample micelles. For both experimental and simulation data, the micelle core (red lines) comprises the alkyl chains, and the micelle shell (black lines) comprises the peptides with conjugated PEG chains.

To validate the micelle model, the radial distribution of PEG and alkyl chains by volume fraction is also presented and compared with experiment, shown in Figure 5.3 (a)(b)(c), for conjugation site P7, P14, P28 respectively. Comparing with previous experimental results on different PEG conjugation sites fitted from SAXS data, we see a good agreement both on micelle size, as well as micelle core-shell distribution.

The core size shows particularly good agreement, and both DPD and experiments report core radius size in the range of 20-30 Å. As for the PEG (shell distribution), both DPD and experiment report the same trend that PEG conjugated further from the micelle core results in a larger micelle. The parabolic distribution of the hydrophilic outer shell indicates a spherical structure, as expected. However, the SAXS data shows a smaller shell distribution area than DPD predicts, which may be due to the fact that these dimensions from experimental data are obtained using a Gaussian model for the distributions, leading to a smoother curve. The reduced attraction area between PEG and peptides in the CG DPD model results in decreased micelle shell hydration. This explains why the shell distribution curve from simulations slightly overshoots the experimental curves. Additionally, we anticipate that the coarse-grained nature of the water beads may also make them difficult to enter micelle shell region. This could be another possible reason for the underestimated degree of hydration and shell distribution in simulations compared to experiments.

5.4 PEG Chains Conformational Analyses

We can gain additional insight into PEG conformations by examining the radial distribution of each micelle component by weight fraction, as shown in Figure 5.4 (b)(c)(d), for conjugation site

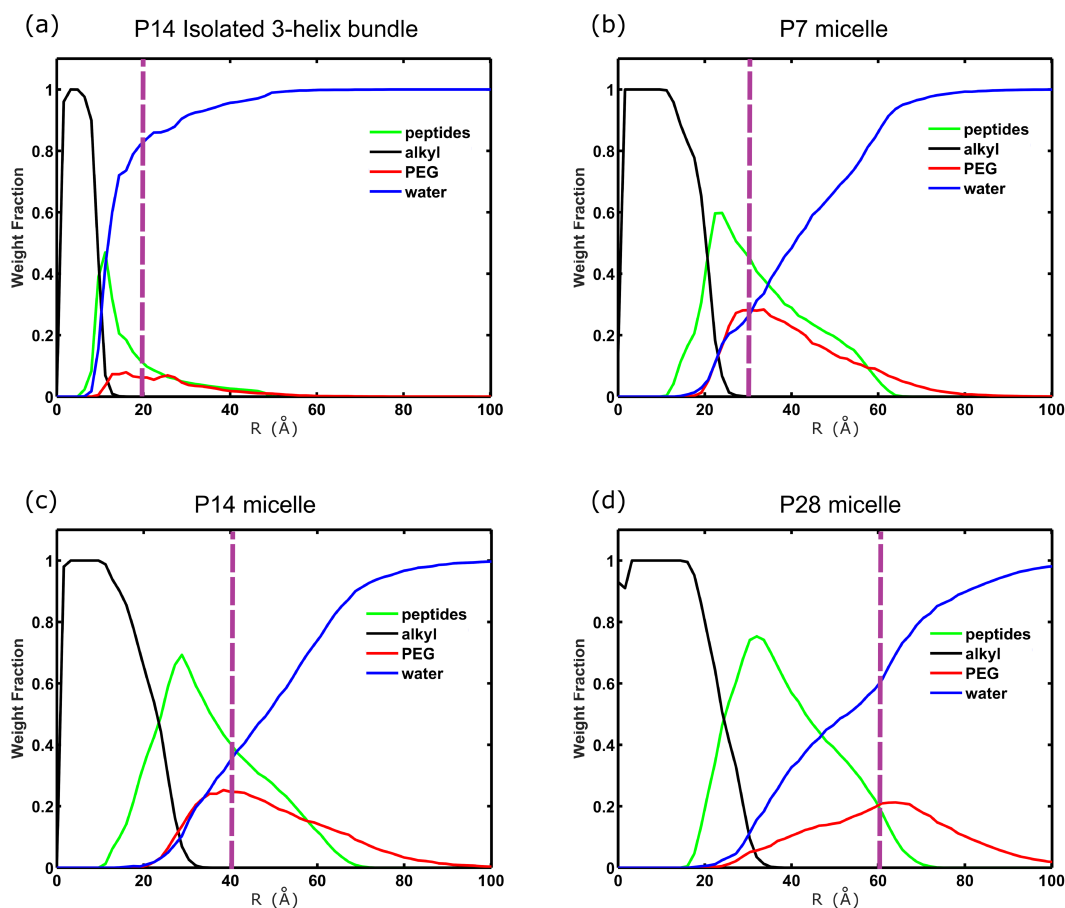


Figure 5.4 Distribution weight fraction of all micelle component beads and water beads as a function of distance to the micelle center of mass, including cases for all the three different PEG conjugation sites. (a) PEG chains conjugated on P7 of the isolated triple helix bundle; (b) PEG chains conjugated at P7 in the sample micelle; (c) PEG chains conjugated at P14 in the sample micelle; (d) PEG chains conjugated at P28 in the sample micelle. Green lines indicate the peptide distribution, black lines indicate the alkyl chain distribution, red lines indicate the PEG chain distribution and blue lines indicate the water distribution. The dash dot magenta lines indicate the estimated position of each conjugation site.

P7, P14, P28 respectively. As expected, conjugating the PEG molecule further away from the micelle core shifts the PEG distribution outwards towards the micelle periphery. The P28 micelle shows a much flatter distribution that extends to the outer region of the micelle. The greater free volume available at the periphery of the micelle decreases the likelihood of individual PEG chains contacting neighboring chains. Comparing Figure 5.4 (b)(c)(d) to PEG on a single subunit

at P14 in Figure 5.4 (a), we see that all PEG distributions within formed micelles have distinct peaks, while the peak is not clear on isolated helix bundle. These are suggestive of possible enthalpic cohesion with other PEG chains, or alternatively, reduced entropic penalty.

To further understand the factors governing the conformation of PEG chains near peptide surfaces, we analyze the probability distribution of the PEG atoms in a heat map. Here, we compare the PEG distribution on an isolated triple helix bundle on P14 Figure 5.5(a) and in a formed micelle (Figure 5.5 (b), (c), and (d), representing P7, P14 and P28 cases respectively. First, it is clear that the PEG chains adopt conformations where most atoms are close to the triple helix bundle, due largely to the fact that the surface of triple helix bundle and PEG polymer chains are both largely hydrophilic according to the DPD parameter assignments. However, the average PEG distribution in the radial direction of micelle grows from ~ 5 nm to ~ 8 nm in micelle formation, when we compared Figure 5.5 (a) and Figure 5.5 (c), marking a slightly more extended configuration. This suggests that there exists a cohesive interaction between PEG chains from neighboring triple helix bundles that leads to enthalpic interactions that promote this configuration. Considering the fact that P7, P14, P28 on isolated helix bundle has similar PEG distribution size in the radial direction of micelle, this reveals a possible mechanism for stabilization of the PEGylated 3-helix micelle, namely that the self-attracting PEG chains act as noncovalent linkers in the micelle shell that promote cohesion of the micelle.

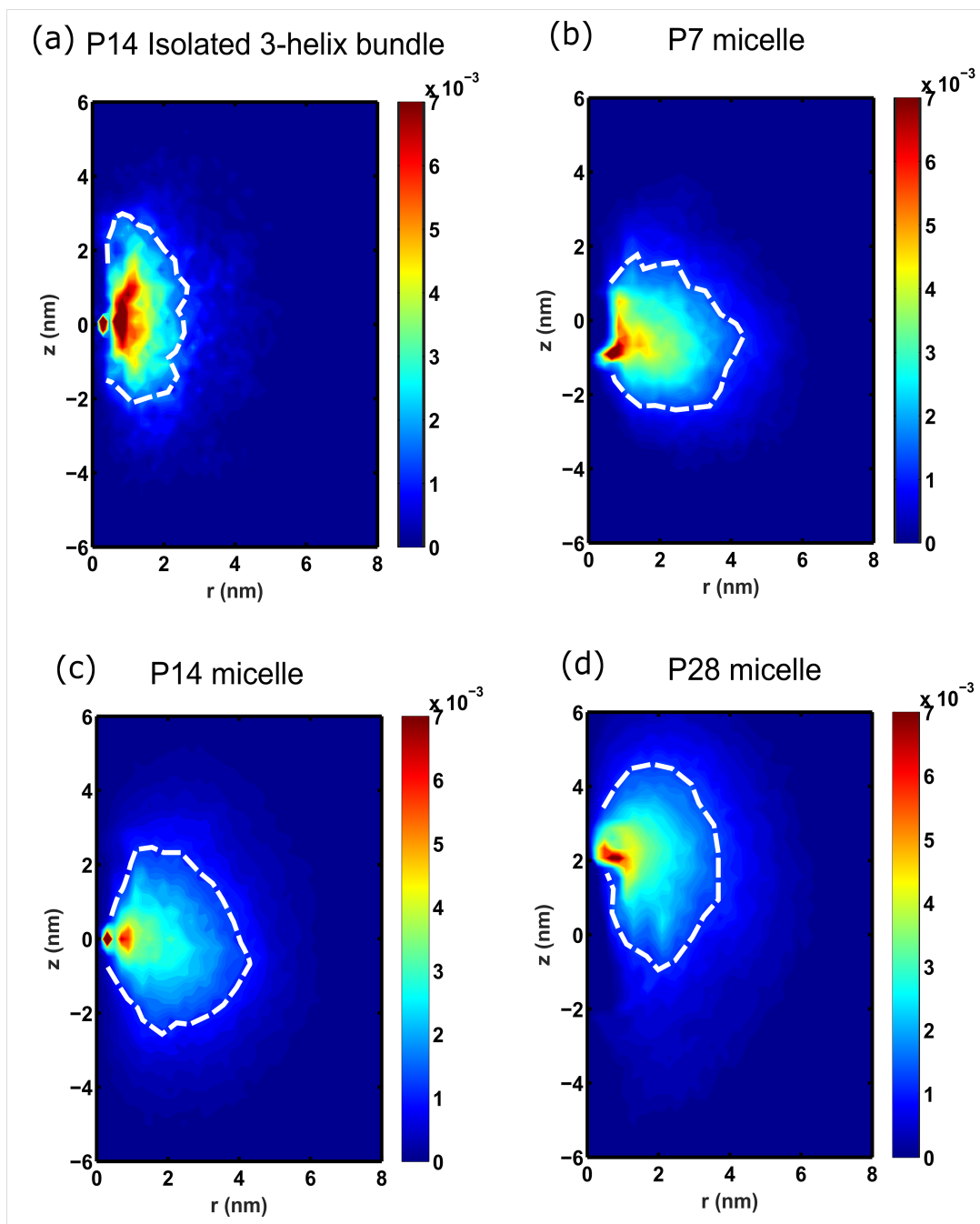


Figure 5.5 PEG chain distribution plots for four different cases, including (a) PEG chains conjugated on the isolated triple helix bundle; (b) PEG chains conjugated at P7 in the sample micelle; (c) PEG chains conjugated at P14 in the sample micelle; (d) PEG chains conjugated at P28 in the sample micelle. The color bar shows the distribution probability decrease from red to blue, the white dashed line in each plot indicates the distribution area with a probability larger than 2×10^{-3} .

Next, we present results on PEG chain radius of gyration (R_g) and end-to-end distance (R_{ee}) to quantify their conformational behavior. We report values for a free PEG chain in solution, PEG on an isolated subunit, as well as PEG in the micelle form for all PEG conjugation positions and a molecular weight of 2000 Da. PEG chains conjugated on the isolated subunit occupy a smaller space than free PEG in solution according to experimental data [4] and R_{ee} values. We note that the relationship between R_g and R_{ee} changes after polymer conjugation, and also after the micelle formation. Specifically, $R_{ee}^2 \approx 4.5R_g^2$ for PEG conjugated on an isolated triple helix, while after micelle formation, $R_{ee}^2 \approx 6.5R_g^2$. Theoretically, a polymer chain in a random coil conformation in theta solvent, has a relationship $R_{ee}^2 = 6R_g^2$ in the equilibrium state [137]. Thus, PEG conformational behavior changes both after conjugation and in the micelle formation process. R_{ee} is the highest for PEG in the micelle, because either or both of the following reasons: 1) PEG chains are pushed away due to excluded volume effects, 2) they cohesively interact with other components in assembly. On the other hand, R_{ee} is the lowest on isolated subunit because of cohesive interaction with peptides.

		R_g (Å)			R_{ee} (Å)
		Radial	Tangential	Total	
Free PEG		8.4±3.4	13.0±3.5	14.8±2.9	37±15
On isolated subunit		9.5±2.8	11.3±2.3	15.2±1.7	32±8
In micelle	P7	9.6±0.8	13.5±0.8	17.1±0.6	43±3
	P14	9.3±0.5	13.8±0.5	17.2±0.5	44±2
	P28	10.9±0.6	12.5±0.5	17.3±0.5	43±2

Table 5.1 Average conformational size of PEG polymer chains, including radius of gyration R_g , R_g in the radial direction (along the helix bundle), R_g on the tangential direction (vertical to the helix bundle) and end-to-end distance R_{ee} in DPD simulations. The results are given by the present simulations for all conjugation sites, on the isolated triple helix bundle and free polymer chains in water with the standard deviation included. All the data presented here studied the same PEG chain molecular weight 2000 Da.

The conformation of the PEG chain can be further described by calculating the components of its R_g in the radial and tangential directions to the micelle. Specifically, here, radial direction denotes the vector vertical to the helix bundle direction, and tangential denotes the vector tangentially pointing along the helix bundle from one end to another. A previous study on polymer cross-linking in micelle revealed that with increased crosslinking, R_g decreases [124]. Because PEG chains conjugated on P28 have the lowest tangentially displayed R_g , ($10.9\pm0.6\text{Å}$ for P28 compared to $9.6\pm0.8\text{Å}$ for P7 and $9.3\pm0.5\text{Å}$ for P14 as in Table 5.1), we may conclude that the PEG chains at P28 have fewer cohesive interactions, as they are able to expand away from the micelle given the larger free volume that is available in this position. For the PEG chains at P7, their conjugation position weakens the expected cohesion effect because in this case, the conjugation site close to the core and steric hindrance from neighboring chains leads to a

competing entropic penalty effect that diminishes the benefits of cohesive interaction. This idea is illustrated schematically in Figure 5.6 (a). Additionally, the smaller average aggregation number and higher N_{max} for case P7 suggests relative dominance of the entropic penalty compared to enthalpic cohesive interactions between PEG chains, which evidently leads to poor micelle stability. However, conjugation at the P14 site results in the highest tangential R_g , hinting at heightened attractive interactions with neighboring PEG chains. As an additional measure of cohesive interaction strength, we considered the “cohesive interaction density”, calculated as the average number of PEG beads from other triple helix bundle in in proximity to each PEG bead. For conjugation sites P7, P14 and P28, the cohesive interaction densities are 0.29, 0.35 and 0.28, respectively, agreeing well with directional R_g results. This fact, as well as P14 having a relatively low tangential R_g , indicates that PEG chains conjugated on P14 have the high cohesive interaction density. Additionally, as PEG chains at P14 have enough free space between themselves and the neighboring triple helix bundle, we determine that PEG chains conjugated at P14 have the best cohesive interaction density and thus stabilization effect.

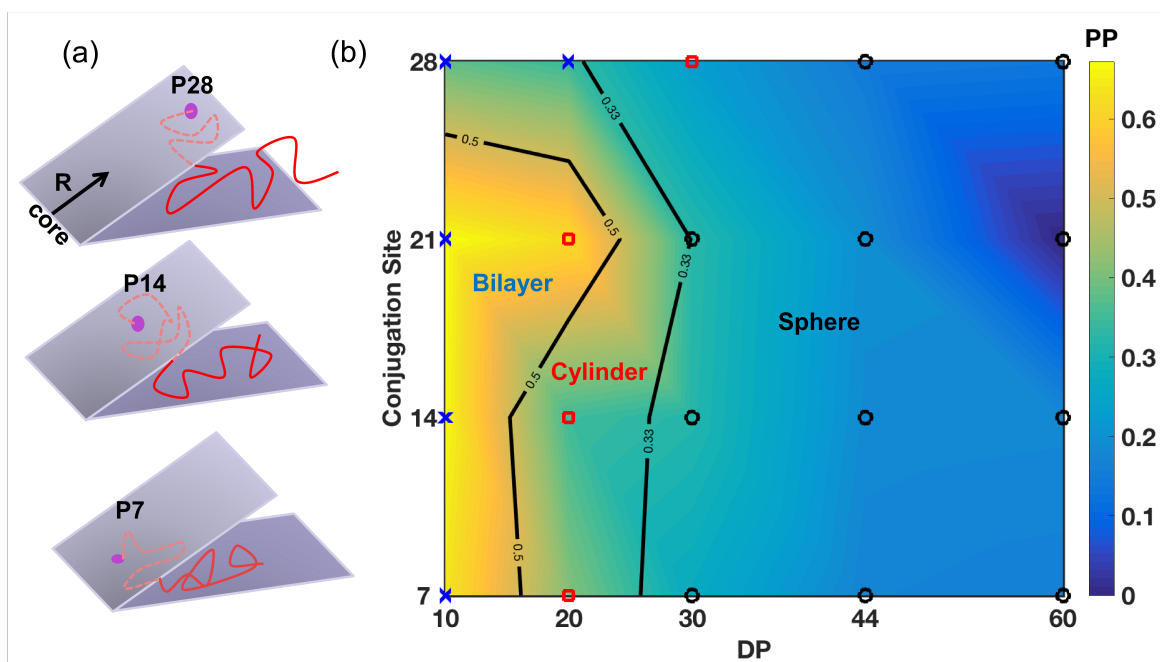


Figure 5.6 Three schematic figures in (a) on the left indicate different PEG conjugation sites with their possible distributions. Vector R here indicates the distance to the micelle center of mass, and a phase diagram (b) of the PEG conjugation sites and the PEG degree of polymerization, illustrating the predicted micelle shape, based on geometric parameters calculated from simulation. The color bar shows the packing parameter decrease from yellow to blue. Two contour lines distinguish three different micelle shapes according to theory. The points represent the visualized shape from simulations, with blue crosses indicating a bilayer shape, red squares indicating a cylinder shape and black circles indicating a spherical shape. The formed micelle shape changes from bilayer to cylinder to sphere with an increasing PEG molecular weight.

Mixtures of conjugated triple helices with different conjugation sites, however, have less overlap in PEG chain distributions than systems of a single site. As a result, the mixture of the conjugation sites largely impairs the cohesive interaction and destabilizes the micelle structure. Besides, the entropic repulsion between PEG chains and peptides [3] will exert imbalanced torsion on micelle. In summary, the mixture cases have greater likelihood to form irregular shapes and unstable micelles, which may broaden the micelle size distribution.

5.5 Micelle Shapes with PEG Conjugation Sites and Molecular Weight

Finally, we also evaluate the micelle formation for different molecular weights, and provide a

phase diagram based on micelle packing parameter considerations. The packing parameter is defined as

$$PP = V_0/a_0 \cdot l_C \quad [1] \quad (5.1)$$

to distinguish micelle geometric shape. $PP < 1/3$ corresponds to a spherical micelle, $1/3 < PP < 1/2$ corresponds to a cylindrical micelle, and $1/2 < PP < 1$ corresponds to a bilayer. Due to a negligible size of the headgroup, the traditional definition of V_0 is the alkyl core volume, a_0 is the interfacial surface area per alkyl chain, and l_C is the alkyl chain length. However, in our model, the hydrophilic head contains the peptide and its conjugated PEG chains. As the head group is fairly large and has a complex shape in our case, we use a modified definition of the geometric parameters. Specifically, V_0 is the occupied volume per subunit, a_0 is the outer surface area per subunit, and l_C is the subunit chain length. Each subunit in the micelle is a 3-helix coiled coil conjugated with PEG chains on side, and alkyl chains to the N-terminus. We used the Volmap plugin tool in VMD [99] to quantify V_0 , as an estimate of the total volume of the sample micelle normalized by the micelle aggregation number. Here we assume that the helix with PEG and water are all part of the headgroup, and in order to regularize the micelle shape, we therefore estimate the alkyl core volume and then scale up to achieve the micelle volume. Area a_0 per group is estimated as the solvent accessible surface area (SASA) of the outer surface (water) of the sample micelle (PEG chains) normalized by the micelle aggregation number. Chain length l_C is estimated as the sum of the alkyl chain length and 3-helix bundle end-to-end length. As the collected data shows in Table 5.2, the volume V_0 does not vary a lot,

chain length l_c remains the same, and the area a_0 dominates the change in packing parameter. Given that the volume is an estimation based on alkyl chain volume, it makes sense the volume does not change with DP and conjugation site. The area changes due to the positioning of PEG and DP, which affect the subunit corona angle and thus cross-section area. Due to reduced degrees of freedom in CG DPD model, the micelles formed in this system exhibit a broad distribution of sizes and shapes. As a result, unphysically large and unstable micelles may also form in simulations. These outliers cannot easily be captured by a general theoretical framework. To ensure the universality of the proposed phase diagram, instead of using the largest micelle present, a sample micelle with median size in each system is used to quantify each packing parameter from the self-assembled micelle structure. Figure 5.6(b) compares these median micelle shapes, as observed visually, to those predicted by the packing parameter theory on a phase diagram that considers conjugation site and degree of polymerization (DP) as the design parameters. Overall, the predictions from theory agree remarkably well with the visualization-based shape assignments from simulations. A few discrepancies seem to arise, particularly at the boundaries between cylinder and the other two shapes, due to the difficulty of assigning a shape purely based on visual principles. We note that for low DP PEG chains conjugated to the site nearest the core, we observe a bilayer structure, most likely due to the fact that the strong entropic repulsion of PEG near the micelle core forces the micelle to adopt a more planar configuration that releases this penalty, decrease the area a_0 and increase PP [44, 138].

As DP increases, larger area a_0 is achieved due to increasing entropic effect. Thus, subunits are more likely to assemble into a spherical micelle as DP increases. Additionally, for large DP PEG chain scenarios, our results indicate that micelles would eventually not form because of the

large entropic penalty at any conjugation site. Using this phase diagram based on the simple concept of geometric packing, we can easily reach conclusions about how conjugation DP and position may ultimately dictate the morphology of the micelles formed. We envision that these new insights obtained from simulation and simple theoretical considerations will be instrumental in synthesizing micelles with tunable size, shape and stability from a broader range of peptide-polymer conjugate building blocks in the near future.

DP	case	V_0 (nm ³)	a_0 (nm ²)	PP
10	P7	108.14	28.24	0.638
	P14	108.10	27.11	0.665
	P21	106.82	26.47	0.673
	P28	105.54	46.29	0.380
20	P7	108.73	43.95	0.412
	P14	107.79	51.38	0.350
	P21	108.03	28.90	0.623
	P28	106.38	51.71	0.343
30	P7	105.66	65.05	0.271
	P14	108.32	56.51	0.319
	P21	106.35	54.41	0.326
	P28	106.69	77.07	0.2317
44	P7	110.35	108.64	0.169
	P14	104.20	93.18	0.186
	P21	108.39	93.21	0.194
	P28	105.61	118.72	0.148
60	P7	106.96	111.17	0.160
	P14	108.86	99.52	0.182
	P28	110.21	133.39	0.138

Table 5.2 Geometric quantities that determine micelle packing parameter for different degrees of polymerization (DP) and PEG conjugation positions, including V_0 , the occupied volume per subunit and a_0 , the outer surface area per subunit. The packing parameters (PP) are given by the results of $PP = \frac{V_0}{a_0 \cdot l_c}$, from which $l_c = 6.00nm$.

Chapter 6 Micelles based on a mixture of coiled-coils

Micelle based on hybrid block copolymers has emerged as a new platform for nanocarriers that achieve tumor-selective macromolecular drug targeting via the enhanced permeation and retention (EPR) effect [38-42]. The major challenge for drug targeting is to acquire precise targeting and high delivery efficiency while avoiding non-specific binding and steric interferences from biological barriers. A tunable ligand density is necessary to strengthen the ligand-receptor binding while avoiding entropic repulsion.[139-142] Controlling the number of copies of ligands on the nanocarrier surface as well as their location is necessary to improve the targeting efficiency of nanocarriers through multivalent linkages that allow more targeted cell internalization. [143-146] Meanwhile, microphase segregation in micelles can be used to control not only the spatial distribution of ligands, but also the self-assembly characteristics of the bulk nanostructure. [147] However, in contrast to multicomponent lipid mixtures that have a well characterized phase separation behavior in membranes [148-153], there are limited reports on nanophase-separated micelles that employ hybrid polymer-peptide conjugates. In analogy with cell membranes, domain budding is shown to depend on the geometric features of the lipid units such as height, and it is expected that similar features with possibly greater diversity exist in hybrid biomaterials as well. [154, 155]

A new design of 3-helix micelle (3HM) nanocarrier based on amphiphilic peptide-PEG-lipid conjugates [3, 27, 33, 43, 44, 46, 156, 157] is reported to have the potential to provide control over the local multivalency of presented ligand clusters. Polyethylene glycol (PEG), which has good hydrophilic properties and biocompatibility, has been shown to stabilize the secondary and

tertiary structure of peptides regardless of PEG conjugation site and density [3, 25, 101, 128]. Recent simulation studies discovered that the micelle size and stability were dictated by a combined effect of the confinement of PEG chains under micelle morphology and the intermolecular cohesive interaction among PEG chains [157]. While these micelles form well-defined shapes and their size can be controlled through tuning parameters such as PEG chain length, means to control the density, distribution and orientation of ligands on the particle surface remain limited with existing designs. To this end, amphiphilic peptide-PEG-alkyl conjugates based on different coiled-coil oligomeric states offer the possibility to create multicomponent micelles with control over the availability of ligand binding sites. In the work by Ang et al. [158], the formation of self-assembled patchy micelles from mixtures of trimeric and tetrameric coiled coils was observed through differential scanning calorimetry, fluorescence recovery spectroscopy, and coarse-grained molecular dynamics simulation. It was found that the mixed micelles had high stability in serum albumin with controlled cluster size and local multivalency. However, the driving force of the phase separation shown in mixed micelles was not characterized in detail.

In this chapter, we sought to explain our previously reported self-organization of patchy phases in mixed coiled-coil micelles as a step towards prospecting them as nanocarriers. Herein, we used coarse-grained molecular dynamics (MD) simulations to investigate the self-assembly of amphiphilic coiled-coil peptide-PEG-lipid hybrid conjugates based on different coiled-coil oligomeric states. Specifically, we examined how micelles formed from 4-helix based conjugates compared to 3-helix based conjugates in terms of self-assembly kinetics as well as micelle size and shape. We revealed differences in the conformation of alkyl chains under varied coiled-coil

oligomeric states through a systematic characterization of the micelle structures. This analysis uncovered that alkyl chain geometry and packing govern phase separation, where steric restrictions were further quantified by measuring alkyl chain extension in each case. We also demonstrated variations of micelle stability and self-assembly tendency by calculating the interaction energy between alkyl chains under different oligomeric states. Size and hydrophobicity of the formulated micelles were also quantified to see if micelles could be suitable for penetrating biological barriers. We anticipate that our findings can help understand the phase separation behavior in mixed micelles with different oligomeric states and provide guidance to develop biomaterials with controlled local multivalency for tunable stability, shape and drug loading potency as nanocarriers.

6.1 Model Generation with Different Coiled-coils Oligomeric States

The two kinds of amphiphilic conjugates in AA simulations are schematically shown in Figure

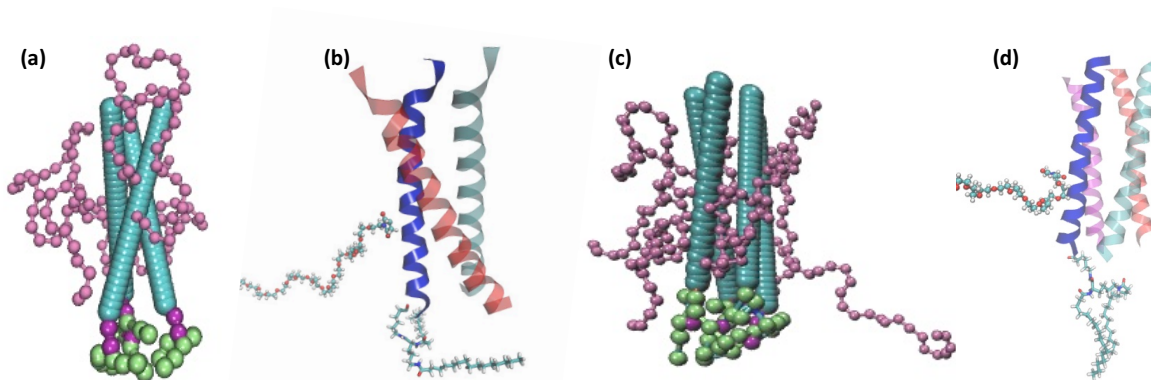


Figure 6.1 Schematic figures of MD models used in simulations: (a) 3-helix bundle (cyan) in CG DPD model with the PEG chain (pink) and the alkyl chain (purple and green) conjugated to each strand. (b) 3-helix bundle in AA model. For simplicity, only the PEG (CPK drawing method) and alkyl (Licorice drawing method) chains conjugated to the blue helix bundle are shown here. (c) 4-helix bundle (cyan) in the CG DPD model with the PEG chain (pink) and the alkyl chain (purple and green) conjugated to each strand. (d) 4-helix bundle in AA model. For simplicity, only the PEG (CPK drawing method) and alkyl (Licorice drawing method) chains conjugated to the blue helix bundle are shown here.

6.1 (b)(d). The headgroup of both amphiphiles is composed of a peptide-polyethylene glycol (PEG) conjugate, in which the peptides are coiled-coils consisting of three alpha helical strands in Figure 6.1 (b) or four alpha helical strands in Figure 6.1 (d). The atomistic structure of trimer or tetramer coiled-coil is available in the Protein Data Bank, referred as '1coi' for the trimeric helix and '1m3w' for tetrameric helix. To enable coupling of maleimide end-functionalized PEG, we performed S14C and K14C mutations on 3-helix strand and 4-helix strand respectively. PEG chain with constant degree of polymerization $DP = 44$ (molecular weight ~ 2000 Da) is conjugated on residue 14 of each helix. Two C16 alkyl chains are attached to the peptide N-terminus through Glutamic (GLU) residue as tail of the amphiphile, with a 6-aminohexanoic acid linker inserted between peptide and alkyl chains.

All the AA simulations were performed using NAMD [159] under an NPT ensemble with a constant pressure of 1 atm and a constant temperature at 300 K. The amphiphiles were solvated in an explicit water solvent using the TIP3P water model [160], and periodic boundary conditions were applied in the three dimensions. The bonded interactions were modeled using the CHARMM force field [65], long-range nonbonded interactions were modeled using the standard Lennard-Jones potential, and the particle-mesh Ewald technique were used for electrostatics interactions. The minimization of the systems run for 50,000 steps and was followed by a 1 ns equilibrium simulation using a 1 fs timestep. The equilibrium of the simulation system was assured by checking the convergence of the radius of gyration and end-to-end distance of alkyl chains.

Here we employed the same mapping method for CG simulations as in Chapter 5, which has improved its efficiency and accuracy in predicting peptide-PEG micellization behavior. [156, 157]

All CG simulations in this work were performed using a variation of the DPD approach, with the open source MD simulation package LAMMPS [161]. An NVT ensemble with a constant temperature 300 K was adopted for simulations, and periodic boundary conditions were applied in the three dimensions. Here the time scale is $\tau = 24.32 \text{ ps}$, length scale is $R_C = 0.8 \text{ nm}$. [133, 162] We investigated systems with 3-helix amphiphiles, 4-helix amphiphiles and a mixture of the amphiphiles. To reduce sampling errors, we carried out 3 duplicate simulations with different random seeds for each case. Each simulated system consists of 100 randomly distributed amphiphilic molecules (the mixture system had 50 amphiphilic molecules for each type), and then solvated in explicit DPD water beads. All CG simulations were carried out for approximately $2.0 \mu\text{s} \sim 2.8 \mu\text{s}$, and tended to reach equilibrium before 800 ns. The equilibration of the simulations was assured by checking that the average micelle aggregation number was a stable value that does not decrease or increase by more than 3 in 200 ns. The last 150 ns of the whole simulations were chosen for data analyses.

6.1 Micelle Self-assembly Process

First, we present DPD CG simulations that investigate micelle formation behaviors for 3HM, 4HM and 3&4 mixture micelles, given the same initial subunit concentration in each system. The driving force of all three kinds of micelle formation processes is the hydrophobic effect induced by the explicit water solvent molecules, which interact unfavorably with the alkyl chains. This effect causes the subunits to aggregate into larger clusters with the hydrophobic alkyl chains forming the micelle core and hydrophilic PEGylated peptides forming the shell. The most common simulation outcome for all three different cases is the formation of spherical micelles.

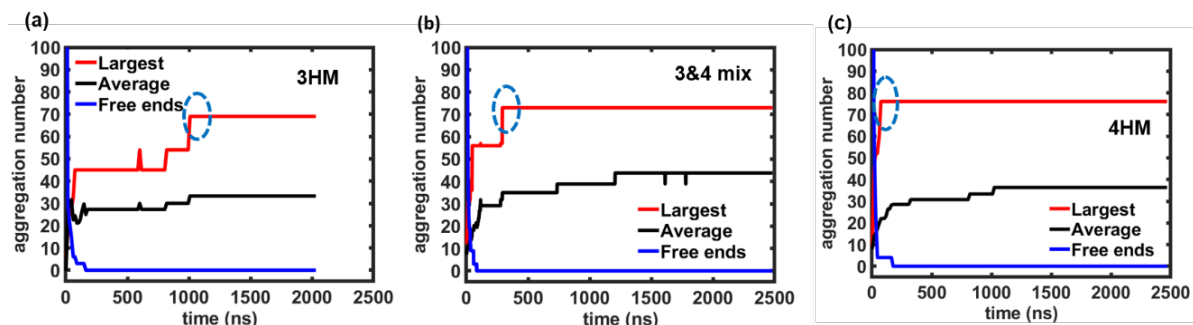


Figure 6.2 The number of free subunits in system and the largest, average aggregation number defined as the number of helices in the (a) 3HM, (b) 3&4 mixture micelle, and (c) 4HM as a function of time. The sharp increases indicating micelle fusion process are highlighted in dashed blue ovals. The results are obtained from DPD CG simulations with 100 subunits for each case.

To quantify micelle size and formation kinetics, we look at two metrics, the average micelle size and the largest micelle size. Here the micelle size refers to aggregation number, i.e. the number of helices in each micelle. We observe similar micelle sizes for the three different kinds of micelles as shown in Figure 6.2. However, the simulation time that each system takes to form the largest micelle varies, suggesting that the subunits exhibit different kinetics of self-assembly. More specifically, 3HM takes the longest time to form its largest micelle (approximately 1000 ns on average), while 4HM takes the shortest time (approximately 130 ns on average), and 3&4 mixture micelle lies in between (approximately 250 ns on average), as shown in Figure 6.3. Under the hydrophobic driving force, an individual micelle can increase its size by either combining with free subunits nearby or by fusing with other neighboring micelles. To explain the differences witnessed in the largest micelle formation time, we investigate the micelle growth behavior under these two conditions respectively. As shown in Figure 6.2(a), the largest micelle size in 3HM increases twice sharply (highlighted in blue oval), indicating that micelle fusion happens at around 800 ns and 1000 ns respectively. Regarding 3&4 mixtures and 4HM cases, we

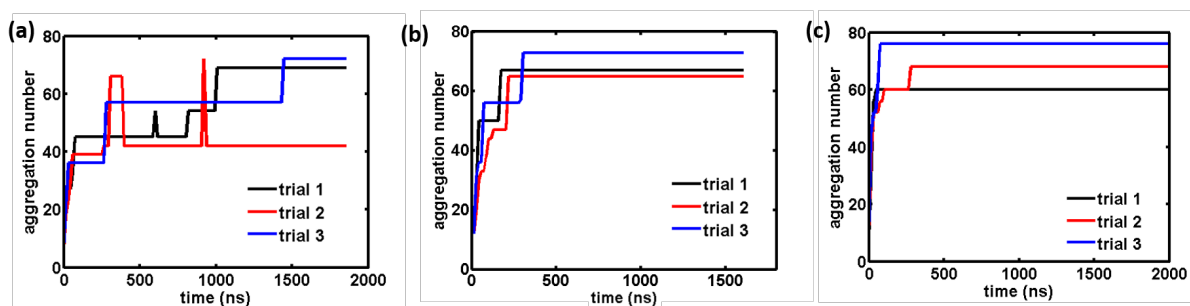


Figure 6.3 The largest aggregation number defined as the number of helices in the largest micelle in systems (a) 3HM, (b) 3&4 mixture micelle, and (c) 4HM as a function of time. The results are obtained from DPD CG simulations, including 3 different trials for each case and with 100 subunits for each system.

observe similar micelle fusion processes, but they occur much earlier in the simulation, at around 300 ns for 3&4 mixture micelle and at around 100 ns for 4HM respectively as shown in Figure 6.2 (b) and (c). A possible explanation to this phenomenon is the fact that 4HM has a stronger hydrophobic driving force due to higher alkyl monomer density and tighter packing. On the other hand, we also observe that the number of free subunits in system decrease to 0 before 200 ns for all the three cases as shown in Figure 6.2, which indicates that no more free subunits are available to join formed micelles. Beyond this early aggregation phase, the dominant mechanism of micelle size increase are the fusion events. In summary, the 4HM has the fastest micelle formation process resulting in the largest micelles, due to a combined effect of a stronger hydrophobic driving force and better packing efficiency at its core to form a spherical micelle. These effects are also present in 3&4 mixture micelles, and thus influence the shape of the mixed micelles and accelerate their formation process.

6.2 Alkyl Chain Conformations Studies

As discussed above, one of the major differences in the micelle formation processes between

3HM and 4HM is that, the 4HM appears to have a stronger hydrophobic driving force. In order to study the alkyl chain density and provide an explanation for the difference in hydrophobic interactions, we study the conformational behavior of alkyl chains on isolated subunits and in micelles using CG DPD simulations. We also corroborate these results with AA simulations that examine the conformational behavior of alkyl chains on an isolated subunit in solution. As shown in Table 6.1 below, both simulation methods reach the same conclusion that the alkyl chains on isolated 3-helix subunit bundle or in 3HM have less extended conformations than those on isolated 4-helix or in 4HM. The alkyl chains in CG DPD simulations are shorter than those in AA simulations because they have fewer degrees of freedom in CG DPD simulations than in AA simulations, and thus exhibit less steric hindrance. For star shaped polymers, M. Daoud et al. reported that if the number of polymers is sufficiently high, the structure of each polymer is stretched due to confinement effects [163]. This theory can be used to explain our observations

		3HM		4HM		3-helix components in mixture		4-helix components in mixture	
		R_g (Å)	R_{ee} (Å)	R_g (Å)	R_{ee} (Å)	R_g (Å)	R_{ee} (Å)	R_g (Å)	R_{ee} (Å)
On isolated helix bundle	AA	4.9 ± 0.2	12.5 ± 1.0	5.0 ± 0.1	14.0 ± 0.6				
	CG DPD	4.1 ± 0.1	10.7 ± 0.4	4.7 ± 0.2	11.5 ± 0.5				
In micelle	CG DPD	4.2 ± 0.1	11.2 ± 0.1	4.9 ± 0.1	12.1 ± 0.2	4.3 ± 0.1	11.2 ± 0.1	4.9 ± 0.1	12.1 ± 0.2

Table 6.1 Average conformational size of alkyl chains, including radius of gyration R_g and end-to-end distance R_{ee} in DPD simulations. The results in the table are given by the present DPD CG simulations for alkyl chains in 3HM, 4HM and 3&4 mixture micelles, alkyl chains on the isolated 3-helix or 4-helix micelles, and compares the CG DPD and AA simulation results for alkyl chains on isolated 3-helix and 4-helix micelles.

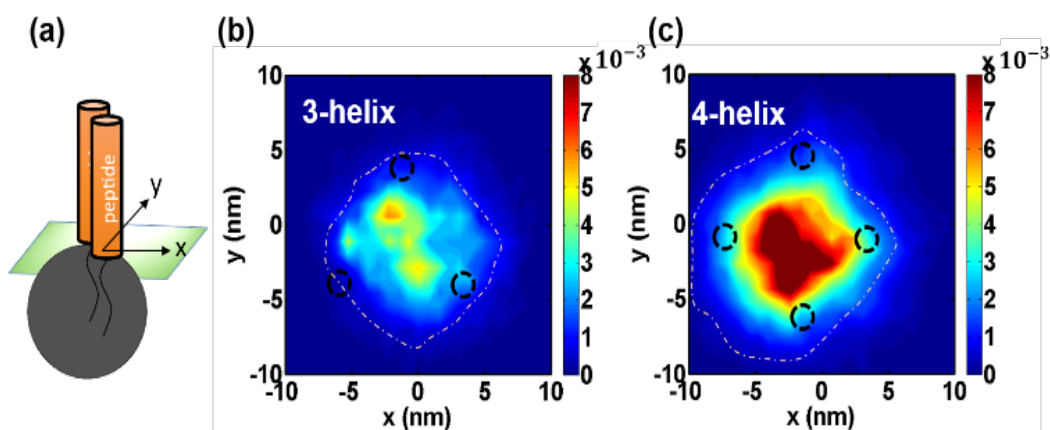


Figure 6.4 Distribution behavior of alkyl chains on the helix bundle cross sectional plane in micelles, including alkyl chains conjugated on (b) a 3-helix peptide and (c) a 4-helix peptide. A schematic figure (a) on the left shows the axis setting method in both figures: with the alkyl bead distribution projected onto the xy plane that is orthogonal to the helix bundle (radial) direction. In the figure (b)(c), the color bars in show the probability distribution decrease from red to blue, the black dashed line indicates the estimated conjugation location on the helix terminus, and the orange point dash lines indicate the alkyl chain distribution area that has a probability density value larger than 1×10^{-4} . The results are given by the present DPD CG simulations for 3HM and 4HM sample micelles with the same number of subunits over the last 150 ns after convergence.

on micelle core size: the alkyl chains in 4HM are slightly extended due to higher packing density than in 3HM.

To study the packing density of alkyl chains, we plot the conformational distribution of alkyl chains on the cross-sectional plane as shown in Figure 6.4. Note that alkyl chains in both cases have the highest probabilities within the boundary marked by the conjugation points and at the center of the helix bundle, indicating the fact that alkyl chains have relatively high attraction between each other. Comparing a 3-helix vs. 4-helix sample micelle with the same number of subunits, 4HM has much higher values of the probability distribution in its center than 3HM due to the larger number of beads in the sample micelle with the same number of subunits. Comparing Figure 6.4 (b) for the distribution area of alkyl chains in 3HM and Figure 6.4 (c) for

4HM, we can conclude that the alkyl chains have very similar area distribution sizes for each subunit. Considering a distribution probability larger than 1×10^{-4} to define the area, 3HM displays a distribution area size of 1.58 nm^2 on xy plane, while 4HM displays a slightly larger area size of 1.80 nm^2 . Since 6 alkyl chains are conjugated on a 3-helix while 8 alkyl chains are conjugated on a 4-helix, we saw a higher alkyl chains concentration for 4HM (4.46 chains/nm^2) than for 3HM (3.80 chains/nm^2). This explains the fact that 4HM has larger aggregation number and better stability. With increase in alkyl chain length, there is a corresponding higher hydrophobic interaction between alkyl chains in the micelle formation process.

6.3 Phase Separation in Mixed Micelles

Next, we present an analysis of the packing behavior of the 3-helix and 4-helix components in 3&4 mixture micelles. Combined with experimental observations [158] and phase separation analysis presented in Figure 6.5, we can conclude that the 3-helix and 4-helix components have a phase separation behavior in their mixture. Typically, experimental techniques such as MALDI

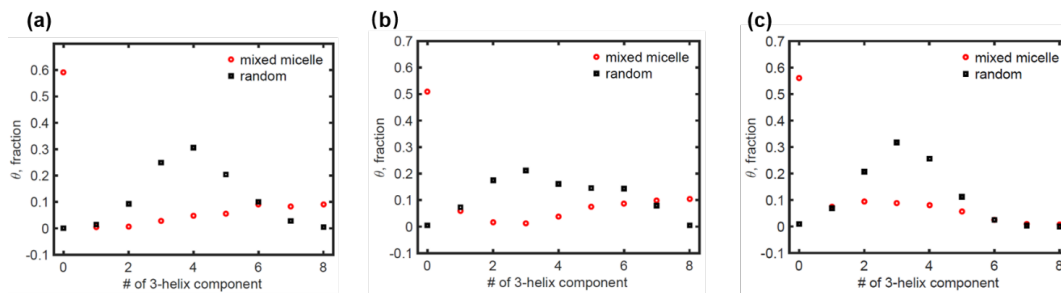


Figure 6.5 Phase separation and fragmentation measurements (red) compared to well mixed theoretical micelles (black) for three sample micelles (a-c). Panels (a-c) show θ_i , the number fraction of 8-bead fragmentation as a function of the number of 3-helix component in the 8 beads. The aggregation number of the sample micelles are 50, 56 and 57, with 3helix:4helix ratio 6:8, 8:8 and 7:8 respectively. The calculated sum of squared error (SSR) are high as 0.504, 0.438 and 0.492, which are anticipated for phase separated mixed micelles.

are used to quantify micro-phase separation, where comparison with a binomial (random) model and subsequent calculation of the sum-of-squares error provides a metric for phase separation. The same analysis can be done on the simulated systems to quantify microphase separation.

From the analysis of the trajectories, we find that the 3-helix subunits tend to assemble into a hemisphere of the mixture micelle, while 4-helix subunits assemble into the other hemisphere of the mixture micelle. The phase separation behavior shown here is more clear than what were reported in the previous copolymer self-assembly phase separation behaviors [164, 165], because the assembled subunits in our system have relatively large subunit volume. To differentiate the effects of core and shell, we first calculate the radius of gyration and end to end length of PEG in free solution, on isolated 3-helix bundle, in 3HM and in 4HM as in Table 6.2. The PEG chains have very similar behavior in 3HM and 4HM, which excludes the possibility that PEG can be the driving force of phase separation. Combined with the aforementioned analysis on conformational behaviors of alkyl chains, we can conclude that the alkyl chains from different components phase

	R_g Radial (Å)	R_g Tangential (Å)	R_g Total (Å)	R_{ee} (Å)
<i>Free PEG</i>	8.4±3.4	13.0±3.5	14.8±2.9	37.3±14.8
<i>PEG in 3-helix single bundle</i>	9.5±2.8	11.3±2.3	15.2±1.7	32.3±8.0
<i>In micelle</i>	3HM	9.6±0.8	13.5±0.8	17.0±0.6
	4HM	9.0±0.6	13.8±0.6	17.2±0.5

Table 6.2 Average conformational size of PEG polymer chains, including radius of gyration R_g , R_g in the radial direction (along the helix bundle), R_g in the tangential direction (vertical to the helix bundle), R_g in total and end-to-end distance R_{ee} in CG DPD simulations. The results are given by the present DPD CG simulations for PEG in 3HM, 4HM and 3&4 mixture micelles, and PEG on the isolated triple helix bundle and free polymer chains in water with standard deviations included. All the data presented here studied the same PEG chains with molecular weight 2000 Da in DPD simulations.

separate in the cores during micelle formation process and thus lead to the phase separation in the whole micelle. More specifically, due to the favorable interaction between alkyl beads, the alkyl chains prefer to assemble with other alkyl chains which have similar conformational distribution and length. As such, subunits from the same components assemble quickly into clusters. It should be noted that in Figure 6.5 (a)(b)(c), the fractions of all 4-helix component fragmentations are dominant, which indicates that the rapid self-assembly process of 4-helix components leads to the phase separation in mixed micelles, while the 3-helix components fill up the rest of the space. In the micelle fusion process, small micelles with phase separation behavior merge into a larger cluster with the phase separation behavior preserved, as shown in Figure 6.6. We can also conclude from the visualization of the simulation trajectories that fusing with other neighboring micelles is the dominant route to increase the size of individual micelles. Subunit migration is observed during the micelle fusing process as shown in Figure 6.6. Since some

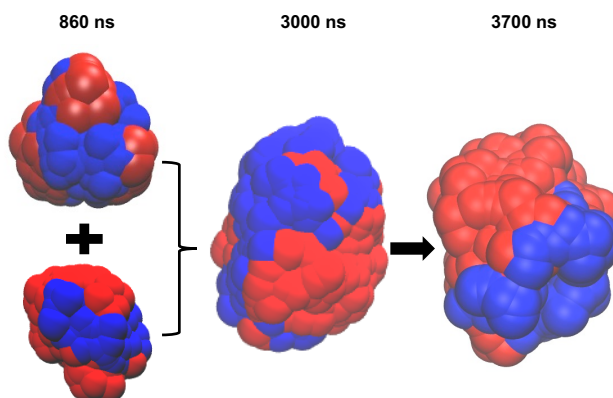


Figure 6.6 Schematic figure of the micelle fusion process, with the initial configuration of the small micelles at 860 ns, and the merged micelle at 3000 ns and 3700 ns. This figure shows the migration of coiled-coils into nanodomains within the mixed micelle. Only alkyl chains are shown in this figure for simplicity, with 4-helix components in red and 3-helix components in blue.

subunits may not find other subunits with the same oligomeric state nearby due to steric hindrance, some flaws and imperfect phase separation in large micelles can be seen.

6.4 Micelle Shape and Stability Investigations

Next, we present more details about the geometric characteristics of sample micelles from the DPD CG simulations as shown in Table 6.3 below to further investigate micelle size and hydration rate, as a step towards prospecting these nanocarriers for drug delivery applications. We can conclude from this table that, under the circumstances that each micelle has the similar number of subunits, 3HM, 4HM and 3&4 mixture micelles have comparable micelle sizes and core sizes. The 4HM has the greatest vacancy in the core and largest water content in the micelle, due to stretched alkyl structure, suggesting some packing frustration that may arise due to stronger driving forces and faster kinetics. Meanwhile, 3&4 mixture micelles have a larger

	3HM	4HM	34mix
AG number	45	60	50
Alkyl core radius (nm)	3.2	3.7	3.2
Vacancy in core (nm^3)	80.7	132.0	85.3
Micelle radius (nm)	7.0	7.7	7.4
Water content in micelle	4.2×10^3	5.3×10^3	4.5×10^3
SASA(nm^2)	18.0 ± 6.0	31.8 ± 6.8	24.1 ± 6.4

Table 6.3 Aggregation number, alkyl core radius, vacant volume in micelle core, water beads permeability and micelle SASA in comparison of 3HM, 4HM and 3&4 mixture micelles. The results are given by sample micelles in the present DPD CG simulations including all the three helix components. The water content in micelle is defined as the number of water beads inside the sample micelle (the micelle boundary here is defined as a PEG weight fraction at 10%).

vacant volume in the core than 3HM with the same alkyl core size, which may offer advantages for serving as a drug carrier. A possible explanation to this phenomenon can be that the phase separation in 3&4 mixture micelles leads to a more compact geometry with better packing. More specifically, subunits from different components separate and have different conformation distributions. This difference in distribution enlarges the vacant volume in core. As for the degree of hydration, both SASA and number of water beads permeating the micelle indicate that the 3&4 mixture micelle has a median degree of hydration in all the three cases, while 4HM has the highest.

The orientation of the helix bundle controls the orientation of ligands conjugated to the helix end, which determines the nanoparticle surface chemistry and the availability of ligand binding sites. Characterization of the ligand availability on the surface gain additional insights into the micelle shape, which we obtain by studying the helix orientation in micelles and the principal moments of inertia [166] [167]. The average ratios of the largest to smallest principal moments of inertia (I_{max}/I_{min}) over the last 150 ns of simulations for 3HM, 4HM and 3&4 mixture micelle are 1.31 ± 0.07 , 1.47 ± 0.07 and 1.16 ± 0.05 respectively, with eccentricity ($\eta = 1 - \frac{I_{min}}{I_{avg}}$) 0.13 ± 0.03 , 0.21 ± 0.03 , 0.08 ± 0.03 respectively. We also analyze the micelles, we find the orientation for helix bundle in 3HM to be $\varphi_{3HM-pure} = 19.4^\circ$; while in 4HM, $\varphi_{4HM-pure} = 25.5^\circ$. As for 3&4 mixtures, we calculate helix bundle orientation with regards to micelle radial direction to gain further insights into the micelle sphericity. From the sample mixture micelle $\varphi_{3HM-mix} = 16.3^\circ$, $\varphi_{4HM-mix} = 18.8^\circ$, $\varphi_{avg-mix} = 17.4^\circ$. The higher helix disorientation seen in 4HM is caused by a minor angle deviation in the 4-helix bundle structure.

A better helix bundle orientation indicates a more spherical micelle shape, corresponding well with the aforementioned orientation analyses. An explanation for this phenomenon may be the more efficient packing of the micelle core due to the mixing of alkyl chains from different components, which resolves packing frustration by allowing irregular subunit shapes to fill up the free volume more effectively. In a recent study on the shape effect of PEGylated nanoparticles on cellular uptake, Ying Li et al. reported that spherical nanoparticles encounter minimal internalization energy changes and thus should be most efficient as drug carriers. [133] Based on this observation, we suggest that the higher sphericity of the 3&4 mixture micelle may make it a better nanocarrier for drug delivery applications.

In order to quantify the interaction energy for alkyl chains beads in different components, we take the soft repulsive potential between two particles as $U^{rep}(r_{nm}) =$

$$\begin{cases} \frac{1}{2} a_{ij} (1 - r_{nm})^2 & \text{for } 0 \leq r_{nm} < r_c \\ 0 & \text{for } r_{nm} \geq r_c \end{cases},$$

where r_{nm} is the distance between bead n and m, and a_{ij}

is the repulsive parameter between bead type i and j. [168] First, the pair correlation functions

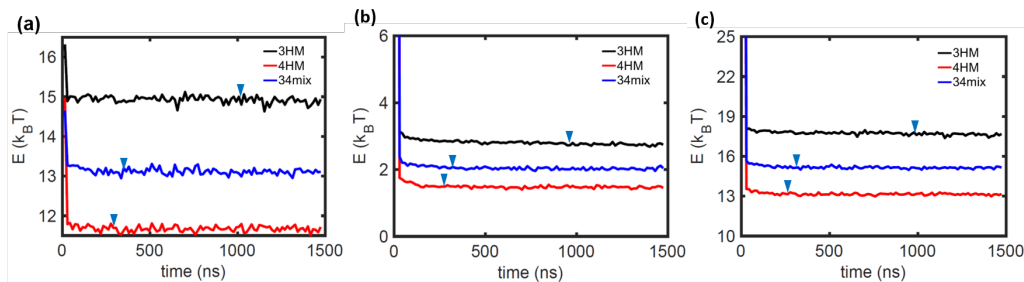


Figure 6.7 Average interaction energy between alkyl beads and (a) alkyl beads, (b) other beads, including the peptide, PEG and water, (c) all beads as a function of simulation time. This energy function compares pure 3-helix micelle (black), pure 4-helix micelle (red) and 3&4 mixture micelles (blue). The blue triangles indicate the convergence time for the two systems, at 300 ns for 3HM, 1000 ns for 4HM, and 330 ns for 3&4 mixture micelles. The results are given by DPD CG simulations including 3HM, 4HM and mixture micelles.

between alkyl beads and all types of beads are calculated, and when implemented into the repulsive potential above, we can come up with the interaction energy for alkyl beads. Given the repulsive nature of the potential, lower numerical values of the interaction energy indicate more favorable interactions. To compare different systems, we plot the alkyl interaction with alkyl, alkyl interaction with all other types of beads (including peptide, PEG and water), and finally alkyl interaction with all the beads as a function of time in Figure 6.7 Comparing alkyl to alkyl interactions in 3HM and 4HM in Figure 6.7 (a), we see that alkyl beads have more favorable interactions in 4HM. This confirms our previous conclusion that alkyl beads in 4HM have a larger driving force in micelle formation. In Figure 6.7 (b), we see the same trend for alkyl beads and peptide, PEG and water interaction, that alkyl beads have less interaction energy to other repulsive beads. This again supports our previous conclusion on micelle driving forces and

	3HM	4HM	mixture			3-helix single	4-helix single
			Ratio=3:4	Ratio=7:5	Ratio=11:5		
$U_{alkyl} (k_B T)$	14.91±0.01	11.67±0.04	12.93	13.38	13.62	15.99	13.74
$U_{others} (k_B T)$	2.63±0.02	1.28±0.02	1.74	1.93	2.08	2.74	3.23
$U_{all} (k_B T)$	17.54±0.03	12.95±0.02	14.66	15.31	15.70	18.73	16.97
$\Delta F (k_B T)$	-1.17±0.03	-4.02±0.02	-2.94	-2.56	-2.37		

Table 6.4 Average interaction energy of alkyl beads to alkyl beads, between other repulsive beads, and among all beads. These average interaction energies are computed for sample 3HM, 4HM and mixture micelles; and for alkyl bead interaction energy in 3-helix and 4-helix conjugates isolated in water solution. The free energy of 3HM, 4HM, and mixture micelle formation is also calculated as the energy in the micelle minus the energy in an isolated single helix bundle. The 3HM and 4HM results are given by the average and standard deviation values of 3 micelle samples with different sizes, and mixture micelles results include 3 different sample micelles with an increasing 3-helix component:4-helix component ratio. Given that DPD naturally has a repulsive interaction potential, larger interaction energy values here indicate less favorable interaction.

indicates that alkyl chains have a more extended conformation in 4HM relative to 3HM. Furthermore, we see that the alkyl energy declines continuously until convergence in Figure 6.7 (b)(c), which indicates that the energy decreases with self-assembly events that lead to micelle formation. In order to quantify and compare the free energy for micelle formation in 3HM, 4HM and mixture micelles, we tabulate the energy terms of sample micelles in Table 6.4. All the three energy terms for alkyl beads interaction energy in sample micelles agree well with the results in Figure 6.7. Moreover, we see that the free energy of 4HM formation is the largest in the three cases, while the 3HM has the least favorable free energy and mixture micelles have free energy in between. Meanwhile, increasing the ratio of 3-helix component in mixture micelles lowers the free energy value. These indicate that 4-helix conjugates have a large free energy in micelle formation, and thus lead to a faster micelle formation process, and a more stable micelle. Additionally, this energy difference also enables the phase separation behavior seen in simulations and experiments [158].

Chapter 7 Conclusions

Coiled coils are among the most extensively studied protein motif because of their structural simplicity and regularity. Recently, many studies have found improvement in helix stability by covalently cross-linking side-chain residues with polymer chains. Meanwhile, molecular dynamics is a computational tool that allows us to build and simulate systems with high levels of structural and chemical complexity, allowing us to explore the physical and thermomechanical behavior at small time and length scales, which makes it suitable for our study.

First, we presented coarse-grained simulations of a trimeric coiled coil conjugated with polymer chains at either its side or its end to provide insights into the effect of conjugation site on the stability and assembly mechanisms of peptide-polymer conjugates. Our annealing simulation studies on the thermal stability of coiled coils indicate insignificant difference between the melting temperature of pure coiled coils and that of coiled coils conjugated with polymer. Additionally, the alpha-helical secondary structure of helical units is completely preserved upon polymer conjugation, even indicating an increase in helicity. The tertiary structure of the trimers is also more or less retained in our simulations. These observations imply that the structural and thermal stability of alpha-helices are not perturbed by means of side polymer conjugation. As for self-assembly mechanisms, the steric occlusion of side-conjugated chains around the protein hinders the coiled coil units from getting too close to each other, leading to formation of clusters with small aggregation numbers (close to three). On the other hand, in the absence of polymer chains attached, clusters with large aggregation numbers are observed for pure coiled coils, which occur due to the absence of specific sequence-based

interactions in the CG model of peptide. The average cluster aggregation number for the end-conjugated coiled coils lies in-between the two aforementioned cases. Additionally, our MetaD simulations on disassembly of a single helical unit from the three-helix bundle show that the unzipping energy is the highest for coiled coils without polymer and the lowest for coiled coils with side-conjugated polymer, supporting the results of self-assembly simulations where pure coiled coils show the highest tendency to aggregate. These results indicate that polymer conjugation slows the rate of aggregation and thus it can be utilized as an efficient design technique to control protein self-assembly in different environments.

Next, we presented both all-atomistic and coarse-grained simulations of a three-helix coiled coil conjugated with three PEG chains of various lengths per helical strand to provide insights into the effect of conjugation density on the stability of coiled coil and conformations of PEG chains. For the PEG densities studied, the secondary structure of the helices and the tertiary structure of the coiled coil are retained. The PEG radius of gyration for three grafting sites per helix are similar to those of a single side-conjugated chain, implying that the excluded volume repulsion of the chains is not strong and thus the three chains do not feel the presence of each other. This is in agreement with the density profile of PEG chains with a parabolic curvature, showing that the chains form a mushroom-like shell around the coiled coil, whose size increases with an increase in PEG molecular weight. Then we analyze the values of PEG radius of gyration for longer chain lengths in the coarse-grained model together with scaling theory, and come to the conclusion that for surfaces with high curvature like coiled coils, we need much larger molecular weights to reach the brush regime.

PEG conjugations can be utilized as an efficient methodology for nanocarriers. Motivated by the desire to design polymer-peptide conjugate micelles with tunable size and shape for drug delivery, we first presented analyses based on a DPD CGMD simulation methodology and revealed important insights into the conformation and interfacial interactions of PEG chains in these systems. The main conclusions of this work can be summarized as follows. First, we find that the competition among the entropic penalty of PEG chain confinement and the cohesive interactions between adjacent chains dictates the kinetic stability of amphiphilic molecules. More specifically, polymer conjugation site and molecular weight influence both the entropic penalty and enthalpic cohesion, and thus lead to micelles with tunable sizes and stabilities. Among all the conjugation sites, P14 (middle) has the highest cohesive interaction due to favorable cohesion among PEG chains. Micelles with the P28 conjugation site show PEG far from the core, which decreases their enthalpic interaction density. P7 (closest to the core) is characterized by an entropic penalty effect that diminishes the advantage of PEG cohesive interaction, causing the formation of smaller micelles. Further, we predict possible micelle shapes for varied PEG molecular weights and conjugation sites, and also verified the entropic and enthalpic mechanisms. The recommendations of this project should prove useful for the design of functional micelles, using PEG conjugation site and molecular weight as potential design parameters. The current toolset of DPD simulations, as well as micelle models with tunable shapes, can also be extended to study transport through biological barriers.

The individual alkyl, peptide and PEG components allow for tunable micelle kinetic stability, since we have studied micelle sizes and shapes in different PEG conjugation sites and molecular weights, our next research focused on peptides. In order to further design mixed micelles with

multivalent ligand cluster sizes, we show how coiled coil-alkyl amphiphiles side-conjugated with a PEG chain exhibit variation in micelle formation kinetics and morphology due to the differences in their coiled-coil oligomeric states. We demonstrated that the alkyl chains in different confinement states lead to different micelle stability properties. In mixed micelles, 3-helix and 4-helix components self-associate into nanodomains to improve alkyl chain packing. Characterization of the ligand orientation, micelle hydrophobicity and drug carrier capacity in different micelle cases revealed advantages of using mixture micelles. Additionally, the 4HM displays stronger interaction energy and higher stability than 3HM, further confirmed by the enthalpy of alkyl chains, which appears to be the driving force for phase separation in mixed micelles. These analyses should provide useful guidance for the design of nanophase-separated micelles for multivalent ligand conjugation.

Based on these PEG conjugation results, simulation-based investigation of coiled coil stability under higher conjugation densities is an interesting research outlook, and our next step is to expand upon the current model to build much longer chains with high molecular weights. In this way, we can investigate if polymers can approach the brush regime and have a different effect on the protein's helical and coiled-coil structure. Considering the limitations of the GO-like model and the MARTINI model, a new coarse-grained model with both secondary and tertiary structure captured should be a practical tool.

These simulation results on micelles contribute to the design of PEG-peptide-alkyl conjugates forming micelles with tunable sizes, shapes, and multivalent ligand conjugations. As our next step in studying micelles as nanocarriers, we simulated 3HM in shear flow to investigate micelle stability in circulation; we also conducted simulations on single 3HM and its interactions

with lipid membrane to investigate the micelles endocytosis process using the same CG DPD tools. The micelles are stable in shear flow while we observe PEG chains tangentially confined to helix bundle radial direction. However, the coarse-grained peptide model is rigid rod, which cannot present peptides helicity changes in shear flow. Meanwhile, the CG nature of water molecules sacrifice degree of freedom and hydrogen bond integrations between water and micelles. Improving the accuracy of these models would be an area that may be worthy of further study. As for the micelle endocytosis studies, building DPD models on lipid bilayer as simplified cell membranes and examining interactions with different size micelles could be an area worthy of investigation. Our preliminary results indicate that it may be challenging to accurately capture endocytosis process with these simplified models. Considering the limitations of the DPD model, a new model with peptides secondary, tertiary structures and water hydrogen bonding captured should be a practical tool for micelle in shear flow studies. As for the micelle endocytosis study, DPD models would need to be tuned based on more experimental data to better present the micelle and lipid bilayer interactions. The scope of this thesis was limited to examining the basic aspects of the self-assembly mechanisms of helix-PEG-alkyl conjugate systems. The methods presented should help carry out more sophisticated calculations that may examine the interactions of these micellar systems with physiologically relevant environments.

References

1. Israelachvili, J.N., *Intermolecular and Surface Forces Preface to the Third Edition*. Intermolecular and Surface Forces, 3rd Edition, 2011: p. Xvii-+.
2. Groot, R.D. and K.L. Rabone, *Mesoscopic simulation of cell membrane damage, morphology change and rupture by nonionic surfactants*. Biophysical Journal, 2001. **81**(2): p. 725-736.
3. Dong, H., et al., *3-helix micelles stabilized by polymer springs*. Journal of the American Chemical Society, 2012. **134**: p. 11807-11814.
4. Shu, J.Y., R. Lund, and T. Xu, *Solution structural characterization of coiled-coil peptide-polymer side-conjugates*. Biomacromolecules, 2012. **13**(6): p. 1945-1955.
5. Lupas, A., *Coiled coils: new structures and new functions*. Trends in biochemical sciences, 1996. **21**(10): p. 375-382.
6. Lupas, A.N. and M. Gruber, *The Structure of α -Helical Coiled Coils*. Advances in protein chemistry, 2005. **70**: p. 37-38.
7. Bertaud, J., Z. Qin, and M.J. Buehler, *Atomistically Informed Mesoscale Model of Alpha-Helical Protein Domains*. International Journal for Multiscale Computational Engineering, 2009. **7**(3): p. 237-250.
8. Jing, P., et al., *Self-assembling peptide-polymer hydrogels designed from the coiled coil region of fibrin*. Biomacromolecules, 2008. **9**(9): p. 2438-2446.
9. Yu, Y.B., *Coiled-coils: stability, specificity, and drug delivery potential*. Advanced drug delivery reviews, 2002. **54**(8): p. 1113-1129.
10. Jain, A. and H.S. Ashbaugh, *Helix Stabilization of Poly(ethylene glycol)-Peptide Conjugates*. Biomacromolecules, 2011. **12**(7): p. 2729-2734.
11. Andrews, M.J.I. and A.B. Tabor, *Forming stable helical peptides using natural and artificial amino acids*. Tetrahedron, 1999. **55**(40): p. 11711-11743.
12. Austin, R.E., et al., *Template for stabilization of a peptide alpha-helix: Synthesis and evaluation of conformational effects by circular dichroism and NMR*. Journal of the American Chemical Society, 1997. **119**(28): p. 6461-6472.
13. Chakrabarty, A., A.J. Doig, and R.L. Baldwin, *Helix Capping Propensities in Peptides Parallel Those in Proteins*. Proceedings of the National Academy of Sciences of the United States of America, 1993. **90**(23): p. 11332-11336.
14. Xu, C.Y. and J. Kopecek, *Genetically engineered block copolymers: Influence of the length and structure of the coiled-coil blocks on hydrogel self-assembly*. Pharmaceutical Research, 2008. **25**(3): p. 674-682.
15. Tang, Y., et al., *Fluorinated coiled-coil proteins prepared in vivo display enhanced thermal and chemical stability*. Angewandte Chemie-International Edition, 2001. **40**(8): p. 1494-1496.
16. Tang, Y., et al., *Stabilization of coiled-coil peptide domains by introduction of trifluoroleucine*. Biochemistry, 2001. **40**(9): p. 2790-2796.
17. Blackwell, H.E. and R.H. Grubbs, *Highly efficient synthesis of covalently cross-linked*

- peptide helices by ring-closing metathesis*. *Angewandte Chemie-International Edition*, 1998. **37**(23): p. 3281-3284.
18. Schafmeister, C.E., J. Po, and G.L. Verdine, *An all-hydrocarbon cross-linking system for enhancing the helicity and metabolic stability of peptides*. *Journal of the American Chemical Society*, 2000. **122**(24): p. 5891-5892.
 19. Kutchukian, P.S., et al., *All-Atom Model for Stabilization of alpha-Helical Structure in Peptides by Hydrocarbon Staples*. *Journal of the American Chemical Society*, 2009. **131**(13): p. 4622-4627.
 20. Zhou, N.E., C.M. Kay, and R.S. Hodges, *The Role of Interhelical Ionic Interactions in Controlling Protein-Folding and Stability - De-Novo Designed Synthetic 2-Stranded Alpha-Helical Coiled-Coils*. *Journal of Molecular Biology*, 1994. **237**(4): p. 500-512.
 21. Houston, M.E., et al., *Lactam bridge stabilization of alpha-helices: The role of hydrophobicity in controlling dimeric versus monomeric alpha-helices*. *Biochemistry*, 1996. **35**(31): p. 10041-10050.
 22. Taylor, J.W., *The synthesis and study of side-chain lactam-bridged peptides*. *Biopolymers*, 2002. **66**(1): p. 49-75.
 23. Szleifer, I., *Statistical thermodynamics of polymers near surfaces*. *Current Opinion in Colloid & Interface Science*, 1996. **1**(3): p. 416-423.
 24. Shu, J.Y., et al., *New design of helix bundle peptide-polymer conjugates*. *Biomacromolecules*, 2008. **9**(8): p. 2111-2117.
 25. Hamed, E., T. Xu, and S. Keten, *Poly(ethylene glycol) Conjugation Stabilizes the Secondary Structure of alpha-Helices by Reducing Peptide Solvent Accessible Surface Area*. *Biomacromolecules*, 2013. **14**(11): p. 4053-4060.
 26. Lund, R., J. Shu, and T. Xu, *A Small-Angle X-ray Scattering Study of alpha-helical Bundle-Forming Peptide-Polymer Conjugates in Solution: Chain Conformations*. *Macromolecules*, 2013. **46**(4): p. 1625-1632.
 27. Dube, N., et al., *Evaluation of Doxorubicin-Loaded 3-Helix Micelles as Nanocarriers*. *Biomacromolecules*, 2013. **14**(10): p. 3697-3705.
 28. Pechar, M., et al., *Associative diblock copolymers of poly (ethylene glycol) and coiled - coil peptides*. *Macromolecular Bioscience*, 2002. **2**(5): p. 199-206.
 29. Kuhlman, B., et al., *Design of a novel globular protein fold with atomic-level accuracy*. *Science*, 2003. **302**(5649): p. 1364-1368.
 30. Mitra, P., D. Shultis, and Y. Zhang, *EvoDesign: de novo protein design based on structural and evolutionary profiles*. *Nucleic Acids Research*, 2013. **41**(W1): p. W273-W280.
 31. Berwick, M.R., et al., *De Novo Design of Ln (III) Coiled Coils for Imaging Applications*. *Journal of the American Chemical Society*, 2014. **136**(4): p. 1166-1169.
 32. Shu, J.Y., et al., *New Design of Helix Bundle Peptide-Polymer Conjugates*. *Biomacromolecules*, 2008. **9**(8): p. 2111-2117.
 33. Dong, H., et al., *Long-Circulating 15 nm Micelles Based on Amphiphilic 3-Helix Peptide-PEG Conjugates*. *Acs Nano*, 2012. **6**(6): p. 5320-5329.
 34. Andrew MacKay, J., et al., *Self-assembling chimeric polypeptide-doxorubicin conjugate nanoparticles that abolish tumours after a single injection*. *Nature Materials*, 2009. **8**(12):

- p. 993-999.
35. Hubbell, J.A., S.N. Thomas, and M.A. Swartz, *Materials engineering for immunomodulation*. Nature, 2009. **462**(7272): p. 449-460.
 36. Kaida, S., et al., *Visible Drug Delivery by Supramolecular Nanocarriers Directing to Single-Platformed Diagnosis and Therapy of Pancreatic Tumor Model*. Cancer Research, 2010. **70**(18): p. 7031-7041.
 37. Popović, Z., et al., *A Nanoparticle Size Series for In Vivo Fluorescence Imaging*. Angewandte Chemie International Edition, 2010. **49**(46): p. 8649-8652.
 38. Greish, K., *Enhanced permeability and retention (EPR) effect for anticancer nanomedicine drug targeting*. Cancer Nanotechnology: Methods and Protocols, 2010: p. 25-37.
 39. Iyer, A.K., et al., *Exploiting the enhanced permeability and retention effect for tumor targeting*. Drug discovery today, 2006. **11**(17): p. 812-818.
 40. Maeda, H., *Tumor-selective delivery of macromolecular drugs via the EPR effect: background and future prospects*. Bioconjugate chemistry, 2010. **21**(5): p. 797-802.
 41. Maeda, H., H. Nakamura, and J. Fang, *The EPR effect for macromolecular drug delivery to solid tumors: Improvement of tumor uptake, lowering of systemic toxicity, and distinct tumor imaging in vivo*. Advanced drug delivery reviews, 2013. **65**(1): p. 71-79.
 42. Torchilin, V., *Tumor delivery of macromolecular drugs based on the EPR effect*. Advanced drug delivery reviews, 2011. **63**(3): p. 131-135.
 43. Dube, N., et al., *Effect of Alkyl Length of Peptide-Polymer Amphiphile on Cargo Encapsulation Stability and Pharmacokinetics of 3-Helix Micelles*. Biomacromolecules, 2014. **15**(8): p. 2963-2970.
 44. Dong, H., R. Lund, and T. Xu, *Micelle Stabilization via Entropic Repulsion: Balance of Force Directionality and Geometric Packing of Subunit*. Biomacromolecules, 2015. **16**(3): p. 743-747.
 45. Dong, H., et al., *Long-Circulating 15 nm Micelles Based on Amphiphilic 3-Helix Peptide-PEG Conjugates*. ACS Nano, 2012. **6**(6): p. 5320-5329.
 46. Seo, J.W., et al., *Self-assembled 20-nm Cu-64-micelles enhance accumulation in rat glioblastoma*. Journal of Controlled Release, 2015. **220**: p. 51-60.
 47. Alder, B. and T. Wainwright, *Phase transition for a hard sphere system*. The Journal of Chemical Physics, 1957. **27**(5): p. 1208-1209.
 48. Liu, W.K., et al., *An introduction to computational nanomechanics and materials*. Computer Methods in Applied Mechanics and Engineering, 2004. **193**(17): p. 1529-1578.
 49. Buehler, M.J. and S. Keten, *Colloquium: Failure of molecules, bones, and the Earth itself*. Reviews of Modern Physics, 2010. **82**(2): p. 1459-1487.
 50. MacKerell Jr, A.D., *Atomistic models and force fields*. Computational Biochemistry and Biophysics, 2001: p. 7-38.
 51. Daw, M.S. and M.I. Baskes, *Embedded-atom method: Derivation and application to impurities, surfaces, and other defects in metals*. Physical Review B, 1984. **29**(12): p. 6443.
 52. Jorgensen, W.L., D.S. Maxwell, and J. Tirado-Rives, *Development and testing of the OPLS all-atom force field on conformational energetics and properties of organic liquids*.

- Journal of the American Chemical Society, 1996. **118**(45): p. 11225-11236.
53. Pearlman, D.A., et al., *AMBER, a package of computer programs for applying molecular mechanics, normal mode analysis, molecular dynamics and free energy calculations to simulate the structural and energetic properties of molecules*. Computer Physics Communications, 1995. **91**(1): p. 1-41.
 54. Oostenbrink, C., et al., *A biomolecular force field based on the free enthalpy of hydration and solvation: The GROMOS force -field parameter sets 53A5 and 53A6*. Journal of computational chemistry, 2004. **25**(13): p. 1656-1676.
 55. Nelson, M.T., et al., *NAMD: A parallel, object oriented molecular dynamics program*. International Journal of Supercomputer Applications and High Performance Computing, 1996. **10**(4): p. 251-268.
 56. Barducci, A., M. Bonomi, and M. Parrinello, *Metadynamics*. Wiley Interdisciplinary Reviews-Computational Molecular Science, 2011. **1**(5): p. 826-843.
 57. Laio, A. and M. Parrinello, *Escaping free-energy minima*. Proceedings of the National Academy of Sciences of the United States of America, 2002. **99**(20): p. 12562-12566.
 58. de Souza, O.N. and R.L. Ornstein, *Effect of periodic box size on aqueous molecular dynamics simulation of a DNA dodecamer with particle-mesh Ewald method*. Biophysical journal, 1997. **72**(6): p. 2395-2397.
 59. Gibbs, J.W., *Elementary principles in statistical mechanics: developed with especial reference to the rational foundation of thermodynamics*. 2010: Cambridge University Press.
 60. Karanicolas, J. and C.L. Brooks, *The origins of asymmetry in the folding transition states of protein L and protein G*. Protein Science, 2002. **11**: p. 2351-2361.
 61. Ueda, Y., H. Taketomi, and N. Go, *Studies on protein folding, unfolding and fluctuations by computer simulation. A three-dimensional lattice model of lysozyme*. Biopolymers, 1978. **17**: p. 1531-1548.
 62. Marrink, S.J., A.H. de Vries, and A.E. Mark, *Coarse grained model for semiquantitative lipid simulations*. Journal of Physical Chemistry B, 2004. **108**(2): p. 750-760.
 63. Marrink, S.J., et al., *The MARTINI force field: coarse grained model for biomolecular simulations*. The Journal of Physical Chemistry B, 2007. **111**(27): p. 7812-7824.
 64. Seo, M., et al., *Improving Internal Peptide Dynamics in the Coarse-Grained MARTINI Model: Toward Large-Scale Simulations of Amyloid- and Elastin-like Peptides*. Journal of Chemical Theory and Computation, 2012. **8**(5): p. 1774-1785.
 65. MacKerell Jr, A.D., et al., *All-atom empirical potential for molecular modeling and dynamics studies of proteins*. The journal of physical chemistry B, 1998. **102**(18): p. 3586-3616.
 66. Monticelli, L., et al., *The MARTINI coarse-grained force field: extension to proteins*. Journal of Chemical Theory and Computation, 2008. **4**(5): p. 819-834.
 67. Kranenburg, M. and B. Smit, *Phase behavior of model lipid bilayers*. J Phys Chem B, 2005. **109**(14): p. 6553-63.
 68. Venturoli, M., B. Smit, and M.M. Sperotto, *Simulation studies of protein-induced bilayer deformations, and lipid-induced protein tilting, on a mesoscopic model for lipid bilayers with embedded proteins*. Biophys J, 2005. **88**(3): p. 1778-98.

69. Jakobsen, A.F., O.G. Mouritsen, and G. Besold, *Artifacts in dynamical simulations of coarse-grained model lipid bilayers*. Journal of Chemical Physics, 2005. **122**(20).
70. Huang, J.H., Z.X. Fan, and Z.X. Ma, *Dissipative particle dynamics simulations on self-assembly of rod-coil-rod triblock copolymers in a rod-selective solvent*. J Chem Phys, 2013. **139**(6): p. 064905.
71. Li, Y., M. Kroger, and W.K. Liu, *Endocytosis of PEGylated nanoparticles accompanied by structural and free energy changes of the grafted polyethylene glycol*. Biomaterials, 2014. **35**(30): p. 8467-8478.
72. Rolfe, B.A., J. Chun, and Y.L. Joo, *Dynamics of micelle-nanoparticle systems undergoing shear: a coarse-grained molecular dynamics approach*. Soft Matter, 2013. **9**(43): p. 10294-10305.
73. Li, Y., et al., *Surface-structure-regulated penetration of nanoparticles across a cell membrane*. Nanoscale, 2012. **4**(12): p. 3768-3775.
74. Harkness, K.M., et al., *Nanoscale phase segregation of mixed thiolates on gold nanoparticles*. Angewandte Chemie International Edition, 2011. **50**(45): p. 10554-10559.
75. Merz, S.N., et al., *Theoretical and Experimental Investigation of Microphase Separation in Mixed Thiol Monolayers on Silver Nanoparticles*. ACS nano, 2016. **10**(11): p. 9871-9878.
76. Pechar, M., et al., *Associative diblock copolymers of poly(ethylene glycol) and coiled-coil peptides*. Macromolecular Bioscience, 2002. **2**(5): p. 199-206.
77. Petka, W.A., et al., *Reversible hydrogels from self-assembling artificial proteins*. Science, 1998. **281**(5375): p. 389-392.
78. Vandermeulen, G.W.M., et al., *PEG-based hybrid block copolymers containing alpha-helical coiled coil peptide sequences: Control of self-assembly and preliminary biological evaluation*. Macromolecules, 2005. **38**(3): p. 761-769.
79. Vandermeulen, G.W.M., C. Tziatzios, and H.A. Klok, *Reversible self-organization of poly(ethylene glycol)-based hybrid block copolymers mediated by a De Novo four-stranded alpha-helical coiled coil motif*. Macromolecules, 2003. **36**(11): p. 4107-4114.
80. Top, A., et al., *Controlling assembly of helical polypeptides via PEGylation strategies*. Soft Matter, 2011. **7**: p. 9758-9766.
81. Shu, J.Y., et al., *Amphiphilic peptide-polymer conjugates based on the coiled-coil helix bundle*. Biomacromolecules, 2010. **11**: p. 1443-1452.
82. Hamed, E., T. Xu, and S. Keten, *Poly(ethylene glycol) conjugation stabilizes the secondary structure of α -helices by reducing peptide solvent accessible surface area*. Biomacromolecules, 2013. **14**: p. 4053-4060.
83. Ogihara, N.L., et al., *The crystal structure of the designed trimeric coiled coil coil-V(a)L(d): Implications for engineering crystals and supramolecular assemblies*. Protein Science, 1997. **6**(1): p. 80-88.
84. Baker, D., *A surprising simplicity to protein folding*. Nature, 2000. **405**: p. 39-42.
85. Lee, H., et al., *A Coarse-Grained Model for Polyethylene Oxide and Polyethylene Glycol: Conformation and Hydrodynamics*. Journal of Physical Chemistry B, 2009. **113**(40): p. 13186-13194.

86. Lianos, P. and R. Zana, *Fluorescence Probe Studies of the Effect of Concentration on the State of Aggregation of Surfactants in Aqueous-Solution*. Journal of Colloid and Interface Science, 1981. **84**(1): p. 100-107.
87. Top, A., C.J. Roberts, and K.L. Kiick, *Conformational and aggregation properties of a PEGylated alanine-rich polypeptide*. Biomacromolecules, 2011. **12**(6): p. 2184-2192.
88. Rajan, R.S., et al., *Modulation of protein aggregation by polyethylene glycol conjugation: GCSF as a case study*. Protein Science, 2006. **15**(5): p. 1063-1075.
89. Bonomi, M., et al., *PLUMED: A portable plugin for free-energy calculations with molecular dynamics*. Computer Physics Communications, 2009. **180**(10): p. 1961-1972.
90. Hamed, E. and S. Keten, *Hierarchical cascades of instability govern the mechanics of coiled coils: Helix unfolding precedes coil unzipping*. Biophysical Journal, 2014. **In Press**.
91. Hsu, D., et al., *Systematic method for thermomechanically consistent coarse-graining: A universal model for methacrylate-based polymers*. Journal of Chemical Theory and Computation, 2014. **10**: p. 2514–2527.
92. Shu, J.Y., R. Lund, and T. Xu, *Solution Structural Characterization of Coiled-Coil Peptide-Polymer Side-Conjugates*. Biomacromolecules, 2012. **13**(6): p. 1945-1955.
93. Carignano, M. and I. Szleifer, *On the structure and pressure of tethered polymer layers in good solvent*. Macromolecules, 1995. **28**(9): p. 3197-3204.
94. Binder, K. and A. Milchev, *Polymer brushes on flat and curved surfaces: How computer simulations can help to test theories and to interpret experiments*. Journal of Polymer Science Part B: Polymer Physics, 2012. **50**(22): p. 1515-1555.
95. Dimitrov, D., A. Milchev, and K. Binder, *Polymer brushes in cylindrical pores: simulation versus scaling theory*. The Journal of chemical physics, 2006. **125**(3): p. 034905.
96. Kent, M., et al., *Tethered chains in good solvent conditions: an experimental study involving Langmuir diblock copolymer monolayers*. The Journal of chemical physics, 1995. **103**(6): p. 2320-2342.
97. Wu, T., et al., *A combinatorial approach to surface anchored polymers*. Journal of materials science, 2003. **38**(22): p. 4471-4477.
98. Milner, S.T., *Polymer Brushes*. Science, 1991. **251**(4996): p. 905-914.
99. Humphrey, W., A. Dalke, and K. Schulten, *VMD: visual molecular dynamics*. Journal of molecular graphics, 1996. **14**(1): p. 33-38.
100. Brooks, B.R., et al., *CHARMM: A program for macromolecular energy, minimization, and dynamics calculations*. Journal of computational chemistry, 1983. **4**(2): p. 187-217.
101. Hamed, E., D. Ma, and S. Keten, *Effect of polymer conjugation site on stability and self-assembly of coiled coils*. BioNanoScience, 2015. **5**(3): p. 140-149.
102. Carignano, M.A. and I. Szleifer, *Structural and Thermodynamic Properties of End-Grafted Polymers on Curved Surfaces*. Journal of Chemical Physics, 1995. **102**(21): p. 8662-8669.
103. Murat, M. and G.S. Grest, *Polymers end-grafted onto a cylindrical surface*. Macromolecules, 1991. **24**(3): p. 704-708.
104. Gong, K., B.D. Marshall, and W.G. Chapman, *Modeling lower critical solution*

- temperature behavior of associating polymer brushes with classical density functional theory.* Journal of Chemical Physics, 2013. **139**(9).
105. Dimitrov, D.I., et al., *Structure of polymer brushes in cylindrical tubes: A molecular dynamics simulation.* Macromolecular Theory and Simulations, 2006. **15**(7): p. 573-583.
 106. Maki-Ontto, R., et al., *"Hairy tubes": Mesoporous materials containing hollow self-organized cylinders with polymer brushes at the walls.* Advanced Materials, 2001. **13**(2): p. 117-121.
 107. Sevick, E.M., *Shear swelling of polymer brushes grafted onto convex and concave surfaces.* Macromolecules, 1996. **29**(21): p. 6952-6958.
 108. Hiergeist, C. and R. Lipowsky, *Elastic properties of polymer-decorated membranes.* Journal De Physique Ii, 1996. **6**(10): p. 1465-1481.
 109. Dan, N. and M. Tirrell, *Self-Assembly of Block-Copolymers with a Strongly Charged and a Hydrophobic Block in a Selective, Polar-Solvent - Micelles and Adsorbed Layers.* Macromolecules, 1993. **26**(16): p. 4310-4315.
 110. Zhulina, E.B. and F.A.M. Leermakers, *A self-consistent field analysis of the neurofilament brush with amino-acid resolution.* Biophysical Journal, 2007. **93**(5): p. 1421-1430.
 111. Alexander, S., *Polymer adsorption on small spheres. A scaling approach.* Journal de Physique, 1977. **38**(8): p. 977-981.
 112. de Gennes, P., *Conformations of polymers attached to an interface.* Macromolecules, 1980. **13**(5): p. 1069-1075.
 113. Wijmans, C., J. Scheutjens, and E. Zhulina, *Self-consistent field theories for polymer brushes: lattice calculations and an asymptotic analytical description.* Macromolecules, 1992. **25**(10): p. 2657-2665.
 114. Wijmans, C.M. and E.B. Zhulina, *Polymer brushes at curved surfaces.* Macromolecules, 1993. **26**: p. 7214-7224.
 115. Woo, S.Y. and H. Lee, *Molecular dynamics studies of PEGylated α -helical coiled coils and their self-assembled micelles.* Langmuir, 2014. **30**: p. 8848-8855.
 116. Ruiz, L. and S. Keten, *Directing the self-assembly of supra-biomolecular nanotubes using entropic forces.* Soft Matter, 2014. **10**: p. 851-861.
 117. Chung, H.J. and T.G. Park, *Self-assembled and nanostructured hydrogels for drug delivery and tissue engineering.* Nano Today, 2009. **4**(5): p. 429-437.
 118. Nasongkla, N., et al., *Multifunctional polymeric micelles as cancer-targeted, MRI-ultrasensitive drug delivery systems.* Nano letters, 2006. **6**(11): p. 2427-2430.
 119. Cabral, H., et al., *Accumulation of sub-100 nm polymeric micelles in poorly permeable tumours depends on size.* Nature nanotechnology, 2011. **6**(12): p. 815-823.
 120. Duncan, R., *The dawning era of polymer therapeutics.* Nature Reviews Drug Discovery, 2003. **2**(5): p. 347-360.
 121. Torchilin, V.P., *PEG-based micelles as carriers of contrast agents for different imaging modalities.* Advanced drug delivery reviews, 2002. **54**(2): p. 235-252.
 122. Dubertret, B., et al., *In vivo imaging of quantum dots encapsulated in phospholipid micelles.* Science, 2002. **298**(5599): p. 1759-1762.
 123. Joralemon, M.J., et al., *Shell Click-crosslinked (SCC) nanoparticles: A new methodology*

- for synthesis and orthogonal functionalization*. Journal of the American Chemical Society, 2005. **127**(48): p. 16892-16899.
124. Sarkar, A., et al., *Hydrodynamic interactions of deformable polymeric nanocarriers and the effect of crosslinking*. Soft Matter, 2015. **11**(29): p. 5955-69.
 125. Sun, X., et al., *An assessment of the effects of shell cross-linked nanoparticle size, core composition, and surface PEGylation on in vivo biodistribution*. Biomacromolecules, 2005. **6**(5): p. 2541-2554.
 126. Ferrer, M.C.C., et al., *Designing nanogel carriers for antibacterial applications*. Acta biomaterialia, 2014. **10**(5): p. 2105-2111.
 127. Zhang, Q., E.E. Remsen, and K.L. Wooley, *Shell cross-linked nanoparticles containing hydrolytically degradable, crystalline core domains*. Journal of the American Chemical Society, 2000. **122**(15): p. 3642-3651.
 128. Hamed, E., D. Ma, and S. Keten, *Multiple PEG Chains Attached onto the Surface of a Helix Bundle: Conformations and Implications*. ACS Biomaterials Science & Engineering, 2015. **1**(2): p. 79-84.
 129. DeBenedictis, E.P., E. Hamed, and S. Keten, *Mechanical Reinforcement of Proteins with Polymer Conjugation*. ACS nano, 2015.
 130. Fattal, D.R. and A. Ben-Shaul, *A molecular model for lipid-protein interaction in membranes: the role of hydrophobic mismatch*. Biophysical journal, 1993. **65**(5): p. 1795.
 131. Friesner, R.A., et al., *Extra precision glide: docking and scoring incorporating a model of hydrophobic enclosure for protein-ligand complexes*. Journal of medicinal chemistry, 2006. **49**(21): p. 6177-6196.
 132. Lee, H., et al., *A Coarse-Grained Model for Polyethylene Oxide and Polyethylene Glycol: Conformation and Hydrodynamics*. The Journal of Physical Chemistry B, 2009. **113**(40): p. 13186-13194.
 133. Li, Y., M. Kröger, and W.K. Liu, *Shape effect in cellular uptake of pegylated nanoparticles: comparison between sphere, rod, cube and disk*. Nanoscale, 2015. **7**(40): p. 16631-16646.
 134. Martinez, L., et al., *PACKMOL: A Package for Building Initial Configurations for Molecular Dynamics Simulations*. Journal of Computational Chemistry, 2009. **30**(13): p. 2157-2164.
 135. Minton, A.P., *Excluded Volume as a Determinant of Macromolecular Structure and Reactivity*. Biopolymers, 1981. **20**(10): p. 2093-2120.
 136. Li, K. and Q. Wang, *Multiple self-assembled nanostructures from an oligo (p-phenyleneethynylene) containing rod-coil-rod triblock copolymer*. Chemical communications, 2005(38): p. 4786-4788.
 137. Rubinstein, M. and R. Colby, *Polymers physics*. Vol. 767. 2003: Oxford Oxford, UK.
 138. Nagarajan, R. and E. Ruckenstein, *Theory of surfactant self-assembly: a predictive molecular thermodynamic approach*. Langmuir, 1991. **7**(12): p. 2934-2969.
 139. Elias, D.R., et al., *Effect of ligand density, receptor density, and nanoparticle size on cell targeting*. Nanomedicine: nanotechnology, biology and medicine, 2013. **9**(2): p. 194-201.
 140. Lee, C.C., et al., *Designing dendrimers for biological applications*. Nature biotechnology, 2005. **23**(12): p. 1517.

141. Tang, Z., et al., *Quantitative control of active targeting of nanocarriers to tumor cells through optimization of folate ligand density*. *Biomaterials*, 2014. **35**(27): p. 8015-8027.
142. Nicolas, J., et al., *Design, functionalization strategies and biomedical applications of targeted biodegradable/biocompatible polymer-based nanocarriers for drug delivery*. *Chemical Society Reviews*, 2013. **42**(3): p. 1147-1235.
143. Mammen, M., S.-K. Choi, and G.M. Whitesides, *Polyvalent interactions in biological systems: implications for design and use of multivalent ligands and inhibitors*. *Angewandte Chemie International Edition*, 1998. **37**(20): p. 2754-2794.
144. Rao, J., et al., *A trivalent system from vancomycin· d-Ala-d-Ala with higher affinity than avidin· biotin*. *Science*, 1998. **280**(5364): p. 708-711.
145. Saul, J.M., A.V. Annapragada, and R.V. Bellamkonda, *A dual-ligand approach for enhancing targeting selectivity of therapeutic nanocarriers*. *Journal of Controlled Release*, 2006. **114**(3): p. 277-287.
146. Ashley, C.E., et al., *The targeted delivery of multicomponent cargos to cancer cells via nanoporous particle-supported lipid bilayers*. *Nature materials*, 2011. **10**(5): p. 389.
147. Müllner, M. and A.H. Müller, *Cylindrical polymer brushes—Anisotropic building blocks, unimolecular templates and particulate nanocarriers*. *Polymer*, 2016. **98**: p. 389-401.
148. Ackerman, D.G. and G.W. Feigenson, *Multiscale modeling of four-component lipid mixtures: domain composition, size, alignment, and properties of the phase interface*. *The Journal of Physical Chemistry B*, 2015. **119**(11): p. 4240-4250.
149. Bacia, K., P. Schwille, and T. Kurzchalia, *Sterol structure determines the separation of phases and the curvature of the liquid-ordered phase in model membranes*. *Proceedings of the National Academy of Sciences of the United States of America*, 2005. **102**(9): p. 3272-3277.
150. Chiantia, S. and E. London, *Acyl chain length and saturation modulate interleaflet coupling in asymmetric bilayers: effects on dynamics and structural order*. *Biophysical journal*, 2012. **103**(11): p. 2311-2319.
151. Hammond, A., et al., *Crosslinking a lipid raft component triggers liquid ordered-liquid disordered phase separation in model plasma membranes*. *Proceedings of the National Academy of Sciences of the United States of America*, 2005. **102**(18): p. 6320-6325.
152. Parthasarathy, R., C.-h. Yu, and J.T. Groves, *Curvature-modulated phase separation in lipid bilayer membranes*. *Langmuir*, 2006. **22**(11): p. 5095-5099.
153. Shi, Q. and G.A. Voth, *Multi-scale modeling of phase separation in mixed lipid bilayers*. *Biophysical journal*, 2005. **89**(4): p. 2385-2394.
154. García-Sáez, A.J., S. Chiantia, and P. Schwille, *Effect of line tension on the lateral organization of lipid membranes*. *Journal of Biological Chemistry*, 2007. **282**(46): p. 33537-33544.
155. Heberle, F.A., et al., *Bilayer thickness mismatch controls domain size in model membranes*. *Journal of the American Chemical Society*, 2013. **135**(18): p. 6853-6859.
156. Ang, J., et al., *Internal Structure of 15 nm 3-Helix Micelle Revealed by Small-Angle Neutron Scattering and Coarse-Grained MD Simulation*. *Biomacromolecules*, 2016. **17**(10): p. 3262-3267.
157. Ma, D., et al., *Design of polymer conjugated 3-helix micelles as nanocarriers with*

- tunable shapes*. *Nanoscale*, 2016. **8**(46): p. 19334-19342.
158. Ang, J., et al., *Sub-20 nm Stable Micelles Based on a Mixture of Coiled-Coils: A Platform for Controlled Ligand Presentation*. *Biomacromolecules*, 2017. **18**(11): p. 3572-3580.
 159. Phillips, J.C., et al., *Scalable molecular dynamics with NAMD*. *Journal of computational chemistry*, 2005. **26**(16): p. 1781-1802.
 160. Jorgensen, W.L., et al., *Comparison of simple potential functions for simulating liquid water*. *The Journal of chemical physics*, 1983. **79**(2): p. 926-935.
 161. Plimpton, S., *Fast parallel algorithms for short-range molecular dynamics*. *Journal of computational physics*, 1995. **117**(1): p. 1-19.
 162. Li, Y., et al., *Graphene microsheets enter cells through spontaneous membrane penetration at edge asperities and corner sites*. *Proceedings of the National Academy of Sciences*, 2013. **110**(30): p. 12295-12300.
 163. Daoud, M. and J. Cotton, *Star shaped polymers: a model for the conformation and its concentration dependence*. *Journal de Physique*, 1982. **43**(3): p. 531-538.
 164. Illya, G., R. Lipowsky, and J. Shillcock, *Two-component membrane material properties and domain formation from dissipative particle dynamics*. *The Journal of chemical physics*, 2006. **125**(11): p. 114710.
 165. Laradji, M. and P.S. Kumar, *Domain growth, budding, and fission in phase-separating self-assembled fluid bilayers*. *The Journal of chemical physics*, 2005. **123**(22): p. 224902.
 166. Bruce, C.D., et al., *Molecular dynamics simulation of sodium dodecyl sulfate micelle in water: micellar structural characteristics and counterion distribution*. *The Journal of Physical Chemistry B*, 2002. **106**(15): p. 3788-3793.
 167. Salaniwal, S., et al., *Molecular simulation of a dichain surfactant/water/carbon dioxide system. I. Structural properties of aggregates*. *Langmuir*, 2001. **17**(5): p. 1773-1783.
 168. Wijmans, C., B. Smit, and R. Groot, *Phase behavior of monomeric mixtures and polymer solutions with soft interaction potentials*. *The Journal of Chemical Physics*, 2001. **114**(17): p. 7644-7654.

Vita**DAN MA****EDUCATION**

- PhD, Mechanical Engineering in Northwestern university, Evanston IL 2015-2018
 - ✓ Advisor: Professor Sinan Keten; GPA 3.9/4.0
 - ✓ Martin Outstanding Doctoral Fellowship, Northwestern University
 - ✓ Honorary Terminal year Fellow, Northwestern University
- Master, Mechanical Engineering in Northwestern university, Evanston IL 2013-2014
- Bachelor, Mechanical Engineering in Tsinghua University, Beijing 2009-2013
 - ✓ Scholarship for Academic Excellence, Tsinghua University
 - ✓ Exchange experience in Technical University of Denmark, straight A

TEACHING EXPERIENCE

- Teaching assistant for course MECH_ENG 233: Electronics Design
- Teaching assistant for course MECH_ENG 416: Computational Nanodynamics
- Teaching assistant for course MECH_ENG 418: Multi-Scale Modeling and Simulation in Fluid Dynamics

PROJECTS EXPERIENCE

Ab-initio Studies on Marine Mussel Adhesive Proteins**2017-present**

- Employed DFT (density functional theory) method to simulate iron ions with different oxidation states, Fe²⁺, Fe³⁺, forming two, tobias and tris complexes and investigated on the binding nature or the metal and catechol interactions
- Conducted metadynamics simulations with ab initio molecular dynamics to examine the cross-linking structure and energy landscapes
- Developed two beads coarse-grained model on mimic mussel protein polymers to explore their adhesion, self-healing and other mechanical characteristics

Yelp Data Challenge with Natural Language Processing**2018**

- Performed tokenization and TF-IDF to convert 348k user review data to vector space for NLP Study
- Built Naïve Bayes, Logistic Regression and Random Forest to predict the successfulness of a restaurant based on user reviews: performed PCA, cross-validation and grid-search for parameter tuning and model selection; achieved 85.67% accuracy score by logistic regression model on test data set
- Implemented K-means clustering to identify common user preferences and the best restaurant within each

group

- Built a restaurant recommender using item-item collaborative filtering based on user past ratings and visits

Lending Club Risk Adjusted Interest Rate Prediction **2017**

- Extracted 23 features from raw lending club loan data containing different types, such as categorial, numerical and time series data, imputed missing data using multivariate imputation by chained equation (MICE) algorithm
- Performed feature selection through exploratory analysis
- Fitted linear regression model with regularization to control for multicollinearity and built decision tree, random forest, boosting decision tree to predict interest rate for each loan
- Achieved 3.17 RMSE by boosting decision tree model on test data set

Peptides based Micelle as Nanocarrier **2015-2017**

- Built efficient model in C++ environment, and ran with high performance computing to studying micelle formation behavior of helical peptides based amphiphiles
- Discovered the intermolecular interaction among conjugated polymer chains. Opened pathways to micelle design of tunable shapes and sizes, with great potential as drug nanocarriers for brain cancer, Alzheimer's disease etc.

Molecular Dynamics Simulation based Peptide Polymer conjugation effect **2013-2015**

- Revealed the effect of conjugated polyethylene glycol polymer (PEG) chains on peptide self-assemble behavior by simulating the 3-helix peptides, with or without PEG chains conjugated on different positions
- Investigated the mechanism of PEGylated molecules self-assembly pattern
- Investigated the PEG chains conformations using molecular dynamics with multiple chains conjugated to peptides
- Generated stimuli-responsive switches that activate helix folding/unfolding

Analysis and Improvements of Spherical Rotors' Surface Quality **2013**

- Simulated polishing possibility of each of the points on the ball with predictive MATLAB model
- Revealed the influence of regular and random cycle sequence on rotors' surface, leading to a 38.7% more precise methodology of polishing

Sensor System Test Platform and Database Integration **2011-2012**

- Developed a test platform by using LABVIEW and MATLAB, integrated accelerometer and gyro sensor in the production chain

- Enhanced the accuracy of gyro sensor through validating the accelerometer test subsystem and overall database

PUBLICATIONS

- Dan Ma and Sinan Keten, "Stable Micelles Based on a Mixture of Coiled-coils: The Role of Different Oligomeric States.", **Nanoscale** (2018).
- Ang, JooChuan, Dan Ma, et al. "Sub-20 nm Stable Micelles Based on a Mixture of Coiled-coils: A Platform for Controlled Ligand Presentation." **Biomacromolecules** 18.11 (2017): 3572-3580.
- Dan Ma, et al. "Design of PEG-Peptides Conjugates Based Micelles as Nanocarrier", abstract no. 395. 2017 Society of Engineering Science Annual Technical Meeting, July 25-28, 2017, Boston, MA.
- DeBenedictis, E. P., D. Ma, and S. Keten. "Structural predictions for curli amyloid fibril subunits CsgA and CsgB." **RSC Advances** 7.76 (2017): 48102-48112.
- Dan Ma, et al. "Design of 3-Helix Micelles with Tailorable Sizes and Shapes", abstract no. 556c. 2016 AIChE Annual Meeting (ISBN: 978-0-8169-1097-7), San Francisco, CA.
- Ma, Dan, et al. "Design of polymer conjugated 3-helix micelles as nanocarriers with tunable shapes." **Nanoscale** 8.46 (2016): 19334-19342.
- Ang, JooChuan, Dan Ma, et al. "Internal structure of 15 nm 3-helix micelle revealed by small-angle neutron scattering and coarse-grained MD simulation." **Biomacromolecules** 17.10 (2016): 3262-3267.
- E. Hamed, D. Ma, S. Keten, "Effect of polymer conjugation on stability and self-assembly of coiled coils", 2015, **Bionanoscience**, 5(3), pp.140-149.
- E. Hamed, D. Ma, S. Keten, "Multiple PEG chains attached onto the surface of a helix bundle: conformations and implications", **ACS Biomaterials Science and Engineering** 2015, 1, pp. 79–84.
- Hamed, E., Ma, D., & Keten, S. (2014). Effect of PEG conjugation on entropy driven self-assembly of coiled coils. Proceedings of the Society of Engineering Science 51st Annual Technical Meeting.